

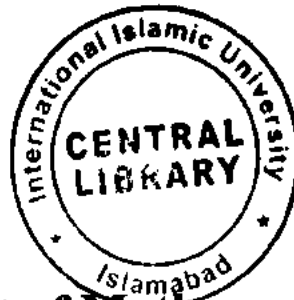
Study of convection flows in nanofluids



By

Mohsan Hassan

13-FBAS/PHDMA/S-12



Department of Mathematics and Statistics
Faculty of Basic and Applied Sciences
International Islamic University, Islamabad
Pakistan

2016

Accession No TH-16258
K
M. M.

PHD
S 10.2462
MOS

Study of convection flows in nanofluids



By

Mohsan Hassan

Supervised by

Dr. Rahmat Ellahi

&

Co Supervisor

Dr. Ahmad Zeeshan

**Department of Mathematics and Statistics
Faculty of Basic and Applied Sciences
International Islamic University, Islamabad
Pakistan**

2016

Study of convection flows in nanofluids

By

Mohsan Hassan

A Thesis

Submitted in the Partial Fulfillment of the

Requirements for the Degree of

DOCTOR OF PHILOSOPHY

IN

MATHEMATICS

Supervised by

Dr. Rahmat Ellahi

&

Co Supervisor

Dr. Ahmad Zeeshan

Department of Mathematics and Statistics

Faculty of Basic and Applied Sciences

International Islamic University, Islamabad

Pakistan

2016

Certificate

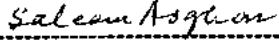
Study of convection flows in nanofluids

By

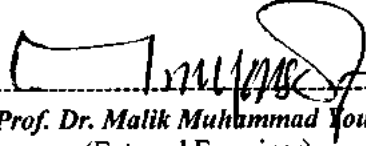
Mohsan Hassan

A THESIS SUBMITTED IN PARTIAL FULFILLMENT OF THE REQUIREMENT
FOR THE DEGREE OF DOCTOR OF PHILOSOPHY IN MATHEMATICS

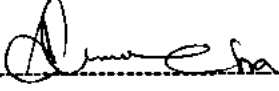
We accept this as conforming to the required standard

1. 

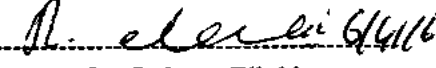
Prof. Dr. Saleem Asghar
(External Examiner)

2. 

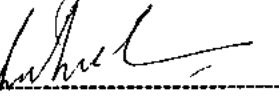
Prof. Dr. Malik Muhammad Yousaf
(External Examiner)

3. 

Dr. Ambreen Afsar Khan
(Internal Examiner)

4. 

Dr. Rahmat Ellahi
(Supervisor)

5. 

Dr. Ahmed Zeeshan
(Co-Supervisor)

6. 

Prof. Dr. M. Arshad Zia
(Chairman)

Department of Mathematics and Statistics
Faculty of Basic and Applied Sciences
International Islamic University, Islamabad
Pakistan
2016

Declaration

hereby declare and affirm that this research work neither as whole nor as a part has been copied out from any source. It is further declare that I have developed this research work entirely on the basis of my personal efforts. If any part of this thesis is proven to be copied out or found to be a reproduction of some other, I shall stand by the consequences.

Moreover, no portion of the work presented in this thesis has been submitted in support of an application for other degree or qualification in this other university or institute of learning.

Signature:-----

Mohsan Hassan

PhDScholar (Mathematics)

Dedication

This thesis is dedicated to my parents and wife

Acknowledgements

Firstly, I am thankful to Almighty Allah, who created us, taught us everything we did not know, provided us with balance, health, knowledge and intelligence to explore his world. I offer salutation upon the Holy Prophet Hazrat Muhammad (PBUH), who has lightened the life of all mankind with his guidance. He is a source of knowledge and blessings for the entire creations. His teachings make us to ponder and to explore this world with direction of Islam.

Secondly, I express my profound gratitude to my respected supervisor Dr. Rahmat Ellahi and co-supervisor Dr. Ahmed Zeeshan, who helped me throughout my PhD study with their cooperation guidance and guided me to complete my thesis within due course of time. This thesis would not have been successfully completed without their valuable intellectual tutelage, words of encouragement, push for tenacity and opportunity to gain from their wealth of knowledge. I am also pay my regards to all my teachers who always directed me to right dimensions and made it possible for me to achieve high goals in my life.

I extend my gratitude to my family for encouragement and support, even in the gloomiest of times. I am also thankful to my friends specially Mohsin Raza, Khurram Javid and others who always helped me during my studies in all respects.

I am also very thankful to Higher Education Commission, Pakistan for providing me scholarship under Indigenous 5000 PhD Fellowship Program without which it would not be possible for me to complete my higher studies.

Mohsan Hassan

Preface

In this thesis study of convective flow in nanofluids is investigated with different nanoparticles in diverse geometries. Mathematical modeling is based upon continuity, momentum and energy equations. The physical problems are first modeled and then the basic governing equations are reduced to a set of non-dimensional form by using appropriate transformations. The work undertaken is a blend of numerical and analytical studies. The nonlinear partial differential equations are analytically solved by means of homotopy analysis method (HAM), Bvph2 Package and optimal homotopy method (OHAM) whereas the numerical results obtained through Control Volume Based Finite Element Method (CVFEM) by using Mathematica and FORTRAN softwares. Convergence of presenting series solutions has been conferred by means of the average residual error and error norm in their respective admissible range. Different nanofluids contain different nanomaterials such as carbon tubes, metal oxides and metal base nanoparticles of various shapes, different sizes of particles with nanolayer and aggregation parameters are taken into account. The physical interpretations of sundry parameters such as Eckert number, Prandtl number, Rayleigh number, power law index, porosity parameter, radiation parameter, nanoparticle volume fraction and magnetic parameter are illustrated by graphs and tables. The effects of nanoparticle concentrations on shear stress, heat flux and thermal resistance along with several aspects are analyzed. In addition, correlation of Nusselt number and Skin friction corresponding to active parameters are also presented. It is observed that the nanofluids appear to have the potential to significantly increase convection heat transfer rates in a variety of areas and have found to possess enhanced thermophysical properties too. It is found that convection heat transfer increases by increasing the concentrations of all types of nanomaterials. It is also seen that heat transfer enhances more by carbon tubes nanoparticle as compared to the spherical nanoparticles whereas the aggregation is the most heat enhancing element. Comparison with the existing studies is made as a limiting situation for some considered problems.

This thesis comprises ten chapters. Chapter one provides introduction, some basic definitions, governing equations and methodology relevant to the material presented

in the subsequent chapters. Detail description of each chapter is given in motivation; the first subsection of introduction.

Contents

1	Introduction.....	1
1.1	Motivation.....	1
1.2	Analytical models for physical properties of nanofluid.....	12
1.2.1	Density of nanofluid.....	12
1.2.2	Heat capacity of nanofluid.....	12
1.2.3	Thermal expansion coefficient of nanofluid.....	13
1.2.4	Viscosity of nanofluid.....	13
1.2.5	Thermal conductivity of nanofluid.....	15
1.3	Governing equations	19
1.3.1	Conservation of mass.....	19
1.3.2	Conservation of momentum	20
1.3.3	Conservation of energy.....	21
1.4	Significance of governing parameters on convection flow.....	22
1.5	Methods of solutions.....	23
1.5.1	Homotopy analysis method.....	24
1.5.2	Bpvh2 package.....	25
1.5.3	Optimal homotopy analysis method.....	26
2	Magnetohydrodynamic flow of water/ethylene glycol based nanofluids with natural convection through porous medium.....	29
2.1	Mathematical formulation of the problem.....	29
2.2	Solution of the problem.....	32
2.3	Results and discussion.....	35
2.4	Conclusions.....	42
3	Shape effects of nanosize particles in $Cu - H_2O$ nanofluid on entropy generation.....	43
3.1	Mathematical formulation of the problem.....	43
3.2	Solution of the problem.....	46
3.3	Results and discussion.....	48
3.4	Conclusions.....	56
4	Study of natural convection MHD nanofluid by means of single and multi-walled carbon nanotubes suspended in a salt-water solution	57

4.1	Mathematical formulation of the problem.....	57
4.2	Solution of the problem.....	58
4.3	Results and discussion.....	60
4.4	Conclusions.....	68
5	On the modeling of natural convection flow of non-Newtonian nanofluid past a vertical cone.....	69
5.1	Mathematical formulation of the problem.....	69
5.2	Solution of the problem.....	72
5.3	Results and discussion.....	73
5.4	Conclusions.....	78
6	CVFEM for MHD natural convection flow of Cu-water nanofluid in elliptics cylinder.....	79
6.1	Mathematical formulation of the problem.....	79
6.2	Solution of the problem.....	81
6.3	Results and discussion.....	81
6.4	Conclusions.....	92
7	A study of heat transfer in power law nanofluid.....	93
7.1	Mathematical formulation of the problem.....	93
7.2	Solution of the problem.....	96
7.3	Results and discussion.....	99
7.4	Conclusions.....	104
8	Shape effects of spherical and non-spherical nanoparticles in mixed convection flow over a vertical stretching permeable sheet.....	105
8.1	Mathematical formulation of the problem.....	105
8.2	Solution of the problem.....	108
8.3	Results and discussion.....	108
8.4	Conclusions.....	116
9	A study of Fe_3O_4 nanoparticles aggregation in engine oil base nanofluid over vertical stretching permeable sheet in mixed convection....	117
9.1	Mathematical formulation of the problem.....	117
9.2	Solution of the problem.....	120
9.3	Results and discussion.....	120
9.4	Conclusions.....	125

10 Particle shape effects on marangoni convection boundary layer flow of a nanofluid.....	127
10.1 Mathematical formulation of the problem.....	127
10.2 Solution of the problem.....	130
10.3 Results and discussion.....	131
10.4 Conclusions.....	137
Reference.....	138
Nomenclature.....	152

Chapter 1

Introduction

1.1 Motivation

Heat transfer is the exchange of thermal energy between physical systems, depending on the temperature and pressure, by dissipating heat. One of the fundamental modes of heat transfer is convection. Convection is the concerted, collective movement of groups or aggregates of molecules within fluids e.g., liquids, gases. It can be qualified in terms of being natural (free) and forced, although other mechanisms also exist. Natural convection or free convection occurs due to temperature differences which affect the density and thus relative buoyancy of the fluid. Forced convection is typically used to increase the rate of heat exchange. Many types of mixing also utilize forced convection to distribute one substance within another. By-product to other processes, such as the action of a propeller in a fluid or aerodynamic heating, heating and cooling of parts of the body by blood circulation, are other familiar examples of forced convection. It is also well-established fact that when the forced and free convection differences are of harmonious order phenomena then mixed convection occurs. It has energetic appearance in atmospheric boundary layer flows, heat exchangers, solar collectors, nuclear reactors and in electronic equipment's. Mixed convective flows with heat transfer are extensively used in chemical industries like design of canisters for nuclear waste disposal and nuclear reactor cooling system etc. These physical processes occur in the situation where the impact of buoyancy forces becomes much more dominant. Consequentially, convective flow has been widely studied due to its wide applications such as post accidental heat removal in nuclear reactors, solar collectors, drying processes, heat exchangers, geothermal oil recovery and building construction, etc. [1-4].

Modern advances in nanotechnology have led to the development of a new innovative class of heat transfer called nanofluids created by dispersing nanoparticles (10-50nm) in traditional heat transfer fluids. Nanofluids appear to have the potential to significantly increase heat transfer rates in a variety of areas such as industrial cooling applications, nuclear reactors, transportation industry (an automobiles, trucks, and

airplanes), micro-electromechanical systems, electronics and instrumentation, and biomedical applications (nano-drug delivery, cancer therapeutics, cryopreservation) etc. Nanofluid has been found to possess enhanced thermophysical properties such as thermal conductivity, thermal diffusivity, viscosity and convective heat transfer coefficients compared to those of base fluids like oil or water. The materials which are commonly used as nanoparticles include chemically stable metals (e.g., gold, copper), metal oxides (e.g., alumina, silica, zirconia, titania), oxide ceramics (e.g., Al_2O_3 , CuO), metal carbides (e.g., SiC), metal nitrides (e.g., AlN , SiN), carbon in various forms (e.g., diamond, graphite, carbon nanotubes) and functionalized nanoparticles. Some relevant studies on the topic can be seen from the list of references [5-8].

Nowadays, convective heat transfer in nanofluids is a topic of major contemporary interest [9]. Das et al. [10] did the experiment for nanofluid, they found a unique and encouraging feature about heat transfer improvement. Some numerical and experimental studies on heat transfer enhancement in nanofluids are listed in [11-13]. In these studies it is concluded that the difference in heat transfer, using different nanofluids, increases with increasing the value of volume fraction of nanoparticles. Theoretical studies on laminar free convection flow over a cone have received wide attention especially in case of uniform and non-uniform surface heat and mass flux. A similarity solution for the laminar free convection from a right circular cone is presented by Lin [14]. Pop et al. [15] focused the theoretical study on the effects of suction or injection on steady free convection from a vertical cone with uniform surface and heat flux condition. A non-similarity solution is studied by Hossain [16] for the free convection from a vertical permeable cone with non-uniform surface heat flux. Saturated porous media combined heat and mass transfer effects over a full cone are reported by Yih [17].

In recent years, there have been several studies in which magnetic field plays an important roles and have attracted the interest of many researchers due to its vital applications in abundant fields such as petroleum industries, crystal growth, liquid-metal cooling of nuclear reactors, magnetic behavior of plasmas in fusion reactors, electromagnetic casting, boundary layer control in aerodynamics, ship propulsion, jet printers, etc. A magnetic field is strongly related to the comprehension of physical effects which take place in magnetohydrodynamic (MHD). The magnetics field is extensively concerned with the flow, heat and mass transfer characteristics in various

physical situations.

The convective heat transfer mechanism of nanofluids through porous medium is gained considerable attention of many researchers in order to establish a better understanding of the associated transport processes. An important characteristic for the combination of porous medium and fluid is tortuosity which represents the hindrance to flow diffusion imposed by local viscosity or local boundaries [18-20].

In view of aforementioned investigations, it is found that no such analysis is yet available in the literature which can simultaneously describe the effects of magnetohydrodynamic, heat generation and porosity on nanofluids along an inverted cone with variable wall temperature. Motivated by these facts, the present effort is devoted to analyze the fully developed flow of water and ethylene glycol base nanofluids containing spherical shape copper nanoparticles in order to fill this gap. The Skin-friction and heat transfer rate for both nanofluids are also presented. The water and ethylene glycol based nanofluids containing spherical shape copper nanoparticles are taken in account. To derive the solutions of nonlinear coupled equations, we have used one of the most efficient methods, homotopy analysis method, which is particularly suitable for nonlinear problems. Homotopy analysis method provides us a simple way to ensure the convergence of series solutions of a nonlinear problem as well and does not require any small parameter. **The results of this chapter (two) are published in the journal of European Physical Journal Plus, 129 (2014) 261- 271.**

Moreover, the simplest model based on the macroscopic effective medium theory was first developed by Maxwell for a dilute suspension of non-interacting spherical particles. This model shows that the effective thermal conductivity of nanofluids depends on the thermal conductivities of the spherical particle, thermal conductivity of base fluid and the volume fraction of the solid particles. Further developments on nonspherical particle shapes are presented by Hamilton and Crosser [21]. Hamilton and Crosser showed that when the particle-to-liquid conductivity ratio of a suspension is above about 100, the particle shape has a substantial effect on the effective thermal conductivity of the suspension. Although the renovated Maxwell model is limited to suspensions with spherical particles, an important feature of the Hamilton-- Crosser model is that it can predict the effective thermal conductivity of suspensions with nonspherical particles. The base fluid, or dispersing medium, can be aqueous or non-aqueous in nature. Typical nanoparticles are metals, oxides, carbides, nitrides, or

carbon nanotubes. Their shapes may be spheres, disks, or rods etc. [22]. The thermal conductivities of different particles in liquid suspensions with spherical and nonspherical particles are of great interest in various engineering applications because of their high effective thermal conductivities over base liquids at very low particle volume concentrations of nanoparticles [23, 24]. In addition to the differences in sample quality, another major cause of the large discrepancies in the thermal conductivity is the fact that the thermal conductivity of nanofluids depends on a great number of parameters, some of which are coupled. Experimental studies have shown that the thermal conductivity of nanofluids is determined by the physical parameters related to different nanoparticles, concentration, size [25-27], shapes [28, 29], agglomeration (fractal-like shapes) [30-33], surface charge [34] base fluids and others.

Furthermore, the studies on natural convection using nanofluids are very limited and they are related with different cones. Wide ranges of investigations have been conducted by researchers in MHD natural convection. The MHD effects on natural convection heat transfer in an enclosure filled with nanofluid are studied by Sheikholeslami et al. [35]. Their results indicated that Nusselt number is an increasing function of buoyancy ratio number but it is a decreasing function of Lewis number and Hartmann number. Sheikholeslami and Ganji [36] investigated two phase modeling of nanofluid in a rotating system with permeable sheet. They found that Nusselt number has direct relationship with Reynolds number and injection parameter while it has reverse relationship with rotation parameter, Schmidt number, Thermophoretic parameter and Brownian parameter. Lattice Boltzmann Method was used to investigate magnetohydrodynamic flow utilizing Cu-water nanofluid in a concentric annulus by Sheikholeslami et al. [37]. Their results proved that enhancement ratio increases with decrease of Rayleigh number and it increases with augment of Hartmann number. Some other numerical and analytical studies on natural convection, heat transfer, porosity and magnetohydrodynamic can be found in the references [38-42].

In short, the studies of combined effects of magnetohydrodynamic, radiation and porous media along a vertical cone with nanofluid of different shapes of nanoparticles are yet not reported in the literature. The present work reports the results of a particle shape factor on natural convection boundary-layer flow of a nanofluid over an inverted vertical cone embedded in a porous medium in the presence of

magneto hydrodynamic, radiation and power law index effects. Effects of Bejan number and entropy generation analysis are also shown. **Results of this effort (chapter three) are published in International Journal of Heat and Mass Transfer, 81 (2015) 449–456.**

In the nanomaterials, the carbon nanotubes (CNTs) have inherently special physical and chemical properties such as the unique optical, thermal and magnetic performance, etc. Hence, the CNTs can be regarded as one of the most promising materials in all nanomaterials [43]. The most commonly used CNTs are single-walled carbon nanotubes (SWCNTs) and multi-wall carbon nanotubes (MWCNTs). The SWCNTs have only one single layer of grapheme cylinders while the MWNTs have many layers [44]. The CNTs have excellent thermal conductivity and mechanical properties. By mixing them in the solid [45-48] or fluid [49, 50], the mixture can effectively enhance the thermal performance and mechanical properties of the base materials. Therefore, the CNTs employed in the field are evaluated with great potential for the heat transfer applications. The first experimental observation in the increase of thermal conductivity using cylindrical structures, namely multi-walled nanotubes (MWCNT), was reported by Choi and co-workers [51]. They reported that a thermal conductivity increase of 160% for the case of MWCNTs dispersed in oil at a nanotube loading of 1 vol%. Garg et al. [52], prepared multi-walled carbon nanotube (MWCNT) based aqueous nanofluids for heat transfer study. The maximum enhancement in thermal conductivity and heat transfer was found 20% and 32% respectively. Bakhshan [53] has investigated the thermal performance of nanofluid by using multi-wall carbon nanotube (MWCNT). In this investigation, three different types of water based nanofluids namely (Al₂O₃ plus water), (Diamond+Water) and (Multi-Wall Carbon Nano tube (MWCNT) +Water) were considered. The results show that the MWCNT based nanofluid has lower thermal resistance but higher heat transfer coefficient as compared to other nanofluids. In addition, experimental and numerical studies on very high thermal conductivity for CNTs can be found in [54] and several references therein. Hence, it is natural to expect that the suspensions consisting of CNTs would result in higher thermal conductivity increase compared to other nanoparticles.

Besides, typically, fluid flow is governed by the partial differential equation system of mass, momentum and energy conservation, but in case of natural convection the situation is quite complex since the velocity and the temperature equations are

coupled due to the buoyancy force. Due to this inherent nonlinearity of the resulting equations, analytical solutions are very rare even where available immense simplification assumptions have explicitly been imposed. To deal with this hurdle several analytical techniques have been developed to fulfill this gap, the "homotopy analysis method" is one of them. In this study, the systems of coupled nonlinear equations are solved analytically by means of a Mathematica package BVP4c [55] based on the homotopy analysis method. Results for velocity, temperature, Skin-friction coefficient and Nusselt number in this investigation are obtained at 30th order iterations.

To the best of authors' knowledge no study has yet been communicated for single and multi-wall carbon nanotube in natural convection flow of a salt-water solution based nanofluid with joule heating. The objective of the proposed study is therefore to analyze the development of natural convection boundary layer flow along a vertical cone for interfacial layers around carbon nanotube in the presence of different quantity of salt in water under the magnetohydrodynamic. This analysis (chapter four) is published in **IEEE Transaction on Nanotechnology, 14 (2015), 726-734.**

As there are two groups of techniques to intensify heat transfer. The first group of techniques, it is needed to external energy input via mechanical vibration, rotation, mixing and adding of external magnetic or electrostatic field, which have been used successfully to improve heat and mass transfer. However external energy input is expensive and difficult under compacted situations. In second group of techniques, the heat transfer magnification can be attained by modifying fluids property, changing of surface shape, increase surface area by and turbulence etc. The existing literature reveals that a very small effort has been yet devoted on heat transfer of nanofluids by different geometries. Lately, Bajestan et al. [56] have studied the thermal properties of nanofluids under forced convection heat transfer in straight and curved geometry. They found that the curvature effects and nanoparticle enhance heat transfer features simultaneously. Bajestan and Niazmand [57] have investigated the heat transfer of water base with the present of carbon nanotubes (CNT) in a vertical curved pipe. They witnessed that the secondary flows are induced by curvature effects and as a result the heat transfer rate is enhanced, and further enhanced strangely by using nanofluids.

With all abovementioned studies, one can clearly observe that no analysis for natural convection of a viscoelastic nanofluid along a vertical cone for different material of

nanoparticles is reported in the available literature yet. The present work puts forward to fill this gap. The PDMS is used as a base fluid. This study (chapter five) is submitted for possible publication in **Advances in Mechanical Engineering, (2015)**. Recent past, natural convective heat transfer in horizontal annuli has concerned many considerations because of its wide uses such as in nuclear reactor design, cooling of electronic equipment, aircraft cabin insulation and thermal storage system. A large and diverse number of literatures on both experimental and numerical investigations were published in the past few decades. Among them, the majority was involved in horizontal circular annuli. Ghaddar [58] reported the numerical results of natural convection from a uniformly-heated horizontal cylinder placed in a large air-filled rectangular enclosure. He observed that flow and thermal behavior depended on heat fluxes imposed on the inner cylinder within the isothermal enclosure. Kuehn and Goldstein [59] systematically studied the concentric cases in a horizontal annulus between two circular cylinders. Haldar [60] reported numerical study of combined convection through a horizontal concentric annulus using a combination of vorticity-stream function and primitive variables formulations. It was found that with increasing axial distance, the entry effect diminishes, while the buoyancy becomes stronger.

In most of the available studies on natural convection in enclosures, the base fluid is a common fluid for which the thermal conductivity is usually low. The resulting performances of such thermal systems are relatively poor. A recent way of improving the performance of these systems is to suspend metallic nanoparticles in the base fluid. Abu-Nada et al. [61] investigated natural convection heat transfer enhancement in horizontal concentric annuli field by nanofluid. They found that for low Rayleigh numbers, nanoparticles with higher thermal conductivity cause more enhancement in heat transfer. Saleh et al. [62] studied the effect of inclination angles of the sloping wall on the flow and temperature fields in a trapezoidal enclosure filled with nanofluids. It was found that acute sloping wall and Cu nanoparticles with high concentration are effective to enhance the rate of heat transfer. MHD effect on natural convection heat transfer in an inclined L-shape enclosure filled with nanofluid was studied by several authors investigated the effect of adding nanoparticle in base fluid on heat transfer enhancement [63-67].

Control Volume based Finite Element Method (CVFEM) is a scheme that uses the advantages of both finite volume and finite element methods for simulation of multi-

physics problems in complex geometries [68-71]. Sheikholeslami et al. [72] discussed the phenomena of free convection amid a circular enclosure and a sinusoidal cylinder. They determined that isotherms, streamlines, size, the number and formation of the cells inside the enclosure intensely influenced by on the values of amplitude, Rayleigh number and the number of undulations of the enclosure. In their further studies [73, 74], they used technique CVFEM in order to observed the impact of magnetohydrodynamic on Cu–water nanofluid. Their outcomes pointed that Hartmann number use as control parameters at different Rayleigh number.

The main goal of the present work is to conduct a numerical investigation of natural convection heat transfer between a circular enclosure and an elliptic cylinder filled with nanofluid using the Control Volume based Finite Element method. This study (chapter six) is published in **Journal of Magnetism and Magnetic Materials**, **349 (2014) 188–200**.

As a result of thermal conductivity the base fluid is dramatically enhanced in the presence of nanoparticles that is why the thermal conductivity of nanofluids has attracted the most widely attention of scientists due to its essential heat transfer properties. Sajadi et al. [75] reported the experimental study to improve the thermal performance of Newtonian fluid water by ZnO particles. The results indicated that heat transfer coefficient increases by 11% and 18% with increasing the volume fractions of nanoparticles to 1% and 2% respectively. It is overall thermal performance of nanofluid which is higher than that of pure water up to 16% for 2% volume concentration of nanoparticles. Another experimentally study examined the convective heat transfer in a helically coiled heat exchanger in laminar to turbulent regime under isothermal steady state and non-isothermal unsteady state conditions for Newtonian as well as non-Newtonian fluids. Newtonian and non-Newtonian nanofluids through a uniformly heated circular tube under turbulent flow conditions are considered [76]. The results in this work showed that overall heat transfer coefficient is higher for smaller helix diameter as compared to larger helix diameter due to significant effect of centrifugal force on secondary flow in coil. It is also observed from results that heat transfer coefficients for pure water are higher than glycerol–water mixture and non-Newtonian fluids for the same conditions. They conclude that enhanced migration of suspended nanoparticles via the mechanisms of thermophoresis increases energy exchange rates in the fluid. Nevertheless, addition of nanoparticle improves the thermal properties even in Newtonian and Non-Newtonian

base fluid.

In this chapter, the shear thinning polymer solution fluid under the influence of nanoparticle on it over stretching sheet is investigated. The study of mass flow and heat transfer over a stretching sheet may find its applications in polymer technology related to the stretching of plastic sheets. Also, many metallurgical processes involve the cooling of continuous strips or filaments by drawing them through a quiescent fluid and while drawing these strips are sometimes stretched. For shear thinning fluid, power law model and mathematical model reduced into nonlinearity. Due to intrinsic nonlinearity of the governing equations, analytical solutions are very rare. To deal with this difficulty numerous analytical and semi analytical methods have been established. The "optical homotopy analysis method" is one of most effective technique among them to handle this obstacle. This investigation (chapter seven) is accepted in **Thermal Science, (2015)**.

As the theory of spherical and non-spherical particles in nanofluid are of great interest in various applications because of their much higher effective thermal conductivities over those of base liquids at very low particle volume concentrations. Shalkevich and co-workers [77] have carefully studied the effect of particle size, concentration, method of stabilization and clustering on thermal transport in gold nanofluid. A maximum enhancement of 1.4 % is reported for volume 0.11% suspension of 40 nm diameter particles in water suggesting no apparent anomaly. Typical thermal conductivity of spherical particles enhancements are in the range 15% to 40% over the base fluid whereas the heat transfer coefficient enhancements have been found up to 40% [78]. In the literature, several authors investigate the thermal properties of cylindrical structures nanoparticle, namely single or multiwall nanotubes suspensions in a variety of solvents [79-82]. Owing to different aspect ratios, solvents and type of nanotubes (single or multiwall), there is considerable spread in the data. The reported values range from 10 % to over 150 % enhancement in the thermal conductivity for one volume 1 % concentration. Singh et al. [83] have studied the heat transfer behavior of aqueous suspension of silicon carbide having oblate shape and aspect ratio of around 1/4. They typically observed 30 % enhancement for volume 7 % concentration. Khandekar et al. [84] employed various spherical nanoparticle as well as Laponite JS (oblate shape, aspect ratio 1/25) based nanofluids in closed two phase thermosyphon and observed its heat transport behavior to be inferior to that of pure water in all cases.

The literature review bear witness that the two-dimensional heat transfer mixed convection flow over a vertical stretching permeable sheet with nanofluid of different shapes of nanoparticles are yet not reported in the literature. In order to fill this gap, the objective of this paper is to solve the said problem of by considering the spherical and non-spherical shapes with different sizes of nanoparticles. In order to investigate the heat transfer rate and Skin friction, the HFE-7100, HFE-7200 and HFE-7500 Engineered Fluids are used as based fluids since these are nonflammable fluids with very low global warming potential in heat transfer applications. In addition, the effects of variable wall temperature and suction/injection parameters on nanofluid are also taken into account.

The present work reports the results of on two-dimensional heat transfer mixed convection flow of a nanofluid over a vertical stretching permeable sheet by considering the spherical and non-spherical shapes with different sizes of nanoparticles. In order to investigate the heat transfer rate and skin friction, the HFE-7100, HFE-7200 and HFE-7500 Engineered Fluids are used as base fluids since these are nonflammable fluids with very low global warming potential in heat transfer applications. In addition, the effects of variable wall temperature and suction/injection parameters on nanofluid are also taken into account. . Effects of Nusselt number and Skin friction are also presented. These finding (chapter eight) are accepted in **Journal of Mechanics of Advanced Materials and Structures, (2015)**.

The mechanism behind the exceptionally enhanced thermal conductivity of nanofluids is a hotly debated topic. The debate behind the mechanism is largely fueled by limited experimental characterization of the nanofluid systems. However, a number of recently reported experimental studies strongly suggest that nanoparticle aggregation plays a significant role in the thermal transport in nanofluids [85-87]. A large thermal conductivity enhancement goes with sharp viscosity increases at low nanoparticle volume fractions [88], which is indicative of aggregation effects. The critical importance of particle surface charge in nanofluid thermal conductivity is already observed. The surface charge is one of the primary factors controlling nanoparticle aggregation. The linear aggregation of stabilized magnetite particles in a magnetic field is measured by [89] and enhancement of 64% is found. Thus, aggregation is an important factor for thermal applications of any nanofluid.

In this chapter, the mixed convection with variable wall temperature and magnetic influence in the presence of buoyancy force is studied. Another important area of

study is the interfacial layer which has fascinated the attention of many researchers. The response of interfacial layers to deformations in size and shape depends on their composition. The important properties of interfacial layers are dilatational and shear viscoelasticity. It contains the foaming and emulsification extensively used in the manufacture of cosmetics, pharmaceuticals and food, mining, oil industry, etc. In addition to the large interest on industrial applications, studying the interfacial layers is still very significant from a fundamental point of view, such as understanding the interaction between molecules, molecular aggregations and the change of molecular conformations [90].

The core determination of this present work is to isolate the effects of aggregation on nanofluid over a nonlinear stretching sheet in mixed convection with the corresponding interfacial layers. The variable wall temperature and magnetic field are also taken into account. The said model is not yet extensively investigated. In particular, when aggregate is embedded within a sphere and is composed of a few approximately linear chains, it will span the whole aggregate and side chains. We have also proposed some possible future work at the end of this paper. This investigation (chapter nine) is accepted in **Journal of Zhejiang University-SCIENCE A**, (2015).

The temperature and surfactant concentration gradients at the interface of two fluid layers give rise to surface tension variations that can induce interfacial flows from region of low surface tension to region of high surface tension. The surface-tension-driven convection is also known as Marangoni convection has central importance in industrial, biomedical and daily life applications, e.g., coating flow technology, microfluidics, surfactant replacement therapy for neonatal infants, film drainage in emulsions and foams and drying of semi-conductor wafers in microelectronics [91, 92]. It appears that Napolitano [93] was the first to recognize the Marangoni boundary-layers that can be formed along the interface of two immiscible fluids in surface driven flows. In recent times the study of nanofluid in Marangoni convection boundary layer has been given a considerable attention by the researchers. For instance Arifin et al. [94] have considered the problem of non-isobaric Marangoni boundary layer flow along the interface of immiscible nanofluid. Mat et al. [95] also investigated Marangoni convection in nanofluid with the addition of radiation effects. All problems mentioned are using model proposed by Tiwari and Das [96]. Sastry et al. [97] have studied the problem of heat transfer on the Marangoni convection

boundary layer flow in an electrically conducting nanofluid.

A literature review bear witness that the particle shape effects on Marangoni convection boundary layer flow of a nanofluid are yet not reported in the literature. In order to fill this gap, the focus of this is to study the particle shape effects on Marangoni convection boundary layer flow of a nanofluid. The copper nanoparticles as nanomaterial with spherical and non-spherical shapes of different sizes and aqueous solutions of ethylene glycol as base fluid as nanofluid is used. This study is accepted in **International Journal for Numerical Methods in Fluids**, (2015).

1.2 Analytical models for physical properties of nanofluids

1.2.1 Density of nanofluid

The density of nanofluid is based on the physical principle of the mixture rule. As such it can be represented as

$$\rho_{nf} = \left(\frac{M}{V} \right)_{nf} = \frac{M_f + M_s}{V_f + V_s} = \frac{\rho_f V_f + \rho_s V_s}{V_f + V_s}, \quad (1.1)$$

$$\rho_{nf} = \left(1 - \frac{V_s}{V_f + V_s} \right) \rho_f + \left(\frac{V_s}{V_f + V_s} \right) \rho_s, \quad (1.2)$$

$$\rho_{nf} = (1 - \phi) \rho_f + (\phi) \rho_s, \quad (1.3)$$

where M is mass and V is volume respectively. The f and s in subscripts respectively refer to the fluid and nanoparticle while ϕ is the volume fraction of the nanoparticles. To examine the validity of Eq. (1.3), Pak and Cho [98] and Ho et al. [99] conducted experimental studies to measure the density of Al_2O_3 -water nanofluids at room temperature as shows an excellent agreement between the experimental results and the predictions using Eq. (1.3).

1.2.2 Heat capacity of nanofluid

The specific heat of nanofluid can be determined by assuming thermal equilibrium between the nanoparticles and the base fluid phase as follows

$$(\rho C_p)_{nf} = \rho_{nf} \frac{(MC_p)_f \Delta T + (MC_p)_s \Delta T}{(M_f + M_s) \Delta T}, \quad (1.4)$$

$$(\rho C_p)_{nf} = \rho_{nf} \frac{(MC_p)_f \Delta T + (MC_p)_s \Delta T}{(M_f + M_s) \Delta T}, \quad (1.5)$$

$$(\rho C_p)_{nf} = \rho_{nf} \frac{(V \rho C_p)_f + (V \rho C_p)_s}{\frac{(M_f + M_s)}{(V_f + V_s)} \times (V_f + V_s)}, \quad (1.6)$$

$$(\rho C_p)_{nf} = (1 - \phi)(\rho C_p)_f + \phi(\rho C_p)_s, \quad (1.7)$$

where ρ_s is the density of the nanoparticle, ρ_f is the density of the base fluid, ρ_{nf} is the density of the nanofluid and the heat capacities of the nanoparticle $(C_p)_s$ and the base fluid $(C_p)_f$, respectively. The nanofluid based on the models given in Eq. (1.7) decreases with an increase in the volume fraction of nanoparticles. The experimental results were compared with the predictions obtained from the models compares very well with the experimental data of Zhou and Ni [100].

1.2.3 Thermal expansion coefficient of nanofluid

The thermal expansion coefficient of nanofluids can be estimated utilizing the volume fraction of the nanoparticles on a weight basis as follows [101]

$$(\rho\beta)_{nf} = (1 - \phi)(\rho\beta)_f + \phi(\rho\beta)_s, \quad (1.8)$$

where β_f and β_s are the thermal expansion coefficients of the base fluid and the nanoparticle, respectively.

1.2.4 Viscosity of nanofluid

The viscosity of nanofluids is of great significance as the application of nanofluids is always associated with their flow. A few studies have addressed the viscous properties of nanofluids [102-104]. In general, the viscosity of nanofluids is much higher than that of their base fluids. The viscosity is a strong function of temperature and the volumetric concentration. Furthermore, a particle-size effect seems to be important only for sufficiently high particle fractions. In 1956, Einstein [105] was determined the effective viscosity of a suspension of spherical solids as a function of volume fraction (volume concentration lower than 5%) using the phenomenological hydrodynamic equations. This equation was expressed by

$$\mu_{nf} = (1 - 2.5\phi) \mu_f, \quad (1.9)$$

where μ_{nf} is the viscosity of the nanofluid and μ_f is the viscosity of the base fluid. Later, Einstein's equation was extended by Brinkman [106] to suspensions with moderate particle volume fraction, typically less than 4% as defined as

$$\mu_{nf} = \frac{\mu_f}{(1 - \phi)^{2.5}}. \quad (1.10)$$

Considering the Brownian motion of nanoparticles and the interaction between a pair of particles, Batchelor [107] proposed the following equation.

$$\mu_{nf} = (1 - A_1\phi + A_2\phi^2 + \dots) \mu_f. \quad (1.11)$$

In Eq. (1.11), A_1 is the intrinsic viscosity and A_2 is the Huggins' coefficient. The values of A_1 and A_2 are 2.5 and 6.5, respectively, for spherical particles. For non-spherical shape Brenner and Condiff [108] have developed a viscosity model to consider the shape effects in dilute suspension as follow

$$\mu_{nf} = (1 - A_1\phi) \mu_f \quad (1.12)$$

with

$$A_1 = \frac{0.312r^*}{\ln 2r^* - 1.5} + 2 - \frac{0.5}{\ln 2r^* - 1.5} - \frac{1.872}{r^*}, \quad (1.13)$$

where r^* is the aspect ratio of nanoparticles at high shear rate viscosity.

The viscosity model nanofluid [109] with the effect of nanolayer is given by

$$\mu_{nf} = (1 + (2.5\phi_e) + (2.5\phi_e)^2 + (2.5\phi_e)^3 + \dots) \mu_f, \quad (1.14)$$

in which $\phi_e = \phi(1 + \beta^*)^3$ and $\beta^* = h_{layer} / R_p$ is ratio of the nanolayer thickness to the original particle radius.

When nanoparticles suspended in liquid would aggregate with each other to form chain structure and viscosity model [110] is given as

$$\mu_{nf} = \mu_f \left(1 - \frac{\phi_a}{\phi_{max}} \right)^{-2.5\phi_{max}}, \quad (1.15)$$

where ϕ_a is volume fraction of the aggregates and ϕ_{max} is maximum volume fraction.

1.2.5 Thermal conductivity of nanofluid

The thermal conductivities of different particles in liquid suspensions with spherical and non-spherical particles are of great interest in various engineering applications because of their high effective thermal conductivities over base liquids at very low particle volume concentrations of nanoparticles [111-113]. The simplest model based on the macroscopic effective medium theory was first developed by Maxwell for a dilute suspension of non-interacting spherical particles [114] as follow

$$\frac{k_{nf}}{k_f} = \frac{k_s + 2k_f + 2(k_s - k_f)\phi}{k_s + 2k_f - (k_s - k_f)\phi} \quad (1.16)$$

This model shows that the effective thermal conductivity of nanofluids depends on the thermal conductivities of the spherical particle, thermal conductivity of base fluid and the volume fraction of the solid particles. Further developments on non-spherical particle shapes with introducing a shape factor can be expressed as

$$\frac{k_{nf}}{k_f} = \frac{k_s + (n^* - 1)k_f - (n^* - 1)\phi(k_f - k_s)}{k_s + (n^* - 1)k_f + \phi(k_f - k_s)}, \quad (1.17)$$

in which k_s and k_f are the conductivities of the particle material and the base fluid.

In this Hamilton-Crosser model, $n^* = 3/\Psi$ is the empirical shape factor (Ψ is the sphericity defined as a ratio between the surface area of the sphere and the surface area of the real particle with equal volumes). When one choose shape factor $n^* = 3$, then the Hamilton-Crosser model reduces to the Maxwell model for spherical particle mixtures. The thermal conductivity model for spherical and non-spherical nanoparticles is introduced by Yu [115] follow as

$$k_{nf} = \left(1 + \frac{n^* \phi_c A^*}{1 - \phi_c A^*} \right) k_f, \quad (1.18)$$

where

$$A^* = \frac{1}{3} \sum_{j=a,b,c} \frac{k_{pj} - k_f}{k_{pj} + (n^* - 1)k_f}, \quad (1.19)$$

k_p is the thermal conductivity along the axes of particle which is defined by

$$k_p = \left[1 + \frac{k_s - k_{layer}}{k_s (r_p d(j,0) - d(j,t)) - k_{layer} (r_p d(j,0) - d(j,t) - r_p)} \right] k_s \quad (1.20)$$

In the above Eq. (1.20), $j(=a, b \text{ and } c)$ is along the semi-axis directions of the particle, k_p and k_{layer} are the thermal conductivities of the solid particle and its surrounding layer respectively. The volume ratio r_p and depolarization factor $d(j, v)$ are defined by

$$r_p = \frac{\sqrt{(a^2 + t_1)(b^2 + t_1)(c^2 + t_1)}}{abc} \quad (1.21)$$

and

$$d(j, v_p) = \frac{\sqrt{(a^2 + v_p)(b^2 + v_p)(c^2 + v_p)}}{2} \quad (1.22)$$

$$\times \int_0^\infty \frac{dw_p}{(j^2 + v_p + w_p) \sqrt{(a^2 + v_p + w_p)(b^2 + v_p + w_p)(c^2 + v_p + w_p)}}$$

with $v_p = 0$ for outside of the solid ellipsoid and $v_p = t_1$ for outside surface of its surrounding layer. For a needle-shape particle with $a \gg b = c$, $d(a, v_p)$, $d(b, v_p)$ and $d(c, v_p)$ tend to 0, 1/2 and 1/2, respectively. For a disk-shape particle with $a = b \gg c$, $d(a, v_p)$, $d(b, v_p)$ and $d(c, v_p)$ tend to 0, 0 and 1, respectively. For a sphere with $a = b = c$, the three factors is 1/3.

The ordered layering of liquid molecules at the solid particle surface forms solid-like nanolayer. This layer acts as a thermal bridge between the solid nanoparticles and the base liquid and plays an important role in the enhanced thermal conductivity of nanofluids [116, 117]. The effective thermal conductivity increases with increase in nanolayer thickness. Especially in small particle size range, the effects of particle size and nanolayer thickness become much more obvious, which implies that manipulating nanolayer structure might be an effective method to produce highly thermally conductive nanofluids [118]. In order to take the liquid layer effects, assume that the solid-like layer thickness is h_{layer} around the spherical particles of radius is R_p and the thermal conductivity k_{layer} of this ordered layer is greater than the bulk liquid.

Moreover, combined with the nanolayer around each particle could be considering equivalent particle; consequently the particle do not overlap of those particles due to few particles volume fraction.

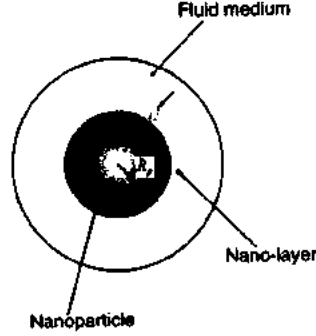


Fig. 1.1. Schematic of nano-layer.

The thermal conductive model [119] of nanofluid for nano-layer effect is given by

$$k_{nf} = \frac{k_{pe} + 2k_f + 2(k_{pe} - k_f)(1 + \beta^*)^3 \phi}{k_{pe} + 2k_f - (k_{pe} - k_f)(1 + \beta^*)^3 \phi} k_f. \quad (1.23)$$

The thermal conductive k_{pe} with layer around the particles is defined by

$$k_{pe} = \frac{[2(1 - \gamma) + (1 + \beta^*)^3 (1 + 2\gamma^*)] \gamma^*}{-(1 - \gamma^*) + (1 + \beta^*)^3 (1 + 2\gamma^*)} k_s, \quad (1.24)$$

here $\gamma^* = k_{layer} / k_s$ is the ratio of nanolayer and particle thermal conductivities.

Nanoparticles suspended in liquid would aggregate with each other to form chain structure which has been confirmed experimentally [120]. The linear chains which span the whole aggregate are called the backbone and other particles, which do not span the whole aggregate, are called dead ends [121]. The backbone plays a significant role in the rheology of colloids because it is the only structure that can transfer elastic forces between aggregate. Due to its connectivity, the backbone is also expected to play a crucial role in thermal conductivity. Fig. 1.2 describes the schematics of the independent single aggregate which includes the backbone and dead-end particles. To further understand the effect of aggregation on the fluid properties the thermal conductivity are modeled using fractal theory.

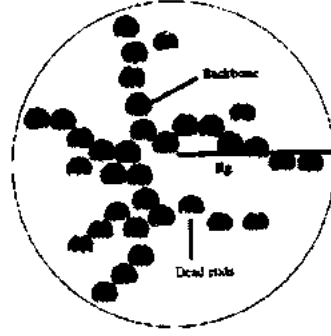


Fig. 1.2. Aggregate of nanoparticles, including the backbone and dead-end particles.

Therefore, the thermal conductivities of aggregates are estimated by separating them into two components, the percolation contributing backbone, and non-percolation contributing dead-end particles. Considering the interfacial thermal resistance (Kapitza resistance), the effective thermal conductivity of dead-end particles based suspension (including the basefluid and dead-end particles) is given by using Bruggeman model [122].

$$(1 - \phi_{nc})(k_f - k_{nc}) / (k_f + 2k_{nc}) + \phi_{nc}(k_s - k_{nc}) / (k_s + 2k_{nc}) = 0. \quad (1.25)$$

The effective thermal conductivity of aggregate, k_a is determined using composite theory for misoriented ellipsoidal particles for the backbone, in a matrix of the non-percolation contributing portion, the following equations are used

$$k_a = k_{nc} \frac{3 + \phi_c [2\beta_{11}(1 - L_{11}) + \beta_{33}(1 - L_{33})]}{3 - \phi_c [2\beta_{11}L_{11} + \beta_{33}L_{33}]}, \quad (1.26)$$

where

$$\begin{aligned} L_{11} &= 0.5p^{*2} / (p^{*2} - 1) - 0.5p \cosh^{-1} p^* / (p^{*2} - 1)^{1/2}, \\ L_{33} &= 1 - 2L_{11} \text{ and} \\ \beta_u &= (k_u^c - k_{nc}) / [k_{nc} - L_u(k_u^c - k_{nc})]. \end{aligned} \quad (1.27)$$

Interfacial resistance is accounted for in the term

$$k_u^c = k_s / (1 + \zeta^* L_u k_s / k_f). \quad (1.28)$$

here $\zeta^* = (2 + 1/p^*)\alpha$, $\alpha = A_k/a$ and A_k is the Kapitza radius. In Eq. (1.27), p^* is the spect ratio, which for the cluster spanning chain is given by $p^* = R_g/R_p$. In particular, our treatment allows the effect of cluster morphology to be evaluated in terms of the average radius of gyration R_g , the fractal dimensions d_f and chemical dimensions d_c of the aggregates respectively. Following the definition of the fractal

dimension d_f the number of particles in the aggregation is given by $N_{int} = (R_g / R_p)^{d_f}$. Due to number conservation of the nanoparticles $\phi = \phi_{int} \phi_a$, where ϕ_{int} is the volume fraction of the nanoparticles in the aggregate or the cluster. It can be shown that $\phi_{int} = (R_g / R_p)^{1/d_f - 3}$ and $(R_g / R_p)_{max} = \phi^{1/d_f - 3}$ for which $\phi_a = 1$. The number of particles belonging to backbone N_c is defined by the chemical dimension is given by $N_c = (R_g / R_p)^{d_i}$. Where d_i ranges between one and d_f . When $d_i = d_f$ all of the particles belong to the backbone and there are no dead ends. Therefore, the volume fraction of backbone particles ϕ_c in the aggregate is given by $\phi_c = (R_g / R_p)^{d_i - 3}$. The volume fraction of the particles belonging to dead ends ϕ_{nc} is given by

$$\phi_{nc} = \phi_{int} - \phi_c \phi_{int} - \phi_c. \quad (1.29)$$

1.3 Governing equations

The fundamental equations of fluid dynamics are based on the following universal laws of conservation:

1.3.1 Conservation of mass

The equation that results from applying the Conservation of Mass law to a fluid flow is called the continuity equation and mathematically defined as

$$\frac{\partial \rho}{\partial t} + \nabla \cdot (\rho \mathbf{V}) = 0, \quad (1.30)$$

where \mathbf{V} is the fluid velocity. The first term in this equation represents the rate of increase of the density in the control volume and the second term represents the rate of mass flux passing out of the control surface (which surrounds the control volume) per unit volume. The Eq. (1.30) can be rewrite in following form

$$\frac{D\rho}{Dt} + \nabla \cdot (\rho \mathbf{V}) = 0, \quad (1.31)$$

where

$$\frac{D(\)}{Dt} \equiv \frac{\partial(\)}{\partial t} + \mathbf{v} \cdot \nabla(\). \quad (1.32)$$

Eq. (1.30) was derived using the Eulerian approach. In this approach, a fixed control volume is utilized, and the changes to the fluid are recorded as the fluid passes through the control volume. In the alternative Lagrangian approach, the changes to the properties of a fluid element are recorded by an observer moving with the fluid element. The Eulerian viewpoint is commonly used in fluid mechanics. The Eq. (1.31) in Cartesian coordinate system as follow

$$\frac{\partial \rho}{\partial t} + \frac{\partial}{\partial x}(\rho u) + \frac{\partial}{\partial y}(\rho v) + \frac{\partial}{\partial z}(\rho w) = 0, \quad (1.33)$$

where u , v , w represent the x , y , z components of the velocity vector. A flow in which the density of each fluid element remains constant is called incompressible. Mathematically, this implies that

$$\frac{D\rho}{Dt} = 0, \quad (1.34)$$

which reduces Eq. (1.31) to

$$\nabla \cdot \mathbf{V} = 0, \quad (1.1)$$

or

$$\frac{\partial u}{\partial x} + \frac{\partial v}{\partial y} + \frac{\partial w}{\partial z} = 0. \quad (1.2)$$

1.3.2 Conservation of momentum

Equation for the conservation of linear momentum is also known as the Navier-Stokes equation. It is possible to write it in many different forms. One possibility is

$$\rho \frac{D\mathbf{V}}{Dt} = \nabla \cdot \boldsymbol{\tau} + \rho \mathbf{g}. \quad (1.37)$$

In order to be able to use an Eulerian description, material derivative at the left hand side, which is the acceleration vector, can be replaced with the sum of local and convective accelerations to get

$$\rho \left[\frac{\partial \mathbf{V}}{\partial t} + (\mathbf{V} \cdot \nabla) \right] = \nabla \cdot \boldsymbol{\tau} + \rho \mathbf{F}. \quad (1.38)$$

The first term on the right-hand side of Eq. (1.38) is the body force \mathbf{F} per unit volume. If the weight of the fluid is the only body force we can replace \mathbf{F} with the

gravitational acceleration vector g . The second term on the right-hand side of Eq. (1.38) represents the surface forces per unit volume. These forces are applied by the external stresses on the fluid element. The stresses consist of normal stresses and shearing stresses and are represented by the components of the stress tensor. Different fluids are defined by different stress tensor, i. e.,

For Newtonian fluid

$$\tau = -p\mathbf{I} + \mu\mathbf{A}_1, \quad (1.39)$$

where \mathbf{A}_1 is defined as

$$\mathbf{A}_1 = (\text{grad}\mathbf{V}) + (\text{grad}\mathbf{V})', \quad (1.40)$$

For non-Newtonian second grade fluid

$$\tau = -p\mathbf{I} + \mu\mathbf{A}_1 + \alpha_1\mathbf{A}_2 + \alpha_2(\mathbf{A}_1)^2, \quad (1.41)$$

where α_1 and α_2 are material coefficients usually called the normal stress moduli and the kinematic first two Rivlin Ericksen tensors are \mathbf{A}_1 and \mathbf{A}_2 .

For non-Newtonian Power law model

$$\tau = -p\mathbf{I} + K\dot{\gamma}^{n_1}, \quad (1.42)$$

where, K the consistency coefficient, is the shear stress at a shear rate of 1.0 s^{-1} . The parameter K is sometimes referred to as consistency index and the consistency index K is identically equal to the viscosity of the fluid μ . The exponent n_1 , the flow behavior index. For the special case of a Newtonian fluid ($n_1 = 1$), when the magnitude of $n_1 < 1$ the fluid is shear-thinning and when $n_1 > 1$ the fluid is shear-thickening in nature.

1.3.3 Conservation of energy

Energy equation can be written in many different ways, such as the one given below

$$\rho \left[\frac{\partial h_{enthalpy}}{\partial t} + \nabla \cdot (h_{enthalpy} \mathbf{V}) \right] = -\frac{Dp}{Dt} + \nabla \cdot (k\nabla T) + \Phi, \quad (1.43)$$

where $h_{enthalpy}$ is the specific enthalpy which is related to specific internal energy as

$$h_{enthalpy} = e + \frac{P}{\rho}. \quad T \text{ is the absolute temperature and } \Phi \text{ is the dissipation function}$$

representing the work done against viscous force, which is irreversibly convert into internal energy. Pressure term on the right hand side of Eq. (1.43) is usually neglected. To derive this energy equation we considered that the conduction heat transfer is governed by Fourier's law with being the thermal conductivity of the fluid. Also note that radioactive heat transfer and internal heat generation due to a possible chemical or nuclear reaction are neglected. Conservation of energy given in Eq. (1.43) can be simplified by considering the fact that density is constant for incompressible flows. Also using the definition of enthalpy given previously and $dh_{enthalpy} = C_p dT$ and $de = C_v dT$ relation, Eq. (1.43) takes the following form

$$\rho C_p \left[\frac{\partial T}{\partial t} + (\nabla \cdot \mathbf{V}) T \right] = k \nabla^2 T + \Phi, \quad (1.44)$$

where C_p is the specific heat at constant pressure. Note that $C_p \approx C_v$ for incompressible flows.

1.4 Significance of governing parameters on convection flow

When convert the fundamental equations of fluid mechanics into non-dimensional form after applying appropriate transformations, then some parameters are appear like Re , Pr , Gr and Ec etc. Thus Temperature solution for convection can be express as

$$T^* = T^*(x^*, y^*, z^*, t^*; Re, Pr, Gr, Ec). \quad (1.45)$$

The following observations are made:

The Reynolds number is associated with viscous flow while the Prandtl number is heat transfer parameter which is fluid property. The Grashof number represents buoyancy effect and Eckert number is associated with viscous dissipation and is important in high speed flow and very viscous fluids.

The number of parameters can be reduced in two special case: (1) If fluid motion is dominated by force convection (negligible free convection), the Grashof number can

be eliminated (II) If viscous dissipation is negligible, the Eckert number is dropped. Thus under these common conditions the solution is simplified to

$$T^* = T^*(x^*, y^*, z^*, t^*; Re, Pr). \quad (1.46)$$

Similarly, for free convection with negligible dissipation

$$T^* = T^*(x^*, y^*, z^*, t^*; Pr, Gr). \quad (1.47)$$

Having identified the important dimensionless parameter in convection heat transfer is the heat transfer coefficient h and dimensionless heat transfer coefficient hx/k is call Nusselt number. It depend on the location of x it is referred to as local Nusselt number and given by

$$Nu = \frac{hx}{k}. \quad (1.48)$$

Since the temperature depends on four parameters, then local Nusselt number is also depended on same these parameters, for mixed convection with dissipation it express as follow

$$Nu_x = Nu_x(x^*; Re, Pr, Gr, Ec). \quad (1.49)$$

For force and free convection it express as similarly temperature respectively as follow

$$Nu_x = Nu_x(x^*; Re, Pr, Ec), \quad (1.50)$$

$$Nu_x = Nu_x(x^*; Pr, Gr, Ec). \quad (1.51)$$

1.5 Methods of solutions

The nonlinear differential equations, nonlinear boundary conditions, variable coefficient differential equations and coupled differential equations have little chance of getting exact solutions or even semi analytical solutions that is why some numerical techniques have been developed, however analytical and semi analytical solutions are still very important as they provide a stander for checking the accuracy of approximate solutions. Analytical solutions can also be used as a test to verify numerical schemes developed for the study of more complex problems. To find the analytical solutions of nonlinear governing equation, there are various methods available in the existing literature. Few of them are as follows:

1. Homotopy Analysis Method
2. Bvp4c Package
3. Optimal Homotopy Analysis Method

1.5.1 Homotopy analysis method

Most physical problems are inherited nonlinear in nature and cannot be solved by several traditional methods such as perturbation techniques [123] which are mostly based on small parameters either in governing equations or in boundary conditions, called perturbation quantities. The small parameter plays a very important role because it determines not only the accuracy of the perturbation approximations but also the validity of the perturbation method itself. In general, it is not guaranteed that a perturbation result is valid in the whole region for all physical parameters. Therefore, it is necessary to develop some new methods which are independent of small parameters because in physical situation there are many nonlinear problems which do not contain any small parameter, especially those having nonlinearity. To overcome the restrictions of perturbation techniques, some powerful mathematical methods have been recently introduced to eliminate the small parameter, such as artificial parameter method introduced by He [124], Tanh method [125], Jacobi elliptic function method [126] and Adomian decomposition method [127], etc. In principle, all of these methods are based on a so-called artificial parameter in which approximate solutions are expanded into series of such kind of artificial parameter. This artificial parameter is often used in such a way that one can easily get approximation solutions efficiently for a given nonlinear equation. All these traditional methods cannot provide any guarantee for the convergence of approximation series. In 1992, Liao [128] first used the concept of homotopy [129] to obtain analytic approximations of nonlinear equations $N[u(\mathbf{r})] = 0$ by means of constructing a one-parameter family of equations (called the zeroth-order deformation equation)

$$(1-q)\mathcal{L}[\varphi(\mathbf{r};q) - u_0(\mathbf{r})] = qN[\varphi(\mathbf{r};q)], \quad (1.52)$$

where N is a differential operator and $u(\mathbf{r})$ is the unknown function of the independent variable(s) $\mathbf{r} = \{r_1, r_2, r_3, \dots, r_n\}$, \mathcal{L} is an auxiliary linear operator, $u_0(\mathbf{r})$ an

initial approximation of $u(\mathbf{r})$, $q \in [0,1]$ is the embedding parameter. The Taylor series of $\varphi(\mathbf{r};q)$ with respect to the embedding parameter q reads

$$\varphi(\mathbf{r};q) = u_0(\mathbf{r}) + \sum_{l=1}^{\infty} u_l(\mathbf{r}) q^l, \quad (1.53)$$

where

$$u_l(\mathbf{r}) = \frac{1}{l!} \left. \frac{\partial^l \varphi(\mathbf{r};q)}{\partial q^l} \right|_{q=0}. \quad (1.54)$$

In above approach, a liability is appeared that Taylor series could be diverged at $q = 1$. To overcome this disadvantage, Liao [130] introduced in 1997 a nonzero auxiliary parameter \hbar , which is now called the convergence-control parameter, to construct such a two-parameter family of equations (i.e. the zeroth-order deformation equation)

$$(1-q)\mathcal{L}[\varphi(\mathbf{r};q) - u_0(\mathbf{r})] = q\hbar N[\varphi(\mathbf{r};q)]. \quad (1.55)$$

Note that the solution $\varphi(\mathbf{r};q)$ of the above equation is not only dependent upon the embedding parameter q but also the convergence-control parameter \hbar . So, the term $u_l(\mathbf{r})$ given by (1.54) is also dependent upon \hbar and therefore the convergence region of the Taylor series (1.53) is influenced by \hbar . Thus, the auxiliary parameter \hbar provides us a convenient way to ensure the convergence of the Taylor series (1.53) at $q = 1$. For $q = 0$ and $q = 1$, we have

$$\varphi(\mathbf{r};0) = u_0(\mathbf{r}), \quad \varphi(\mathbf{r};1) = u(\mathbf{r}), \quad (1.56)$$

where $u(\mathbf{r})$ is a solution of given differential equation. Thus we can write as

$$u(\mathbf{r}) = u_0(\mathbf{r}) + \sum_{l=1}^{\infty} u_l(\mathbf{r}). \quad (1.57)$$

1.5.2 Bvph2 package

In 2013, Liao [55] developed a homotopy analysis method based package "Bvh2" that can deal with many systems of ordinary differential equations. It can solve different kinds of systems of ODEs, including a system of coupled ODEs in finite interval, a system of coupled ODEs in semi-infinite interval, a system of coupled ODEs with algebraic property at infinity, a system of ODEs with an unknown parameter to be determined and a system of ODEs in different intervals. For

simplicity, the BVP 2.0 needs to input the governing equations along with corresponding boundary conditions and choose proper initial guess of solutions and auxiliary linear operators for under consideration linear sub-problems. In this package, one has great freedom to choose the auxiliary linear operator and initial guess. To run the package, need to define all the inputs of problem properly, except the convergence-control parameters. Usually, the optimal values of the convergence-control parameters are obtained by minimizing the squared residual error. To the accuracies of this package, compare the results of some problem of this thesis with results which obtained by another analytical and numerical method and find good accuracy.

1.5.3 Optimal homotopy analysis method

Lately Niu and Wang [131] developed a very interesting method "Optimal Homotopy Analysis" for approximate solution of nonlinear problems in the frame of the homotopy analysis method. In this method convergence region can be controlled by square residual error instead of non-auxiliary parameter. It is worth to mention that optimal homotopy analysis method is computationally more efficient than the homotopy analysis method. This method is not only valid for small or large values of physical parameter but also achieve the desired solution of resulting equation in less number of iterations as compared to homotopy analysis method. Generalized the homotopy analysis method by constructing such a zeroth-order deformation equation

$$(1 - B(q))\mathcal{L}[\varphi(\mathbf{r}; q) - u_0(\mathbf{r})] = \hbar A(q)N[\varphi(\mathbf{r}; q)], \quad (1.58)$$

where $A(q)$ and $B(q)$ are two analytic functions satisfying. To modify the auxiliary parameter \hbar , one can construct the zeroth-order deformation equation by setting in $H(q) = \hbar A(q)$ and $B(q) = q$ in Liao's Eq. (1.58) to construct the zeroth-order deformation equation

$$(1 - q)\mathcal{L}[\varphi(\mathbf{r}; q) - u_0(\mathbf{r})] = H(q)N[\varphi(\mathbf{r}; q)], \quad (1.59)$$

where $H(q)$ is called the convergence-control function satisfying $H(0) = 0$ and $H(1) \neq 0$. From Eq. (1.59), we have

$$\varphi(\mathbf{r}; 0) = u_0(\mathbf{r}), \quad \varphi(\mathbf{r}; 1) = u(\mathbf{r}), \quad (1.60)$$

when $q = 0$ and $q = 1$, respectively. Thus, as the embedding parameter q increases from 0 to 1, $\varphi(\mathbf{r}; q)$ varies (or deforms) from the initial approximation $u_0(\mathbf{r})$ to the solution $u(\mathbf{r})$ of the original equation $N[u(\mathbf{r})] = 0$. Expand $\varphi(\mathbf{r}; q)$ and the convergence-control function $H(q)$ in Maclaurin's series as

$$\varphi(\mathbf{r}; q) = \sum_{l=0}^{\infty} u_l(\mathbf{r}) q^l, \quad H(q) = \sum_{k=0}^{\infty} h_k q^k, \quad (1.61)$$

where

$$u_l(\mathbf{r}) = \frac{1}{l!} \left. \frac{\partial^l \varphi(\mathbf{r}; q)}{\partial q^l} \right|_{q=0}, \quad h_k(\mathbf{r}) = \frac{1}{k!} \left. \frac{\partial^k H(q)}{\partial q^k} \right|_{q=0}. \quad (1.62)$$

Assuming that the two series in Eq. (1.62) are convergent at $q = 1$, we have,

$$u(\mathbf{r}) = u_0(\mathbf{r}) + \sum_{l=1}^{\infty} u_l(\mathbf{r}), \quad (1.63)$$

When differentiating the zeroth-order deformation original equation l times with respect to the embedding parameter q , then dividing it by $l!$ and finally setting $q = 0$, we gain the so-called l th-order deformation equation for the unknown $u_l(\mathbf{r})$:

$$\mathcal{L}[u_l(\mathbf{r}) - \chi_l u_{l-1}(\mathbf{r})] = \sum_{k=1}^l h_k R_{l-k}(\mathbf{r}), \quad (1.64)$$

where

$$R_{l-k}(\mathbf{r}) = \frac{1}{n!} \left. \frac{\partial^n N[\varphi(\mathbf{r}; q)]}{\partial q^n} \right|_{q=0} \quad (1.65)$$

and

$$\chi_l = \begin{cases} 0, & l \leq 1 \\ 1, & l > 1 \end{cases} \quad (1.66)$$

The n th-order approximation of the solution $u(\mathbf{r})$ can be expressed as which is mathematically dependent upon the convergence-control parameter vector $\mathbf{h}_n = \{h_1, h_2, \dots, h_n\}$. Let

$$\Delta_n(\mathbf{h}_n) = \int_{\omega} (N[\tilde{u}_n(\mathbf{r})])^2 d\omega, \quad (1.67)$$

we denote the square residual error of the governing equation $N[u(\mathbf{r})]=0$ at the n th-order of approximation, where $n=1,2,3$ and so on. At the 1st-order of approximation, the square residual error Δ_1 is only dependent upon h_1 and thus we can gain the “optimal” value of h_1 by solving the nonlinear algebraic equation

$$\frac{d\Delta_1}{dh_1} = 0. \quad (1.68)$$

At the 2nd-order of approximation, the square residual error $\Delta_2(h_1, h_2)$ is a function of both h_1 and h_2 . Because h_1 is known, we can gain the “optimal” value of h_2 by solving one nonlinear algebraic equation

$$\frac{d\Delta_2}{dh_2} = 0. \quad (1.69)$$

Similarly, at the n th-order of approximation, the square residual error Δ_n contains only one unknown convergence-control parameter h_n , whose “optimal” value is determined by a nonlinear algebraic equation

$$\frac{d\Delta_n}{dh_n} = 0, \quad n \geq 1. \quad (1.70)$$

In this way, one can get accurate results at rather high-order of approximation. Note that in homotopy analysis method, $H(q) = hq$ is mostly used, and h is chosen by plotting the h curves whereas in OHAM, the square residual error Δ_n at a given order n of approximation is a function of h and the “optimal” value of the convergence-control parameter h is given by

$$\frac{d\Delta_n}{dh} = 0. \quad (1.71)$$

Chapter 2

Magnetohydrodynamic flow of water and ethylene glycol based nanofluids with natural convection through porous medium

In this chapter, the natural convective boundary layer flow of nanofluids along the vertical cone through porous medium is considered under the effects of magnetic and heat generation. For the nanofluid, water and ethylene contemplated as base fluid and used spherical nanoparticles of copper metal. The governing equations in non-dimensional form are reserved to investigate the nanofluid flow with convective heat transfer profile. Analytical solutions of these equations are gotten by means of HAM. Correlation of Skin friction and heat transfer rate corresponding to active parameters is also presented. The obtained results are illustrated by graphs and tables in order to see the effects of physical parameters.

2.1 Mathematical formulation of the problem

Consider a convective flow of nanofluid along a vertical cone with semi-angle Ω . In the coordinate system, x -axis and y -axis are along and normal to the surface of cone. The origin is occupied at the vertex of the cone as shown in Fig. 2.1.

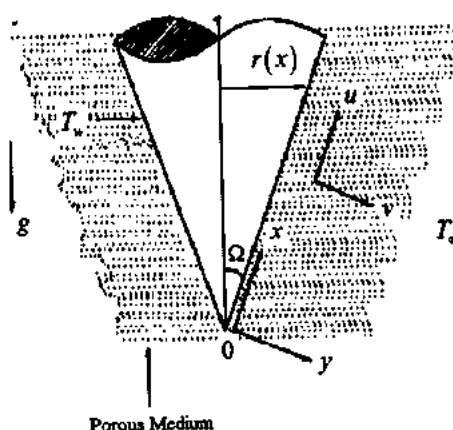


Fig. 2.1. Schematic sketch of vertical cone.

TH-16258

Applying the boundary layer and Boussinesq approximations, the governing equations can be written as

$$\frac{\partial}{\partial x}(ru) + \frac{\partial}{\partial y}(rv) = 0, \quad (2.1)$$

$$\rho_{nf} \left(u \frac{\partial u}{\partial x} + v \frac{\partial u}{\partial y} \right) = \mu_{eff} \frac{\partial^2 u}{\partial y^2} + (\rho\beta)_{nf} g (T - T_\infty) \cos\Omega - \frac{\mu_{nf}}{K_1} u - \sigma_0 \beta_0^2 u, \quad (2.2)$$

$$u \frac{\partial T}{\partial x} + v \frac{\partial T}{\partial y} = \alpha_{nf} \frac{\partial^2 T}{\partial y^2} + \frac{Q_0}{(\rho C_p)_{nf}} (T - T_\infty). \quad (2.3)$$

The corresponding hydrodynamic and thermal boundary conditions are

$$u(x,0) = 0, \quad v(x,0) = 0, \quad u(x,\infty) = 0 \quad (2.4)$$

and

$$T(x,0) = T_w = T_\infty + Cx^n, \quad T(x,\infty) = T_\infty. \quad (2.5)$$

For a thin boundary layer $r = x \sin\Omega$, σ_0 is the electric conductivity and β_0 is the uniform magnetic field strength and K_1 is the permeability. The amount of heat absorbed or generated per unit volume is Q_0 . In the thermal boundary conditions, T_∞ is the temperature far from the surface of the cone, $C > 0$ is constant and n is power law index. Note that the power law thermal boundary condition can also be used for isothermal cases. For instance, when n equal to zero, Eq. (2.5) yields isothermal case. In Eqs. (2.2) and (2.3), the thermal-physical properties for nanofluid are defined in Eqs. (1.3), (1.7), (1.8), (1.10) and (1.16) respectively. The thermal-physical properties of water, ethylene glycol and copper are defined as in table 2.1.

Table 2.1. Thermal-physical properties for nanofluid.

Physical Properties	Water (H_2O)	Ethylene glycol ($C_2H_6O_2$)	Copper (Cu)
ρ (kgm^{-3})	999	1110	8910
C_p ($Jkg^{-1}K^{-1}$)	4180	2400	390
k ($W/m-K$)	0.60	0.26	395
β (K^{-1}) $\times 10^{-5}$	15	65	1.7

By means of the stream function $\psi(x, y)$, which satisfies the continuity equation as follow

$$u = \frac{1}{r} \frac{\partial \psi}{\partial y}, \quad v = -\frac{1}{r} \frac{\partial \psi}{\partial x}. \quad (2.6)$$

Let us introduce the following non-dimensional parameters

$$\begin{aligned} \eta = \frac{y}{x} Ra_x^{1/4}, \quad \psi = \nu_f r Ra_x^{1/4} f(\eta), \quad \theta(\eta) = \frac{T - T_\infty}{T_w - T_\infty}, \\ u = \frac{\nu_f}{x} Ra_x^{1/4} f', \quad v = -\frac{\nu_f}{x} Ra_x^{1/4} \left[\left(\frac{n+7}{4} \right) f + \left(\frac{n-1}{4} \right) \eta f' \right]. \end{aligned} \quad (2.7)$$

Substituting the transformations given in Eq. (2.7) into Eqs. (2.1) to (2.4) and obtain the governing equations in non-dimensional form as follows

$$\frac{\rho_{nf}}{\rho_f} \left[\left(\frac{n+1}{2} \right) f'^2 - \left(\frac{n+7}{4} \right) f f'' \right] = \frac{\mu_{nf}}{\mu_f} (f''' - \Lambda f') - M_1 f' + \frac{(\rho\beta)_{nf}}{(\rho\beta)_f} \theta, \quad (2.8)$$

$$Pr \frac{(\rho C_p)_{nf}}{(\rho C_p)_f} \left[n \theta f' - \left(\frac{n+7}{4} \right) f \theta' \right] = \frac{k_{nf}}{k_f} \theta'' + Q \theta \quad (2.9)$$

along the boundary conditions

$$\left. \begin{aligned} f' = 0, \quad f = 0, \quad \theta = 1 \quad \text{when } \eta = 0 \\ f' = 0, \quad \theta = 0 \quad \text{when } \eta \rightarrow \infty \end{aligned} \right\} \quad (2.10)$$

The following dimensionless quantities are also obtained

$$\left. \begin{aligned} Pr = \frac{\nu_f}{\alpha_f}, \quad Ra_x = \frac{g\beta_f (T_w - T_\infty) x^3 \text{Cos}\Omega}{\alpha_f \nu_f}, \quad \Lambda = \frac{x^2}{K_1 Ra_x^{1/2}}, \\ Q = \frac{Q_0 x^2}{k_f Ra_x^{1/2}}, \quad M_1 = \frac{\sigma_0^2 \beta_0^2}{\mu_f} \sqrt{\frac{x^4}{Ra_x}} \end{aligned} \right\} \quad (2.11)$$

where Ra_x is Rayleigh number, Λ is porosity parameter, Q is the heat generation parameter, M_1 is magnetic parameter and Pr is Prandtl number.

Skin-friction coefficient and local Nusselt number in non-dimensional form are given by

$$Ra_x^{1/4} C_f = 2 \left(\frac{\mu_{nf}}{\mu_f} \right) f''(0) \quad \text{and} \quad Ra_x^{-1/4} Nu_x = - \left(\frac{k_{nf}}{k_f} \right) \theta'(0). \quad (2.12)$$

2.2 Solution of the problem

For the HAM, choose the initial approximation of $f(\eta)$ and $\theta(\eta)$

$$f_0(\eta) = \frac{1}{2} + \frac{1}{2}e^{-2\eta} - e^{-\eta}, \quad \theta_0(\eta) = e^{-\eta}. \quad (2.13)$$

The auxiliary linear operators are

$$\mathcal{L}_1(f) = \frac{d}{d\eta} \left(\frac{d^2 f}{d\eta^2} - f \right), \quad \mathcal{L}_2(\theta) = \frac{d}{d\eta} \left(\frac{d\theta}{d\eta} - \theta \right). \quad (2.14)$$

Construct the zero-order deformation

$$\begin{aligned} (1-q)\mathcal{L}_1[f(\eta, q) - f_0(\eta)] &= q\hbar N_1[f(\eta, q), \theta(\eta, q)], \\ (1-q)\mathcal{L}_2[\theta(\eta, q) - \theta_0(\eta)] &= q\hbar N_2[f(\eta, q), \theta(\eta, q)], \end{aligned} \quad (2.15)$$

$$\left. \begin{aligned} f(\eta, q) = 0, \quad \frac{\partial f(\eta, q)}{\partial \eta} = 0, \quad \theta(\eta, q) = 1 \text{ at } \eta = 0 \\ f(\eta, q) = 0, \quad \theta(\eta, q) = 1 \text{ at } \eta \rightarrow \infty \end{aligned} \right\} \quad (2.16)$$

The non-linear operators N_1 and N_2 are

$$\begin{aligned} N_1[f(\eta, q), \theta(\eta, q)] &= -\frac{\rho_{nf}}{\rho_f} \left[\left(\frac{n+1}{2} \right) f^2 - \left(\frac{n+7}{4} \right) f f'' \right] \\ &+ \frac{\mu_{nf}}{\mu_f} (f''' - \Lambda f') - M_1 f' + \frac{(\rho\beta)_{nf}}{(\rho\beta)_f} \theta, \end{aligned} \quad (2.17)$$

$$N_2[f(\eta, q), \theta(\eta, q)] = -Pr \frac{(\rho C_p)_{nf}}{(\rho C_p)_f} \left[n\theta f' - \left(\frac{n+7}{4} \right) f \theta' \right] + \frac{k_{nf}}{k_f} \theta'' + Q\theta. \quad (2.18)$$

In the above expressions, \hbar is convergence control parameter. For $q = 0$

$$f(\eta, 0) = f_0(\eta), \quad \theta(\eta, 0) = \theta_0(\eta) \quad (2.19)$$

and $q = 1$

$$f(\eta, 1) = f(\eta) \quad \theta(\eta, 1) = \theta(\eta). \quad (2.20)$$

When embedding parameter q diverges from 0 to 1, then $f(\eta, q)$ and $\theta(\eta, q)$ varies from initial guess $f_0(\eta)$ and $\theta_0(\eta)$ to final $f(\eta)$ and $\theta(\eta)$ solution.

Let expand $f(\eta, q)$ and $\theta(\eta, q)$ in Maclaurin's series as

$$f(\eta, q) = f_0(\eta) + \sum_{l=1}^{\infty} f_l(\eta) q^l, \quad \theta(\eta, q) = \theta_0(\eta) + \sum_{l=1}^{\infty} \theta_l(\eta) q^l, \quad (2.21)$$

where

$$f_l(\eta) = \frac{1}{l!} \left. \frac{\partial f^l(\eta, q)}{\partial q^l} \right|_{q=0}, \quad \theta_l(\eta) = \frac{1}{l!} \left. \frac{\partial \theta^l(\eta, q)}{\partial q^l} \right|_{q=0}. \quad (2.22)$$

Differentiating l -times to zeroth-order deformation Eqs. (2.15) and (2.16) with respect to the q and dividing it by $l!$ then putting $q=0$ and gain l th-order deformation expression for $f_l(\eta)$ and $\theta_l(\eta)$ as follow

$$\mathcal{L}_1[f_l(\eta) - \chi_l f_{l-1}(\eta)] = h_1 R1_l(\eta), \quad (2.23)$$

$$\mathcal{L}_2[\theta_l(\eta) - \chi_l \theta_{l-1}(\eta)] = h_2 R2_l(\eta), \quad (2.24)$$

$$\left. \begin{aligned} f_l(\eta, q) = 0, \quad \frac{\partial f_l(\eta, q)}{\partial \eta} = 0, \quad \theta_l(\eta, q) = 0 \quad \text{at } \eta = 0 \\ f_l(\eta, q) = 0, \quad \theta_l(\eta, q) = 0 \quad \text{at } \eta \rightarrow \infty \end{aligned} \right\}, \quad (2.25)$$

where

$$\begin{aligned} R1_l(\eta) = & -\frac{\rho_{nf}}{\rho_f} \left[\left(\frac{n+1}{2} \right) \sum_{k=0}^l f_k f_{l-k} - \left(\frac{n+7}{4} \right) \sum_{k=0}^l f_k f_{l-k}'' \right] \\ & + \frac{\mu_{nf}}{\mu_f} (f_l'' - N f_l') - M_1 f_l' + \frac{(\rho\beta)_{nf}}{(\rho\beta)_f} \theta_l \end{aligned} \quad (2.26)$$

and

$$R2_m(\eta) = -\text{Pr} \frac{(\rho C_p)_{nf}}{(\rho C_p)_f} \left[n \sum_{k=0}^l \theta_k f_{l-k} - \left(\frac{n+7}{4} \right) \sum_{k=0}^l f_l \theta_{l-k}' \right] + \frac{k_{nf}}{k_f} \theta_l'' + Q \theta_l. \quad (2.27)$$

The l th-order approximation of the solution can be expressed as

$$f(\eta) = f_0(\eta) + \sum_{k=1}^l f_k(\eta), \quad (2.28)$$

$$\theta(\eta) = \theta_0(\eta) + \sum_{k=1}^l \theta_k(\eta). \quad (2.29)$$

In above, the expressions (2.28) and (2.29) contain the auxiliary parameter h . In HAM, the convergence region and rate of approximations are strongly dependent upon h . The Fig. 2.12 shows the h -curves to find the range of h for the velocity and temperature fields.

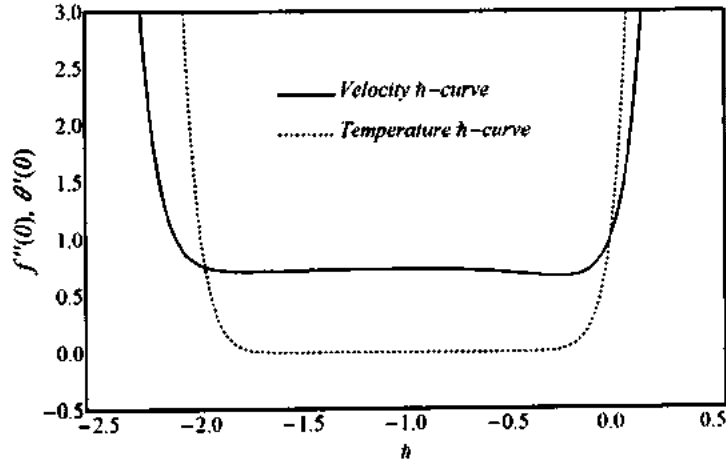


Fig. 2.2. h -curves of the velocity and temperature fields at 20-th-order approximations.

The range for permissible value of h , for the velocity is $-2.0 \leq h \leq -0.5$ and for the temperature is $-1.8 \leq h \leq -0.3$. Moreover, the error of norm 2 of the two successive approximations over $[0,1]$ at 20-th iterations are given by

$$E_f = \sqrt{\frac{1}{21} \sum_{i=0}^{15} (f(i/20))^2}, \quad (2.30)$$

$$E_\theta = \sqrt{\frac{1}{21} \sum_{i=0}^{15} (\theta(i/20))^2}.$$

It is realized that the error is minimum at $h = -0.8$ for the velocity and temperature as shown in table 2.2.

Table 2.2. Residual error at different orders of approximation when $\phi = 5\%$, $\Lambda = 0.5$, $M_1 = 0.9$, $Q = 0.1$ and $n = 1$.

Order of approximation	$f(\eta)$	$\theta(\eta)$
2	5.627×10^{-2}	3.625×10^{-3}
6	2.268×10^{-5}	2.125×10^{-6}
10	2.279×10^{-6}	1.339×10^{-9}
14	5.096×10^{-8}	1.221×10^{-10}
18	3.533×10^{-12}	3.551×10^{-13}
20	2.669×10^{-14}	2.918×10^{-15}

The mathematical expression of solutions at first iteration for velocity and temperature are given as

$$f' = \left(1 + \frac{671C_1}{750} - \frac{64C_2}{75} + \frac{16M_1}{75} + \frac{13C_1n}{150} - \frac{14C_1\eta}{25} \right) e^{-\eta} + \left(-1 - \frac{104C_1}{75} + \frac{64C_2}{75} - \frac{16M_1}{75} - \frac{16M_1\Lambda}{75} \right) e^{-2\eta} + \left(\frac{31C_1}{50} + \frac{C_1n}{50} \right) e^{-3\eta} - \frac{16}{125} C_1 e^{-4\eta}, \quad (2.31)$$

$$\theta = \left(1 + \frac{4459C_4nPr}{4800} - \frac{343C_4Pr}{4800} + \frac{49C_5\eta}{100} - \frac{343C_4Pr\eta}{400} - \frac{49C_4Prn\eta}{400} \right) e^{-\eta} + \left(-\frac{343C_4Pr}{300} + \frac{49C_4nPr}{300} \right) e^{-2\eta} + \left(\frac{343C_4Pr}{1600} - \frac{147C_4nPr}{1600} \right) e^{-3\eta}, \quad (2.32)$$

where $C_1 = \frac{\rho_{nf}}{\rho_f}$, $C_2 = \frac{\mu_{nf}}{\mu_f}$, $C_3 = \frac{(\rho\beta)_{nf}}{(\rho\beta)_f}$, $C_4 = \frac{(\rho C_p)_{nf}}{(\rho C_p)_f}$ and $C_5 = \frac{k_{nf}}{k_f}$.

2.3 Results and discussion

In this segment, we have discussed the analytical and numerical results for embedding parameters. The important finding in this communication is the combined effects of magnetohydrodynamic and porosity along with variable wall temperature boundary condition on water and ethylene glycol base nanofluid. To see the effects of particle volume fraction on velocity and temperature profiles with water and ethylene glycol base nanofluid, Figs. 2.3 and 2.4 have been displayed. It is observed that the increment in particle volume fraction leads to a diminution in velocity field and enhancement in temperature profile. A maximum decrease in velocity profile is observed in ethylene glycol, while the maximum increase is noticed by water in temperature profile. The Figs. 2.5 and 2.6 have been prepared to explain the effects of magnetohydrodynamic parameter. It is found the diminution in the velocity by increasing of magnetohydrodynamic parameter whereas temperature profile is enhanced. It is in accordance with the physical expectation because in base fluid the bid of transverse magnetic field will upshot for a resistive type force, known as Lorentz force, which resist the fluid flow and as resulting velocity decrease with an increase in magnetohydrodynamic parameter. Figs. 2.7 and 2.8 illustrate the impact of porosity parameter on velocity and temperature expressions. The velocity field declines and temperature rise by increasing the values of porosity parameter. It is also

found that ethylene glycol base nanofluid has minimum velocity and temperature when compared with water base nanofluid. The heat generation parameter variation analysis is carried out in Figs. 2.9 and 2.10. The results show utmost enhancement in velocity and temperature of the nanofluid. The effects of temperature power index on velocity and temperature fields are shown in Figs. 2.11 and 2.12. These Figs. elucidate that velocity and temperature of nanofluid decrease by increasing the temperature power index.

The second set of results not only displays the effects of sundry parameters, but also provides a comparison between sundry parameters on Skin friction and Nusselt number for two different base fluid contained nanofluid as shown in tables 2.3 to 2.7. The effects of nanoparticles volume fraction on Skin friction and Nusselt number are presented in table 2.3. It is evident from results that rate of heat transfer enhances when nanoparticles volume fraction increases. It is also observed that maximum heat transfer rate is achieved in case of water base nanofluid as compared to ethylene glycol. The heat transfer rate respectively increases 7.13% and 5.66% for water and ethylene glycol at 10% volume fraction. On the other hand, when the particle volume fraction upturns, the Skin friction coefficient increases for both nanofluids. Table 2.4 shows the effects of magnetohydrodynamic parameter on Skin friction and heat transfer rate. This table reflects that an increase of the magnetohydrodynamic parameter decreases the Skin friction and heat transfer rate of nanofluids. In table 2.4, it is perceived that Skin friction is maximum reduced by ethylene glycol as compared to water base nanofluid. Table 2.5 depicts the impact of porosity parameter on Skin friction and heat transfer. The Skin friction and heat transfer rate reduce as the porosity parameter culminates respectively. Table 2.6 exhibits the result of Skin friction and heat transfer rate collected by multiple variations of heat generation parameter. In this table, it is seen that the Skin friction increases by increasing the heat generation parameter whereas heat transfer rate decreases when considered 5% volume fractions. Table 2.7 demonstrates that by increasing the temperature power index, the Skin friction declines and heat transfer rate increases by keeping other parameters fixed.

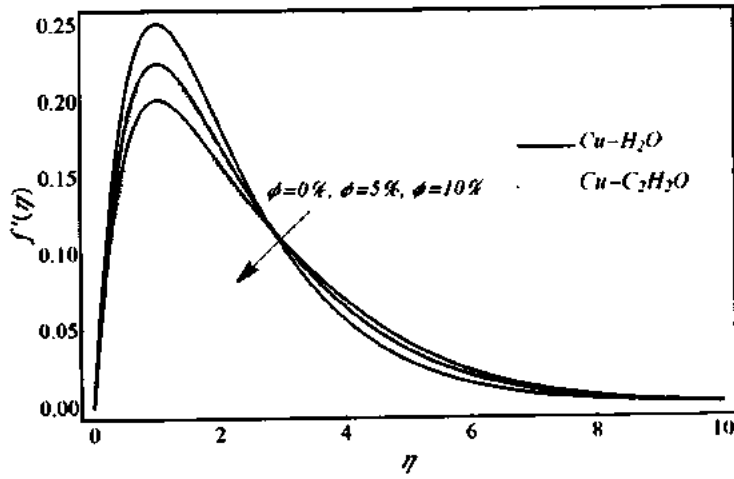


Fig. 2.3. Effects of nanoparticles volume-fraction on velocity field.

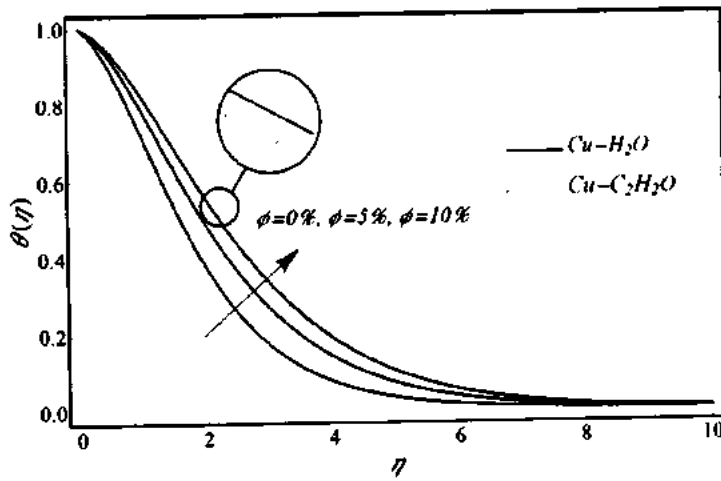


Fig. 2.4. Effects of nanoparticles volume fraction on temperature field.

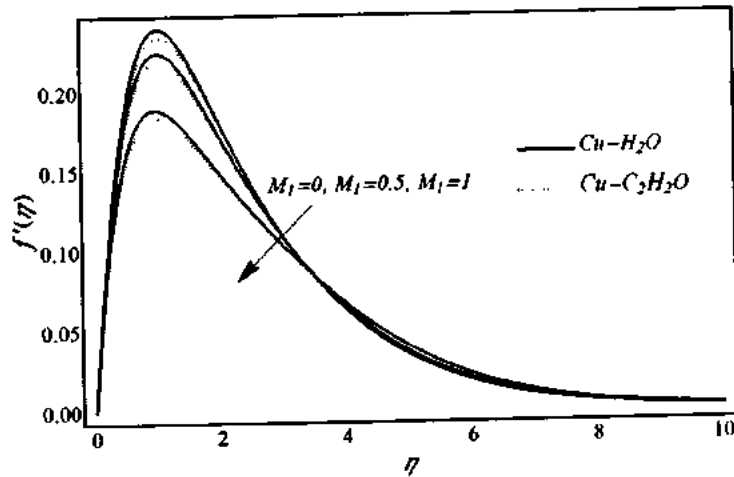


Fig. 2.5. Effects of magnetohydrodynamic parameter on velocity field.

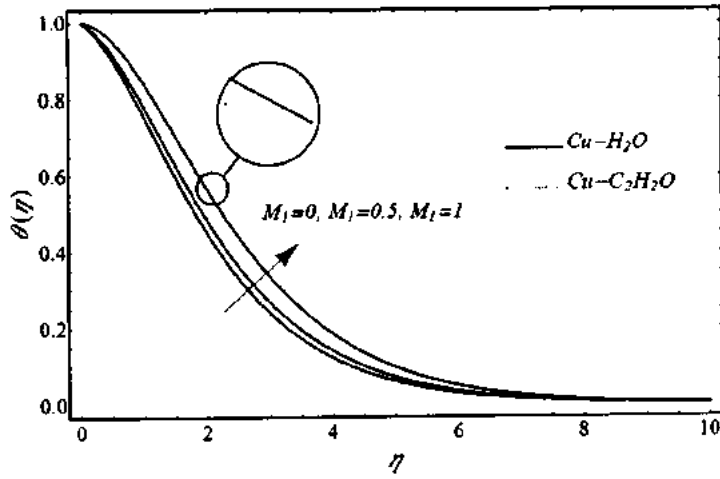


Fig. 2.6. Effects of magnetohydrodynamic parameter on temperature field.

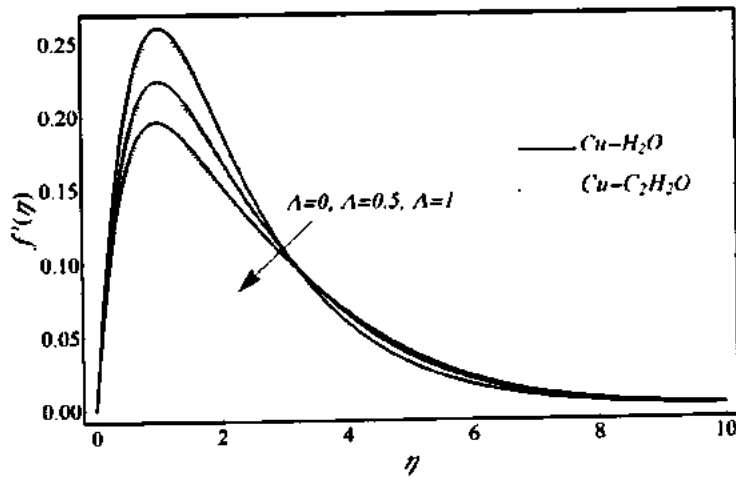


Fig. 2.7. Effects of porosity parameter on velocity field.

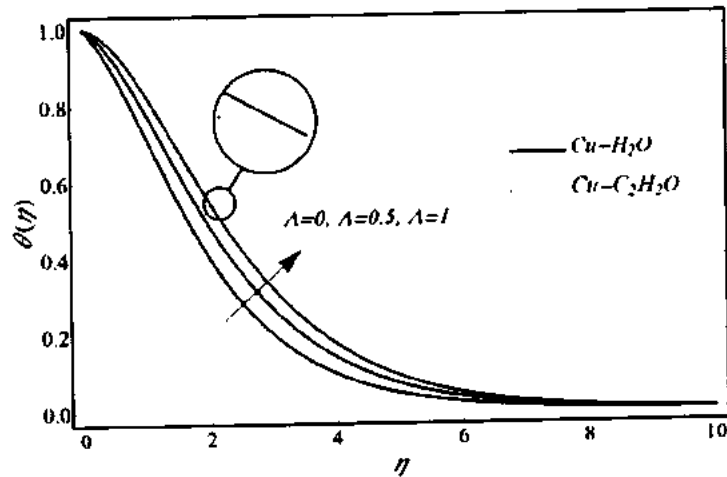


Fig. 2.8. Effects of porosity parameter on temperature field.

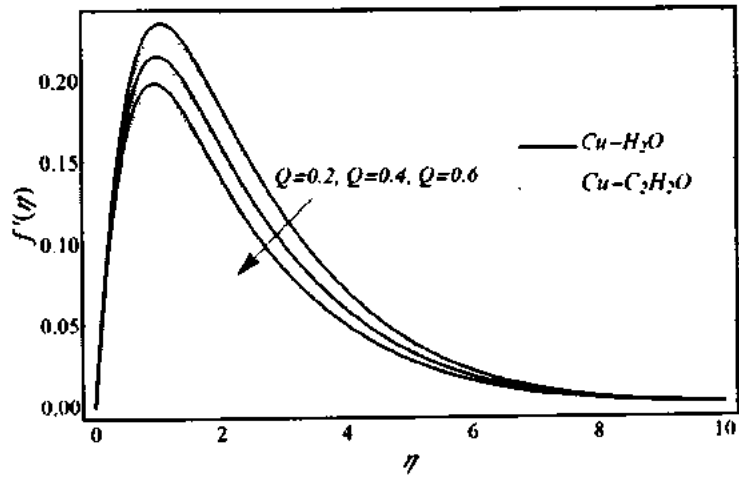


Fig. 2.9. Effects of heat generation parameter on velocity field.

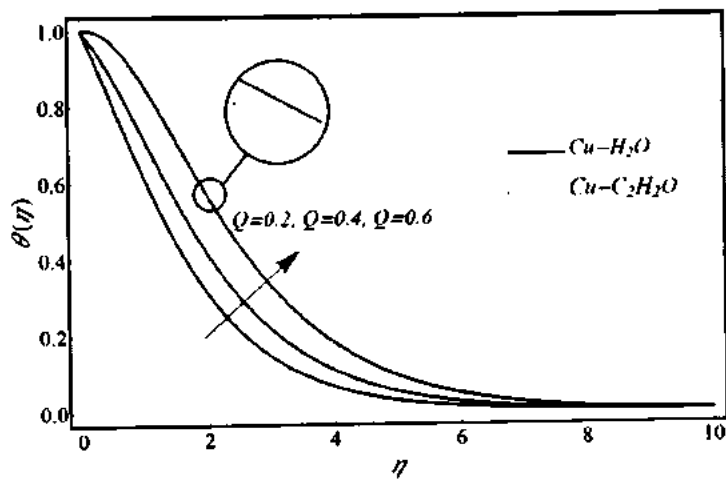


Fig. 2.10. Effects of heat generation parameter on temperature field.

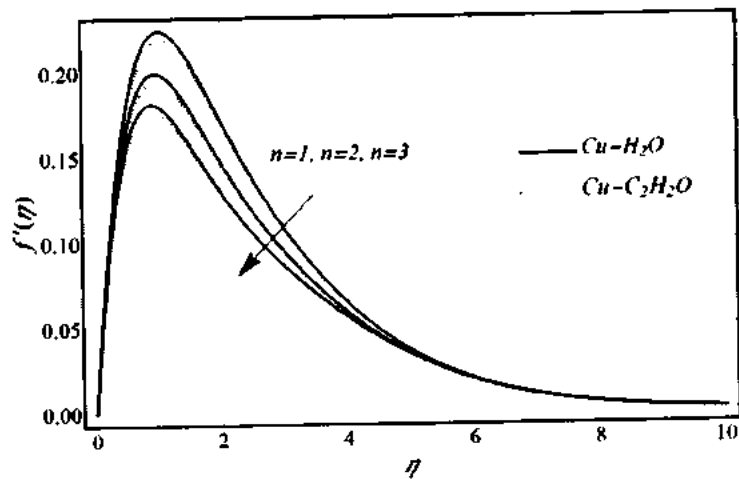


Fig. 2.11. Effects of temperature power index on velocity field.

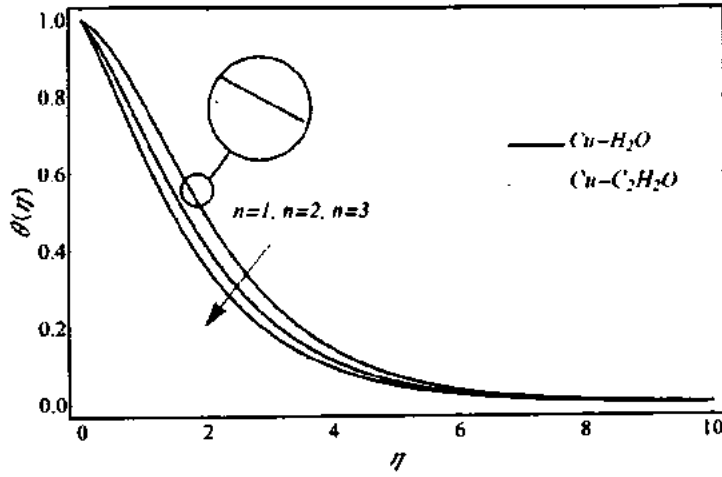


Fig. 2.12. Effects of temperature power index on temperature field.

Table 2.3. Effects of nanoparticles volume fraction on Skin friction and Nusselt number when $M_1 = 0.9$, $\Lambda = 0.5$, $Q = 0.1$ and $n = 1$.

	ϕ	$Cu-H_2O$	$Cu-C_2H_6O_2$
$Ra_x^{1/4} C_f$	0%	1.15914	1.15914
	5%	1.21782	1.18567
	10%	1.28151	1.19695
$Ra_x^{-1/4} Nu$	0%	0.51542	0.51542
	5%	0.53280	0.53202
	10%	0.55223	0.54462

Table 2.4. Effects of magneto hydrodynamic parameter on Skin friction and Nusselt number when $\phi = 5\%$, $\Lambda = 0.5$, $Q = 0.1$ and $n = 1$.

	M_1	$Cu-H_2O$	$Cu-C_2H_6O_2$
$Ra_x^{1/4} C_f$	0	1.26034	1.21375
	0.5	1.21782	1.18567
	1	1.10862	1.06325
$Ra_x^{-1/4} Nu$	0	0.54870	0.54547
	0.5	0.53280	0.53202
	1	0.48226	0.48125

Table 2.5. Effects of porosity parameter on Skin friction and Nusselt number when $\phi = 5\%$, $\Lambda = 0.5$, $M_1 = 0.9$, $Q = 0.1$ and $n = 1$.

	Λ	$Cu-H_2O$	$Cu-C_2H_6O_2$
$Ra_x^{1/4}C_f$	0	1.3136	1.3067
	0.5	1.2178	1.1857
	1	1.1299	1.0910
$Ra_x^{-1/4}Nu$	0	0.5782	0.5782
	0.5	0.5328	0.5320
	1	0.4922	0.4912

Table 2.6. Effects of heat generation parameter on Skin friction and Nusselt number when $\phi = 5\%$, $\Lambda = 0.5$, $M_1 = 0.9$ and $n = 1$.

	Q	$Cu-H_2O$	$Cu-C_2H_6O_2$
$Ra_x^{1/4}C_f$	0	1.1883	1.1450
	0.1	1.2178	1.1856
	1.2	1.2734	1.2088
$Ra_x^{-1/4}Nu$	0	0.6067	0.6063
	0.1	0.5328	0.5320
	0.2	0.4511	0.4536

Table 2.7. Effects of power law index on Skin friction and Nusselt number when $\phi = 5\%$, $\Lambda = 0.5$, $M_1 = 0.9$ and $Q = 0.1$.

	n	$Cu-H_2O$	$Cu-C_2H_6O_2$
$Ra_x^{1/4}C_f$	1	1.2178	1.1857
	2	1.1551	1.1193
	3	1.0906	1.0694
$Ra_x^{-1/4}Nu$	1	0.5328	0.5320
	2	0.6041	0.6057
	3	0.6589	0.6578

2.4 Conclusions

In this chapter, magnetohydrodynamic influence on water/ethylene glycol base nanofluids flow through porous medium is investigated. The influence of different parameters on velocity, temperature, Skin-friction coefficient and Nusselt number for different two base fluids contained nanofluids over the cone are analyzed. It is realized that velocity decreases as increasing the particle volume fraction, magnetic, porosity and power law index parameters. In context of temperature, when the particle volume fraction, magnetic, porosity, heat generation parameters are upturn then temperature of nanofluids are amplified. Under the effects of these parameters, water base nanofluid gain maximum velocity and temperature as compared to ethylene glycol base nanofluid. With increasing the effects of magnetic, porosity and power law index, the shear stress at wall is decreased. On the other hand, improvement in heat transfer rate at wall is found by enhancing the volume fraction of particles and power law index for both fluids.

Chapter 3

Shape effects of nanosize particles in $Cu-H_2O$ nanofluid on entropy generation

In this chapter, a mathematical model is analyzed to study the convective flow of nanofluid along a vertical cone. For the water base nanofluid, consider copper nanoparticles of different shapes like platelet, cylinder and brick. Hamilton–Crosser model is used to calculate the effective thermal conductivities for different shapes. Simultaneous effects of porous medium, radiation, magnetohydrodynamic and power law index effects are also taken into account. The shape of nanosize particles on entropy generation with based fluid is also considered. The nonlinear coupled equations are solved analytically. The calculations are done for various governing parameters like Prandtl number, power law index, Rayleigh number, porosity parameter, radiation parameter and magnetic parameter. The physical interpretations of obtained results are illustrated with graphs and tables. In addition, the Nusselt number and Skin friction correlation corresponding to active parameters are also analyzed in this investigation.

3.1 Mathematical formulation of the problem

Consider water based nanofluid flow containing copper (Cu) nanoparticles of different shapes likes platelets, cylinders and bricks over cone. The mathematical description of geometry of the problem is shown in Fig. 2.1. The governing equations under the Boussinesq and boundary layer approximations can be transcribed as

$$\frac{\partial}{\partial x}(ru) + \frac{\partial}{\partial y}(rv) = 0, \quad (3.1)$$

$$\rho_{nf} \left(u \frac{\partial u}{\partial x} + v \frac{\partial u}{\partial y} \right) = \mu_{nf} \frac{\partial^2 u}{\partial y^2} + (\rho\beta)_{nf} g(T - T_\infty) \text{Cos}\Omega - \frac{\mu_{nf}}{K_1} u - \sigma_0 \beta_0^2 u, \quad (3.2)$$

$$u \frac{\partial T}{\partial x} + v \frac{\partial T}{\partial y} = \alpha_{nf} \frac{\partial^2 T}{\partial y^2} - \frac{1}{(\rho C_p)_{nf}} \frac{\partial q}{\partial y}. \quad (3.3)$$

The boundary conditions for the considered problem are

$$\left. \begin{aligned} v(x,0) = 0, \quad u(x,0) = 0, \quad u(x,\infty) = 0, \\ T(x,0) = T_w = T_\infty + Cx^n, \quad T(x,\infty) = T_\infty \end{aligned} \right\} \quad (3.4)$$

By using the Rossel approximation, the radioactive heat flux q_r can be written as

$$q_r = -\frac{4\sigma^*}{3k^*} \frac{\partial T^4}{\partial y}. \quad (3.5)$$

In above, σ^* is Stefan-Boltzmann constant. The k^* is mean absorption coefficient. By expanding Taylor's series of T^4 about T_∞ and ignoring higher order terms, we obtain

$$T^4 \approx 4T_\infty^3 T - 3T_\infty^4. \quad (3.6)$$

In Eqs. (3.2) and (3.3), the physical properties for nanofluid are defined in Eqs. (1.3), (1.7), (1.8), (1.11) and (1.17) respectively. For different shapes of nanoparticles, the values of sphericities and shapes factors are given in the following table 3.1.

Table 3.1. The values of sphericity and shape factor of different nanoparticles [132].

Nanoparticles shape	Aspect satio	Sphericity (Ψ)	Shape sactor (n^*)
Platelet	1:1/8	0.52	5.7
Cylinder	1:8	0.62	4.9
Brick	1:1:1	0.81	3.7

The thermal conductivities k_{nf} of copper nanofluids with different particle shapes measured at temperature (20°C) are presented as a function of nanoparticle volume fraction ϕ . The thermal conductivity enhancement which is defined as k_{nf}/k_f ratio, where k_f is the thermal conductivity of the base liquid (H_2O). At tested particle concentrations thermal conductivity of nanofluid linearly rises with increasing in nanoparticle volume fraction. It is also observed that the suspensions of particles with high shape factor should have higher thermal conductivities according to said model of conductivity as shown in Fig. 3.1.

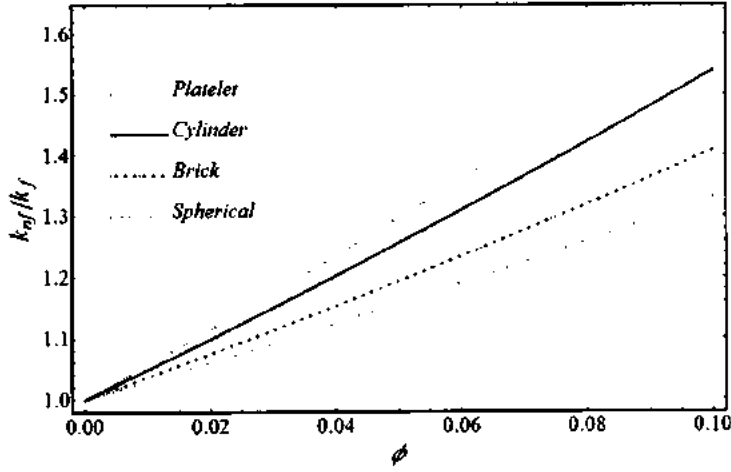


Fig. 3.1. Thermal conductivity of copper nanofluids by Hamilton-Crosser model for corresponding particle shapes.

Using the dimensionless variables Eq. (2.7) and substitute in Eqs. (3.1) to Eqs. (3.4).

Eqs. (3.1) to (3.4) take the forms

$$\frac{\rho_{nf}}{\rho_f} \left[\left(\frac{n+1}{2} \right) f'^2 - \left(\frac{n+7}{4} \right) f f'' \right] = \frac{\mu_{nf}}{\mu_f} (f''' - N f') - M_1 f' + \frac{(\rho\beta)_{nf}}{(\rho\beta)_f} \theta, \quad (3.7)$$

$$\text{Pr} \frac{(\rho C_p)_{nf}}{(\rho C_p)_f} \left[n \theta f' - \left(\frac{n+7}{4} \right) f \theta' \right] = \frac{k_{nf}}{k_f} (1+N) \theta''. \quad (3.8)$$

The boundary conditions are

$$\left. \begin{aligned} f = 0, \quad f' = 0, \quad \theta = 1 \quad \text{when } \eta = 0 \\ f' = 0, \quad \theta = 0 \quad \text{when } \eta \rightarrow \infty \end{aligned} \right\}. \quad (3.9)$$

where $N = -\frac{16\sigma * T_\infty^3}{3k_f k^*}$ is radiation parameter.

The dimensionless Skin friction coefficient C_f and local Nusselt number Nu_x , are demarcated in Eqs. (2.12).

Entropy generation analysis

The local volumetric rate of entropy generation for nanofluid flow in the presence of MHD and thermal radiation is defined as [133,134]

$$S_{gen} = \underbrace{\frac{1}{T^2} \left[k_{nf} \left(\frac{\partial T}{\partial y} \right)^2 + \frac{16\sigma T_\infty^3}{3k^*} \left(\frac{\partial T}{\partial y} \right)^2 \right]}_{HFI} + \underbrace{\frac{\mu_{nf}}{T} \left(\frac{\partial u}{\partial y} \right)^2 + \frac{\mu_{nf}}{TK} u^2 + \frac{\sigma B_0^2}{T} u^2}_{FFI}. \quad (3.10)$$

The Eq. (3.10) clearly illustrates the contributions of different sources for entropy generation. In the above expression, HFI is irreversibility as a result of heat transfer and FFI is the impact of fluid friction irreversibility. In terms of the primitive variables HFI and FFI become

$$HFI = \left(\frac{k_{nf}}{k_f} + N \right) \left[\frac{k_f (T_w - T_\infty) Gr^{\frac{1}{2}}}{x^2 ((T_w - T_\infty)\theta + T_\infty)^2} \theta' \right], \quad (3.11)$$

$$FFI = \frac{\mu_f^3 Ra_x^{\frac{1}{2}}}{x^4 \rho_f} \left[\frac{M_1 f'^2}{(T_w - T_\infty)\theta + T_\infty} + \frac{f'' + \Lambda f'^2}{(1-\phi)^{2.5} ((T_w - T_\infty)\theta + T_\infty)} \right], \quad (3.12)$$

where T_w and T_∞ are measured in degree of Kelvin.

The Bejan number Be illustrates the ration of entropy generation caused by heat transfer irreversibility to the total entropy generation. The value of Be more/less than 0.5 indicates the influence of HFI or FFI in total irreversibility. The value of $Be = 1$ express domination of HFI mechanism while $Be = 0$ representing no HFI role in the total entropy production. This most important physical quantity Be is defined as

$$Be = \frac{HFI}{HFI + FFI}. \quad (3.13)$$

3.2 Solution of the problem

In this section analytical solutions will be determined for the velocity and temperature. For the solution of Eqs. (3.7) to (3.9), used HAM.

Choose $f_0(\eta)$ and $\theta_0(\eta)$

$$f_0(\eta) = \frac{1}{2} + \frac{1}{2} e^{-2\eta} - e^{-\eta}, \quad \theta_0(\eta) = e^{-\eta}, \quad (3.14)$$

as the initial approximation of velocity and temperature. Further choose the following linear operators defined by

$$\mathcal{L}_1 = \frac{d^3}{d\eta^3} - \frac{d}{d\eta}, \quad \mathcal{L}_2 = \frac{d^2}{d\eta^2} - 1. \quad (3.15)$$

Introducing the zeroth-order deformation as follows

$$(1-q)\mathcal{L}_1[f(\eta,q) - f_0(\eta)] = q\hbar N_3[f(\eta,q), \theta(\eta,q)], \quad (3.16)$$

$$(1-q)\mathcal{L}_2[\theta(\eta,q) - \theta_0(\eta)] = q\hbar N_4[f(\eta,q), \theta(\eta,q)], \quad (3.17)$$

$$\left. \begin{aligned} f(0, q) = 0, \quad \frac{\partial f(0, q)}{\partial \eta} = 0, \quad f(\infty, q) = 0 \\ \theta(0, q) = 1, \quad \theta(\infty, q) = 0 \end{aligned} \right\} \quad (3.18)$$

The non-linear operators N_3 and N_4 are defined by

$$\begin{aligned} N_3[f(\eta, q), \theta(\eta, q)] = & -\frac{\rho_{nf}}{\rho_f} \left[\left(\frac{n+1}{2} \right) f'^2 - \left(\frac{n+7}{4} \right) ff'' \right] \\ & + \frac{\mu_{nf}}{\mu_f} (f''' - \Lambda f') - M_1 f' + \frac{(\rho\beta)_{nf}}{(\rho\beta)_f} \theta, \end{aligned} \quad (3.19)$$

$$N_4[f(\eta, q), \theta(\eta, q)] = \text{Pr} \frac{(\rho C_p)_{nf}}{(\rho C_p)_f} \left[n\theta f' - \left(\frac{n+7}{4} \right) f\theta' \right] - \frac{k_{nf}}{k_f} (1+N)\theta''. \quad (3.20)$$

For $q = 0$ and $q = 1$, we have

$$\begin{aligned} f(\eta, 0) = f_0(\eta), \quad \theta(\eta, 0) = \theta_0(\eta), \\ f(\eta, 1) = f(\eta), \quad \theta(\eta, 1) = \theta(\eta). \end{aligned} \quad (3.21)$$

The $f(\eta, q)$ and $\theta(\eta, q)$ can be written as

$$f(\eta, q) = f_0(\eta) + \sum_{l=1}^{\infty} f_l(\eta) q^l, \quad (3.22)$$

$$\theta(\eta, q) = \theta_0(\eta) + \sum_{l=1}^{\infty} \theta_l(\eta) q^l, \quad (3.23)$$

where

$$\theta_l(\eta) = \frac{1}{l!} \frac{\partial \theta(\eta, q)}{\partial q^l} \Big|_{q=0}, \quad f_l(\eta, q) = \frac{1}{l!} \frac{\partial f(\eta, q)}{\partial q^l} \Big|_{q=0}. \quad (3.24)$$

The convergence of Eq. (3.24) depends on the auxiliary parameter h , therefore, elect the h in this way that it convergent at $q = 1$. In view of Eq. (3.24) finally we have

$$f(\eta, q) = f_0(\eta) + \sum_{l=1}^{\infty} f_l(\eta), \quad (3.25)$$

$$\theta(\eta, q) = \theta_0(\eta) + \sum_{l=1}^{\infty} \theta_l(\eta). \quad (3.26)$$

The l th order deformation problems of Eqs. (3.16) to (3.18) are

$$\left. \begin{aligned} \mathcal{L}_l[f_l(\eta, q) - \chi_l f_{l-1}(\eta, q)] = h R l_l(\eta, q) \\ f_l(0, q) = 0, \quad f'_l(0, q) = 0, \quad f_l(\infty, q) = 0 \end{aligned} \right\} \quad (3.27)$$

$$\left. \begin{aligned} \mathcal{L}_2[\theta_l(\eta, q) - \chi_l \theta_{l-1}(\eta, q)] &= \hbar R2_l(\eta, q) \\ \theta_l(0, q) = 0, \quad \theta_l(\infty, q) &= 0 \end{aligned} \right\}, \quad (3.28)$$

where

$$\begin{aligned} R1_l(\eta, q) &= -\frac{\rho_{nf}}{\rho_f} \left(\left(\frac{n+1}{2} \right) \sum_{k=0}^l f'_k f'_{l-k} - \left(\frac{n+7}{4} \right) \sum_{k=0}^l f_k f''_{l-k} \right) \\ &+ \frac{\mu_{nf}}{\mu_f} (f'''_l - N f'_l) - M_1 f'_l + \frac{(\rho C_p)_{nf}}{(\rho C_p)_f} \theta_l, \end{aligned} \quad (3.29)$$

$$R2_l(\eta, q) = \text{Pr} \frac{(\rho C_p)_{nf}}{(\rho C_p)_f} \left[n \sum_{k=0}^l \theta_l f'_{l-k} - \left(\frac{n+7}{4} \right) \sum_{k=0}^l f_l \theta'_{l-k} \right] - \frac{k_{nf}}{k_f} (1+N) \theta'_l. \quad (3.30)$$

In HAM, the convergence region and rate of approximations are strongly dependent upon control parameter \hbar . It realizes that the minimum error is occurred at $\hbar = -0.772$. The results for velocity and temperature at the first iteration of package are obtained as

$$f' = C_6 e^{-\eta} + C_7 e^{-2\eta} + C_8 e^{-3\eta} + C_9 e^{-4\eta} + C_{10} e^{-5\eta}, \quad (3.31)$$

$$\theta = C_{11} e^{-\eta} + C_{12} e^{-2\eta} + C_{13} e^{-3\eta} + C_{14} e^{-4\eta}. \quad (3.32)$$

The results for velocity and temperature at the second iteration of package are given as

$$f' = C_{15} e^{-\eta} + C_{16} e^{-2\eta} + C_{17} e^{-3\eta} + C_{18} e^{-4\eta} + C_{19} e^{-5\eta} + C_{20} e^{-6\eta} + C_{21} e^{-7\eta} + C_{22} e^{-8\eta}, \quad (3.33)$$

$$\theta = C_{23} e^{-\eta} + C_{24} e^{-2\eta} + C_{25} e^{-3\eta} + C_{26} e^{-4\eta} + C_{27} e^{-5\eta} + C_{28} e^{-6\eta} + C_{29} e^{-7\eta}. \quad (3.34)$$

The coefficients $C_6 - C_{29}$ can be easily found through the routine calculations.

3.3 Results and discussion

To see the effects of emerging parameters of interest on flow quantities such as velocity, temperature and volume-fraction of nanoparticles. Figs. 3.2 to 3.13 have been prepared for pertinent parameters in the presence of different shapes of copper nanoparticles in this section. Fig. 3.2 and Fig. 3.3 display the volume fraction effects of copper nanoparticles with different shapes on velocity and temperature profiles. It is perceived that with an increase in volume fraction of platelets, cylinders and bricks nanoparticles, the velocity decreases. But for temperature profile one witness the opposite behavior. This figure directs to the result that θ increases with an increase in

volume-fraction of platelets, cylinders and bricks nanoparticles. The maximum decrease in velocity and maximum increase in temperature are caused by platelets, followed by cylinder and bricks respectively. Figs. 3.4 and 3.5 designate the magnetic parameter effects on velocity and the temperature fields. It is observed that the velocity is diminished and the temperature is upturn respectively for increasing the strength of magnetic parameter. The behaviors of porosity parameter in the presence of different shaped nanoparticles on velocity and temperature fields are observed in the Figs. 3.6 and 3.7. The behavior of porosity parameter Λ on velocity and temperature profiles is quite similar to that of magnetic parameter M_1 . The effects of radiation parameter on fields of velocity and temperature are publicized in Figs. 3.8 and 3.9. It is seen that velocity and temperature profiles increase when N is increased. It is reasonable in the sense that energy production causes to enhance the velocity and temperature fields. The effects of temperature power index on velocity and temperature profiles are displayed in Figs. 3.10 and 3.11. It is found that the flow speed as well as temperature is decline when increasing the power law index. The effect of entropy generation rate S_{gen} is discussed in Fig. 3.12. It is found that increase percentage in concentration of nanoparticles causes to increasing entropy generation rate. The increment in heat transfer irreversibility by reason of heat transfer (HTI) and fluid friction irreversibility (FFI) is responsible to increment in the total entropy generation. As it is noted in temperature profile that fluid has maximum temperature due to platelets nanoparticle, therefore as a result entropy generation rate is maximum by platelets shaped nanoparticle. Fig. 3.13 discloses the study of Bejan number. It is realized that HTI is dominant as compared to FFI near to cone surface. In Addition, platelets nanoparticles lead to the minutest heat loss whereas the maximum heat loss ensues by choosing bricks nanoparticles. Tables 3.2 to 3.6 are prepared to see the effects of various pertinent parameters on Skin-friction and Nusselt number. Table 3.2 exhibits the impact of particles volume fraction on Skin-friction and Nusselt number. For large value of nanoparticles fraction, an increase is found in the coefficient of Skin-friction as well as in Nusselt number. The Skin-friction coefficient and Nusselt number are maximum values for bricks, cylinders and platelets nanoparticles. Table 3.3 reflects the influence of magnetic parameter on Skin friction and Nusselt number. It is found that the maximum decrease in Skin-friction and Nusselt number for large value of magnetic parameter in case of

bricks when compared with the cases of cylinders and platelets. The impact of porosity parameter on Skin-friction and Nusselt number depicts in Table 3.4. The Skin-friction and Nusselt number coefficient reduce maximum for porosity parameter in the presence of bricks nanoparticles when compared with other nanoparticles. Table 3.5 exhibits the result of Skin-friction and Nusselt numbers collected by multiple variations of radiation parameter. It is perceived that the magnitude of Skin friction coefficient maximum escalates for large values of radiation parameter by platelets, however, it decreases for large values of radiation parameter by bricks nanoparticles. Table 3.6 demonstrates the power-law index parameter, it is obvious from this table that the Skin friction declines by bricks nanoparticles for large value of n whereas Nusselt numbers increase much by platelets nanoparticles for the same case.

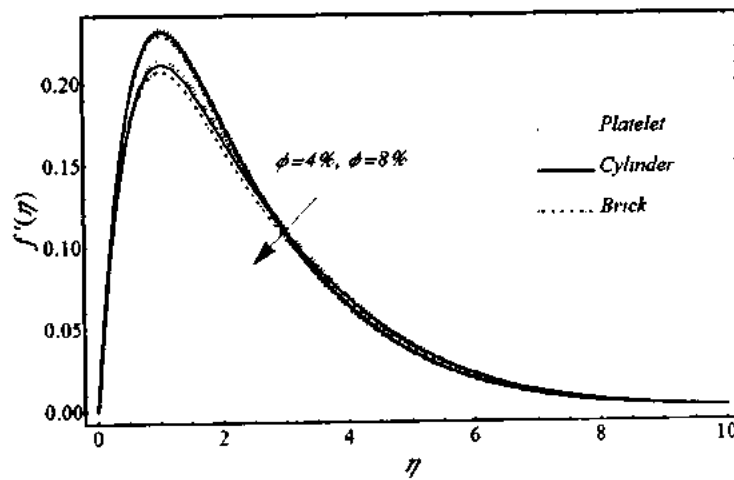


Fig. 3.2. Nanoparticle volume fraction effects on velocity profile when $\Lambda = 0.4$, $N = 0.4$, $M_1 = 0.4$ and $n = 1$.

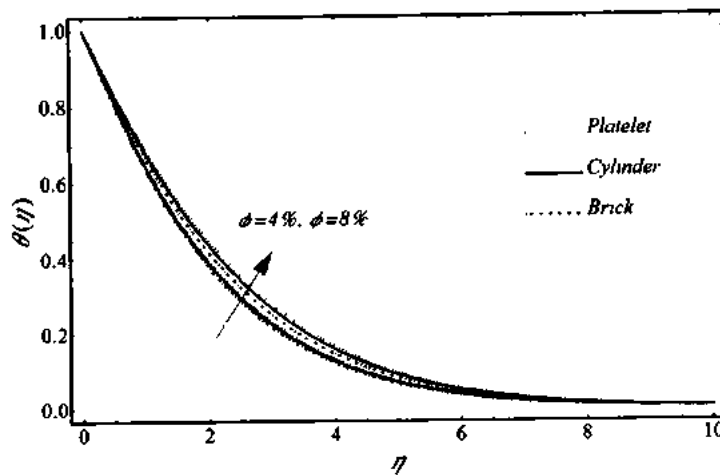


Fig. 3.3. Nanoparticle volume fraction effects on temperature profile when $\Lambda = 0.4$, $N = 0.4$, $M_1 = 0.4$ and $n = 1$.

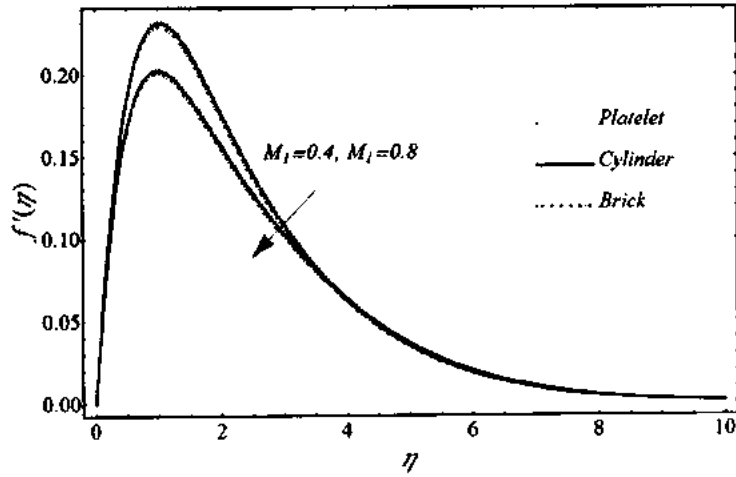


Fig. 3.4. Magnetic parameter effects on velocity profile $\Lambda = 0.4$, $N = 0.4$, $\phi = 4\%$ and $n = 1$.

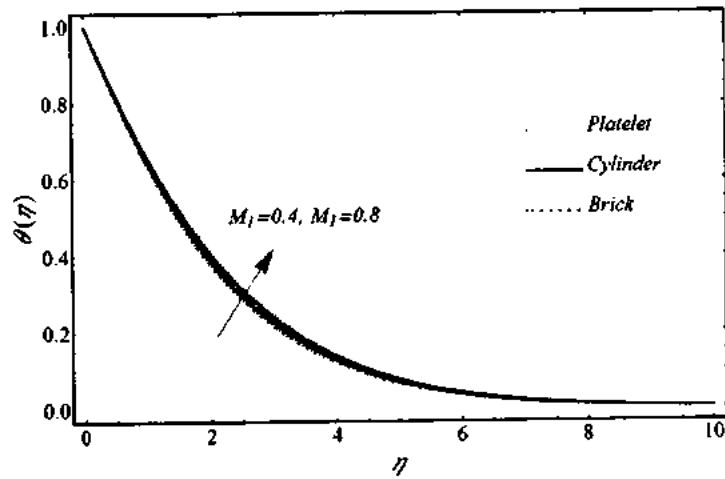


Fig. 3.5. Magnetic parameter effects on temperature profile $\Lambda = 0.4$, $N = 0.4$, $\phi = 4\%$ and $n = 1$.

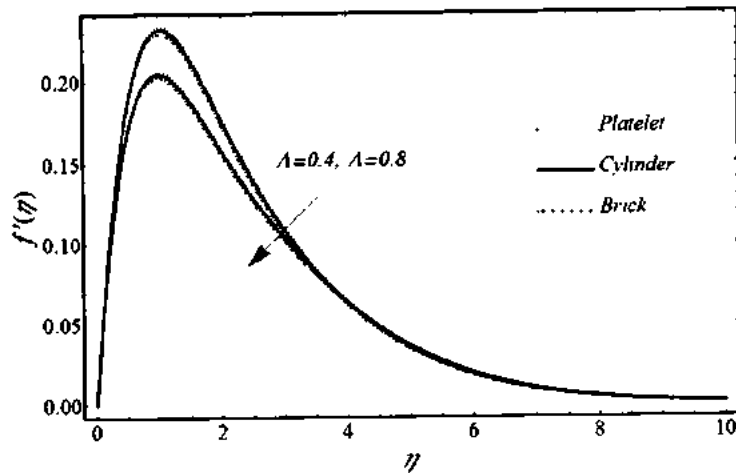


Fig. 3.6. Porosity parameter effects on velocity profile when $M_1 = 0.4$, $N = 0.4$, $\phi = 4\%$ and $n = 1$.

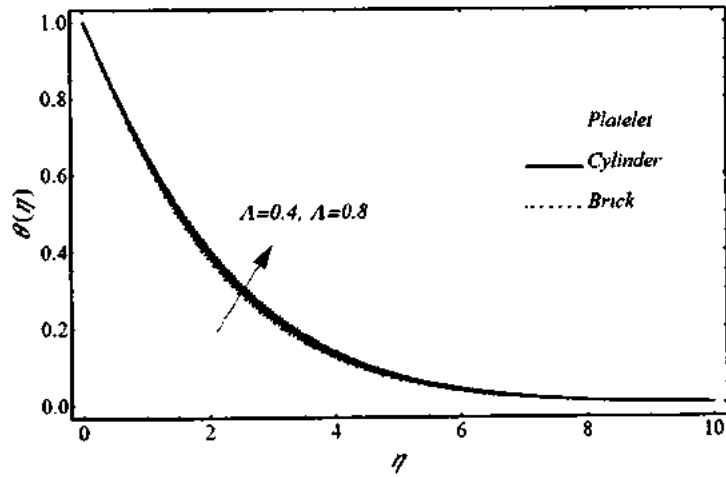


Fig. 3.7. Porosity parameter effects on temperature profile when $M_1 = 0.4$, $N = 0.4$, $\phi = 4\%$ and $n = 1$.

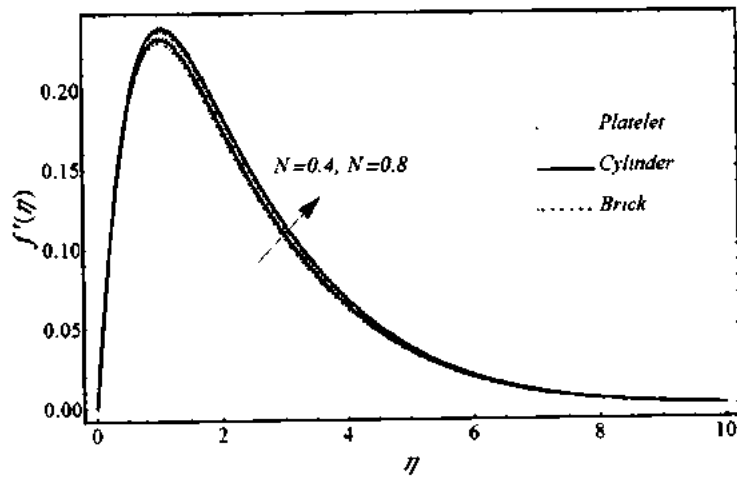


Fig. 3.8. Radiation parameter effects on velocity profile $M_1 = 0.4$, $\Lambda = 0.4$, $\phi = 4\%$ and $n = 1$.

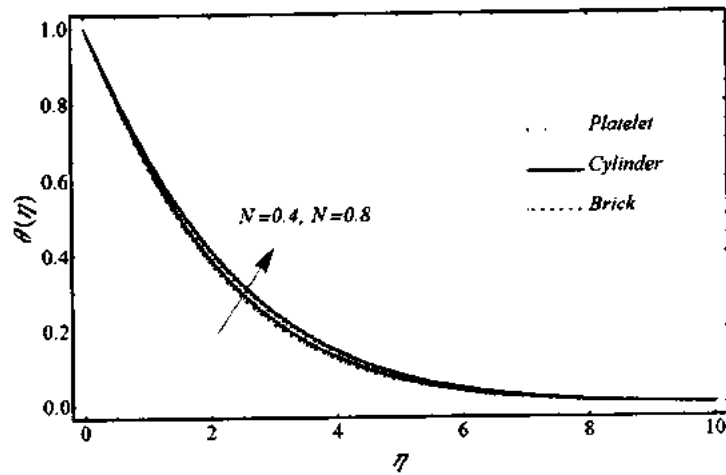


Fig. 3.9. Radiation parameter effects on temperature profile $M_1 = 0.4$, $\Lambda = 0.4$, $\phi = 4\%$ and $n = 1$.

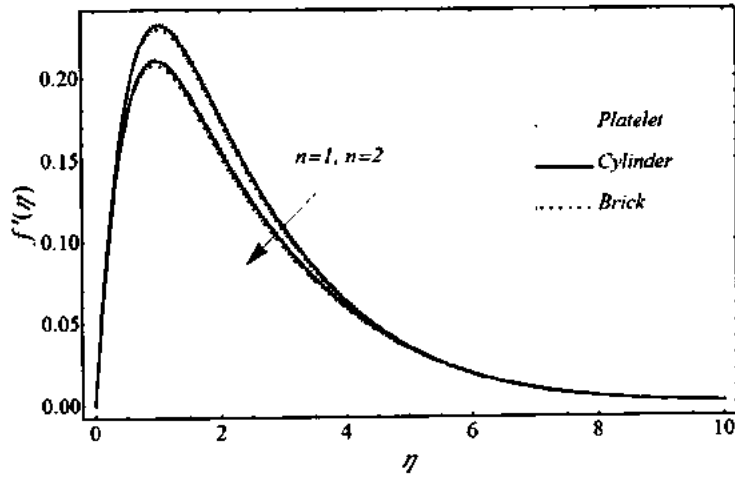


Fig. 3.10. Power law index effects on velocity profile when $M_1 = 0.4$, $\Lambda = 0.4$, $\phi = 4\%$ and $N = 0.4$.

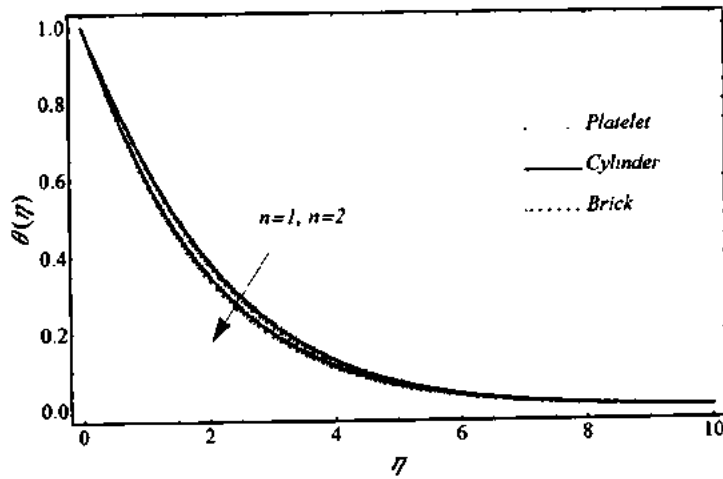


Fig. 3.11. Power law index effects on temperature profile when $M_1 = 0.4$, $\Lambda = 0.4$, $\phi = 4\%$ and $N = 0.4$.

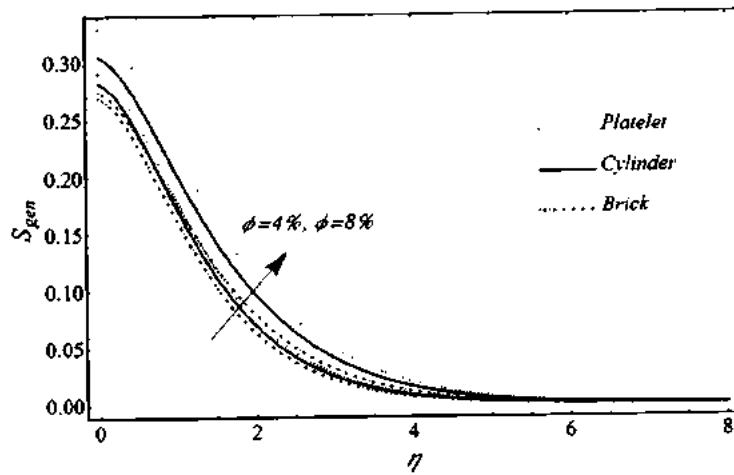


Fig. 3.12 Nanoparticle volume fraction effects on S_{gen} when $\Lambda = 0.4$, $M_1 = 0.4$, $N = 0.4$, $n = 1$, $T_w = 288$, $T_\infty = 308$, $x = 0.1$ and $Ra_x = 10$.

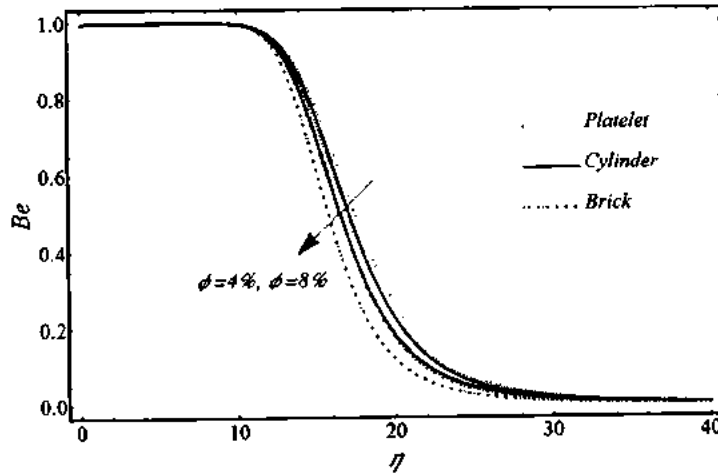


Fig. 3.13. Nanoparticle volume fraction effects on Be when $\Lambda = 0.4$, $M_1 = 0.4$, $N = 0.4$, $n = 1$, $T_w = 288$, $T_\infty = 308$, $x = 0.1$ and $Ra_x = 10$.

Table 3.2. Nanoparticle volume fraction effects on Skin friction and Nusselt number when $M_1 = 0.4$, $\Lambda = 0.4$, $N = 0.4$ and $n = 1$.

	ϕ	Platelets	Cylinder	Bricks
$Ra_x^{1/4} C_f$	0%	1.3422	1.3422	1.3422
	4%	1.3752	1.3716	1.3551
	8%	1.4089	1.4019	1.3908
$Ra_x^{-1/4} Nu$	0%	0.4477	0.4477	0.4477
	4%	0.4954	0.4861	0.4718
	8%	0.5435	0.5262	0.4994

Table 3.3. Magnetic parameter effects on Skin friction and Nusselt number when $\phi = 4\%$, $\Lambda = 0.4$, $N = 0.4$ and $n = 1$.

	M_1	Platelets	Cylinder	Bricks
$Ra_x^{1/4} C_f$	0	1.4234	1.3949	1.4128
	0.4	1.3752	1.3716	1.3551
	0.8	1.2570	1.2518	1.2501
$Ra_x^{-1/4} Nu$	0	0.5035	0.4933	0.4789
	0.4	0.4954	0.4861	0.4718

0.8 0.4731 0.4639 0.4505

Table 3.4. Porosity parameter effects on Skin friction and Nusselt number when $\phi = 4\%$, $M_1 = 0.4$, $N = 0.4$ and $n = 1$.

	Λ	Platelets	Cylinder	Bricks
$Ra_x^{1/4} C_f$	0	1.5111	1.5144	1.4646
	0.4	1.3752	1.3716	1.3551
	0.8	1.2664	1.2622	1.2550
$Ra_x^{-1/4} Nu$	0	0.5179	0.5139	0.5053
	0.4	0.4954	0.4861	0.4716
	0.8	0.4747	0.4661	0.4524

Table 3.5. Radiation parameter effect on Skin friction and Nusselt number when $\phi = 4\%$, $M_1 = 0.4$, $\Lambda = 0.4$ and $n = 1$.

	N	Platelets	Cylinder	Bricks
$Ra_x^{1/4} C_f$	0	1.3119	1.3187	1.3004
	0.4	1.3752	1.3716	1.3551
	0.8	1.4043	1.4036	1.4020
$Ra_x^{-1/4} Nu$	0	0.5517	0.5426	0.5287
	0.4	0.4954	0.4861	0.4718
	0.8	0.4549	0.4457	0.4316

Table 3.6. Power law index effects on Skin friction and Nusselt number when $\phi = 4\%$, $M_1 = 0.4$, $\Lambda = 0.4$ and $N = 0.4$.

	n	Platelets	Cylinder	Bricks
$Ra_x^{1/4} C_f$	0	1.5178	1.5024	1.4906
	1	1.3752	1.3716	1.3551
	2	1.2748	1.2714	1.2663
$Ra_x^{-1/4} Nu$	0	0.3824	0.3736	0.3644
	1	0.4954	0.4861	0.4718

3.4 Conclusions

In this chapter, the natural convection boundary layer flow having nano-size particles on entropy generation with based fluid along an inverted cone is investigated. Porous medium, magnetohydrodynamic, radiation and power law index effects are also taken into account. It is noticed that the velocity of fluid declines by cumulating the values of particle volume fraction, magnetic, porosity and power law index parameters. It is also seen that due to increase in radiation parameter, the velocity of nanofluid is increased. On the other hand, temperature increases by increasing the particle volume fraction, magnetic parameter, porosity parameter and radiation parameter. The reverse behavior is detected for power law index parameter. In fact, it is in accordance with the physical expectation since it is well known that the platelets nanoparticle has greater sphericity than cylinder and bricks nanoparticles, therefore, the platelets nanoparticle comparatively gains maximum temperature than others. The velocity decreases maximum by bricks nanoparticles when compared with other shapes. With the increase of particle fraction, magnetic, porosity, radiation parameters, temperature is increased. The Skin-friction and Nusselt number reduce with the increase of magnetic and porosity parameters while the Skin-friction rises by increasing the values of particle fraction and viscous dissipation. The Nusselt number also rises by raising the values of particle fraction and power law index.

Chapter 4

Study of natural convection MHD nanofluid by means of single and multi-walled carbon nanotubes suspended in a salt-water solution

The natural convective flow of nanofluid along a cone with variable wall temperature under the presence of magnetohydrodynamic is investigated in this chapter. The mathematical model based on nanolayer single and multi-wall carbon nanotubes in salt-water solutions and interfacial layers is considered. The nonlinear partial differential equations are analytically solved via BVP4c 2.0 package. Flow behavior under altering involving physical parameters such as: nanoparticle volume fraction, nanolayer, Prandtl number, Eckert number and power law index on the velocity and the temperature profiles is discussed and explained through graphs and tables. In addition, shear stress and heat transfer rate at wall are calculated and examined.

4.1 Mathematical formulation of the problem

Consider the brain solution base nanofluid flow that containing SWCNT and MWCNT over a cone. The description for geometry for problem is publicized in Fig. 2.1. Under the boundary layer approximations, the governing equations take the form

$$\frac{\partial}{\partial x}(ru) + \frac{\partial}{\partial y}(rv) = 0, \quad (4.1)$$

$$\rho_{nf} \left(u \frac{\partial u}{\partial x} + v \frac{\partial u}{\partial y} \right) = \mu_{nf} \frac{\partial^2 u}{\partial y^2} + (\rho\beta)_{nf} g(T - T_\infty) \cos\Omega - \sigma_0 \beta_0^2 u, \quad (4.2)$$

$$u \frac{\partial T}{\partial x} + v \frac{\partial T}{\partial y} = \alpha_{nf} \frac{\partial^2 T}{\partial y^2} + \frac{\sigma \beta_0^2}{(\rho C_p)_{nf}} u^2. \quad (4.3)$$

The hydrodynamic boundary conditions are

$$\left. \begin{aligned} u(x, 0) = 0, \quad v(x, 0) = 0, \quad u(x, \infty) = 0, \\ T(x, 0) = T_w = T_\infty + Cx^n, \quad T(x, \infty) = T_\infty \end{aligned} \right\} \quad (4.4)$$

In above, the physical properties for nanofluid are defined in Eqs. (1.3), (1.7), (1.8) and (1.12) respectively. To account the ordered layering of liquid molecules at carbon tubes taken thermal conductivity model which is defined in Eq. (1.18). In thermal conductivity model, $j(=a, b, c)$ is along the semi-axis direction of the carbon tube as shown in Fig. 4.1.

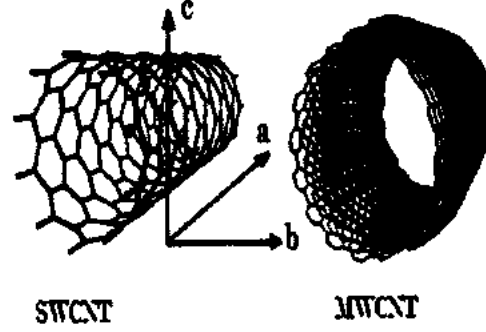


Fig. 4.1. Geometry for SWCNT and MWCNT.

By using the transformations Eq. (2.7) into Eqs. (4.1) to (4.4), the non-dimensional form of resulting equations along with the corresponding boundary conditions are obtained as

$$\frac{\rho_{nf}}{\rho_f} \left[\left(\frac{n+1}{2} \right) f'^2 - \left(\frac{n+7}{4} \right) f f'' \right] = \frac{\mu_{nf}}{\mu_f} f''' - M_1 f' + \frac{(\rho\beta)_{nf}}{(\rho\beta)_f} \theta, \quad (4.5)$$

$$\text{Pr} \frac{(\rho C_p)_{nf}}{(\rho C_p)_f} \left[n\theta f' - \left(\frac{n+7}{4} \right) f \theta' \right] = \frac{k_{nf}}{k_f} \theta'' + \text{Pr} Ec M_1 f'^2, \quad (4.6)$$

along the boundary conditions

$$\left. \begin{aligned} f=0, \quad f'=0, \quad \theta=1 \quad \text{when } \eta=0 \\ f'=0, \quad \theta=0 \quad \text{when } \eta \rightarrow \infty \end{aligned} \right\}. \quad (4.7)$$

where $Ec = \frac{\nu_f^2 Ra_x}{x^2 (C_p)_f (T_w - T_\infty)}$ is the Eckert number.

The Skin-friction coefficient and local Nusselt number are given by

$$C_f Ra_x^{1/4} = 2 \left(\frac{\mu_{nf}}{\mu_f} \right) f''(0) \quad \text{and} \quad Nu_x Ra_x^{-1/4} = - \left(\frac{k_{nf}}{k_f} \right) \theta'(0). \quad (4.8)$$

4.2 Solution of the problem

In this section, we will provide the analytic and uniformly valid solutions by using BVPh 2 Package. The BVPh 2.0 requirements to put the governing equations along

with corresponding boundary conditions, initial guess and auxiliary linear operators. Thus taken the auxiliary linear operators corresponding to the Eqs. (4.7) and (4.8) as

$$\mathcal{L}_1(f) = \frac{d}{d\eta} \left(\frac{d^2 f}{d\eta^2} - f \right), \quad \mathcal{L}_2(\theta) = \left(\frac{d^2}{d\eta^2} - 1 \right) \theta. \quad (4.9)$$

Considering the boundary conditions in Eq. (4.7), we respectively choose the following initial approximation for variable wall temperature

$$f_0(\eta) = 1 + f_w - e^{-\eta}, \quad \theta_0(\eta) = e^{-\eta}. \quad (4.10)$$

Using the linear auxiliary operators in Eq. (4.9) and the initial approximations in Eq. (4.10), the coupled nonlinear Eqs. (4.5) and (4.6) subject to the Eq. (4.7) can be solved directly by Using package BVP4c 2.0. Finally the solutions of velocity and temperature distributions can be exposed explicitly by means of an infinite series of the following form

$$f_i(\eta) = \sum_{m=0}^{\infty} f_{i,m}(\eta), \quad \theta_i(\eta) = \sum_{m=0}^{\infty} \theta_{i,m}(\eta), \quad (4.11)$$

where $f_{i,m}(\eta)$ and $\theta_{i,m}(\eta)$ are governed by high-order deformation equations. The results for the velocity, the temperature distribution, Sink fiction and Nusselt numbers for different non-dimensional numbers at 30th iterations of package are obtained as

$$\begin{aligned} f = & \left(-1 + \frac{13C_1}{200} + \frac{C_2}{15} - \frac{2C_3}{15} + \frac{M_1}{12} + \frac{3C_4 n}{200} \right) e^{-\eta} + \left(\frac{7C_1}{60} + \frac{C_2}{15} + \frac{C_3}{15} - \frac{M}{15} - \frac{C_1 n}{60} - \frac{C_2 \alpha}{15} \right) e^{-2\eta} \\ & + \left(\frac{13C_1}{120} - \frac{C_2}{15} + \frac{M_1}{60} + \frac{C_1 n}{120} \right) e^{-3\eta} + \left(-\frac{31C_1}{600} - \frac{C_1 n}{600} \right) e^{-4\eta} + \frac{1}{100} C_1 e^{-5\eta} \\ & + \frac{1}{2} - \frac{3C_1}{200} - \frac{C_2}{15} + \frac{C_3}{15} - \frac{M_1}{30} - \frac{C_1 n}{200}, \end{aligned} \quad (4.12)$$

$$\begin{aligned} \theta = & \left(1 + \frac{37C_5}{150} - \frac{777C_4 Pr}{8000} + \frac{37EcM_1 Pr}{1500} - \frac{1369C_4 n Pr}{24000} \right) e^{-\eta} + \left(-\frac{37C_5}{150} + \frac{259C_4 Pr}{1200} + \frac{37C_4 n Pr}{1200} \right) e^{-2\eta} + \\ & \left(-\frac{259C_4 Pr}{1600} - \frac{37EcM_1 Pr}{400} + \frac{111C_4 n Pr}{1600} \right) e^{-3\eta} + \left(\frac{C_4 Pr}{6000} + \frac{37EcM_1 Pr}{375} - \frac{C_4 n Pr}{6000} \right) e^{-4\eta} \\ & - \frac{37e^{-5\eta} EcM_1 Pr}{1200}. \end{aligned} \quad (4.13)$$

4.3 Results and discussion

In this segment, the influences of emerging parameters involved in expression of the velocity and the temperature distributions are examined through Figs. 4.2 to 4.13 with salt water solutions based nanofluid containing SWCNTs and MWCNTs. The resulting equations include the Prandtl number, Eckert number, magnetic, nanoparticles volume fraction and power law index parameters. The radius 0.5nm and length 100nm of single wall and multi-wall carbon nanotube are taken into account. The thickness of nanolayer around tubes is 2nm whereas the thermal conductivity of layer is considered $2k_f$. In view of Eq. (1.18) the carbon nanotubes suspensions in 15% mixture of salt in water are used. The value of the parameter t_1 is chosen to be 6nm which corresponds to 2nm layer thickness $\left(\sqrt{(0.5)^2 + 6} - 0.5 = 2 \text{ nm}\right)$ along b -axis and c -axis provided that $a = 100 \text{ nm}$, $b = c = 0.5 \text{ nm}$. Also a negligible layer thickness $\left(\sqrt{100^2 + 6} - 100 = 002 \text{ nm}\right)$ along a -axis is considered. Figs. 4.2 and 4.3 illustrate the volume fraction effect on the velocity and the temperature of the fluid. In Fig. 4.2, the velocity of fluid is decreased when volume fraction is increased. It is observed that in the presence of the nanoparticles the movement of the fluid tends to slow down. In Fig. 4.3, temperature of fluid increases by rising particle volume fraction. This is consistent with the fact that the thermal conductivity of nanofluid is boosted by increasing the particle volume fraction. It is also observed that the maximum velocity and the minimum temperature are gained by SWCNTs and MWCNTs respectively within fraction $0\% \leq \phi \leq 10\%$. Figs. 4.4 and 4.5 show the impact of magnetic field on velocity and temperature fields. It is examined through these plots that the velocity and the temperature of fluid are respectively declined and enhanced when magnetic effect is raised. Due to the magnetic field, the particles are aggregated in the direction of field that resist flow and enhanced the temperature of fluid. In addition, the minimum velocity and the maximum temperature are observed by MWCNTs and SWCNTs respectively. The Eckert number effect on the velocity and the temperature have been seen in Figs. 4.6 and 4.7. Fig. 4.6 demonstrates the enhancement in the velocity distribution in flow region by increasing the Eckert number. This is by reason of frictional heating that leads to storage of energy in the

liquid. Fig. 4.7 shows the influence of Eckert number on temperature profile. It is perceived that the temperature cumulates by cumulating the values of Eckert number. Figs. 4.8 and 4.9 show the behavior of the velocity and the temperature for diverse values of the Prandtl number Pr . Fig. 4.8 points out that the velocity profile is declined due to rising value of Prandtl number. In Fig. 4.9, the temperature profile is increased for small value ($Pr = 0.71$) compared to large value ($Pr = 7$). The reason is that thermal diffusivity is dominated for smaller values of Pr , therefore, fluid temperature rapidly increases at small value of Pr . The stimulus on the velocity and the temperature profiles of power law index are sketched in Figs. 4.10 and 4.11. It is noticed that the effect of increasing value of n is to decrease the velocity as well as the temperature profiles. Figs. 4.12 and 4.13 are plotted to see the effects of CNTs dimension on velocity and temperature of fluid. It is detected that the velocity field increases when CNTs have small length, but when length of CNTs exceeds form certain length, velocity decreases. In Fig. 4.13 it is noticed that when length of CNTs is increased, the temperature of CNTs is decreased. When length of CNTs is exceed form certain limit the CNTs have no effects on the temperature of fluid.

In the tables 4.1 to 4.5, the numeric results illustrate the impressions of various parameters on the shear stress and the heat transfer rate at wall with the presence of SWCNTs and MWCNTs in salt water solutions. The effect of particle volume fraction on the local Skin friction coefficients and the local Nusselt number are shown in table 4.1. Table 4.1 depicts that with the increase in volume fraction of the SWCNT's and MWCNTs in the base fluid, local Skin friction coefficient increases. It is also observed that heat Skin friction increases maximum by SWCNTs than MWCNTs within $0 \leq \phi \leq 10\%$ volume fraction. In addition, the transfer rate is increased by increasing volume fraction of tubes as shown in table 4.1. It is also realized that the heat transfer rate has maximum increase with small difference by SWCNTs than MWCNTs at different volume fraction. Table 4.2 illustrates the influence of the Rayleigh number on local Skin friction coefficients and Nusselt number. The results reflect to dwindle in Skin friction and amplify in the heat transfer rate when Rayleigh number is enhanced. The effects of carbon tube's size on shear stress and heat transfer rate at wall are shown in table 4.3. Here, all the calculations have been done by taking nanolayer thickness about 2nm. For keeping the fixed nanolayer thickness, we choose different value of t_1 for different dimensions of tubes.

Table 4.3 depicts that shear stress at wall as well as heat transfer rate both decrease with the escalation in the length and radius of SWCNTs and MWCNTs respectively. The reason of decreasing in Nusselt number is the reduction of thermal conductivity due to increasing the dimension of tubes. In this table, it also analyzed that the maximum enhancement in length and diameter of tube is not effective for the heat transfer rate. Table 4.4 exhibits the result of Skin-friction coefficient and Nusselt number collected by variations of thermal conductivity of nanolayer k_{layer} . Here one can see that when thermal conductivity of nanolayer is increased, Skin friction and Nusselt number are increased simultaneously. Table 4.5 depicts the impact of salt composition in water on coefficients of Skin-friction and heat transfer rate. The enhancement has happened in both heat and stress at wall when quantity of salt is increased in water with the composition of 0 to 25%.

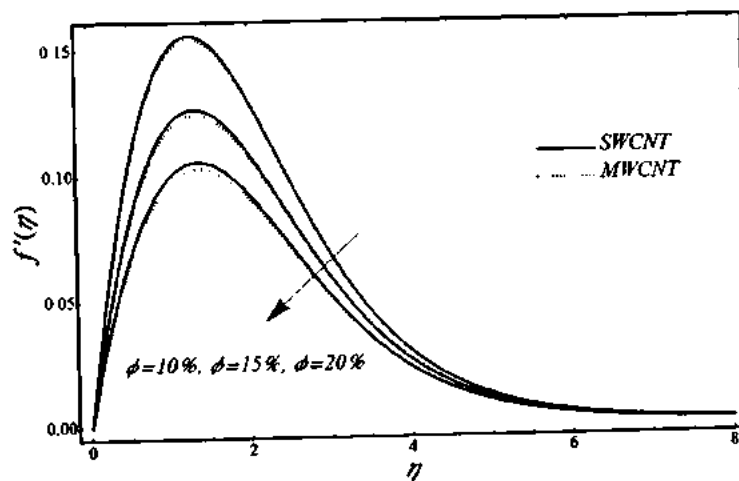


Fig. 4.2. Particles volume fraction effects on velocity field.

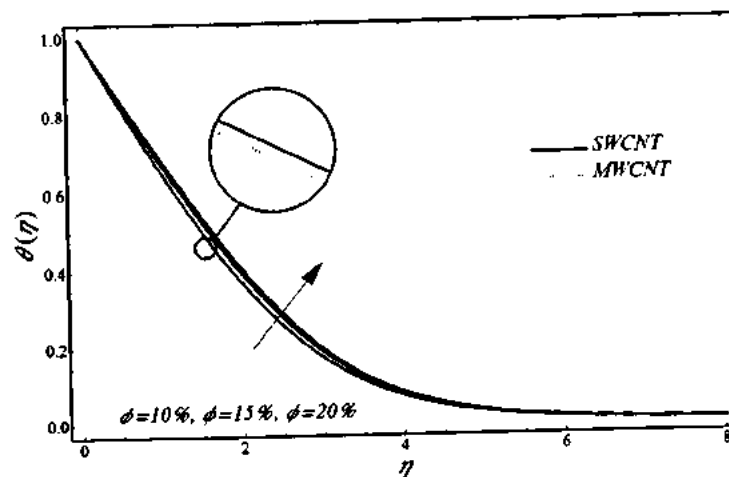


Fig. 4.3 Particles volume fraction effects on temperature field.

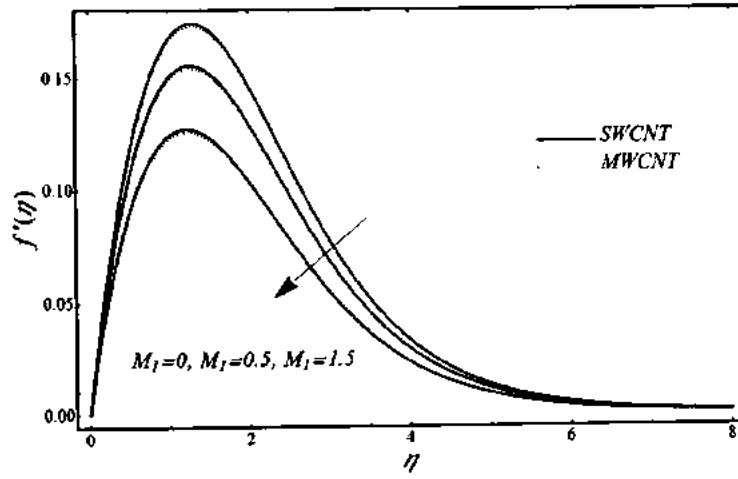


Fig. 4.4. Magnetic parameter effect on velocity field.

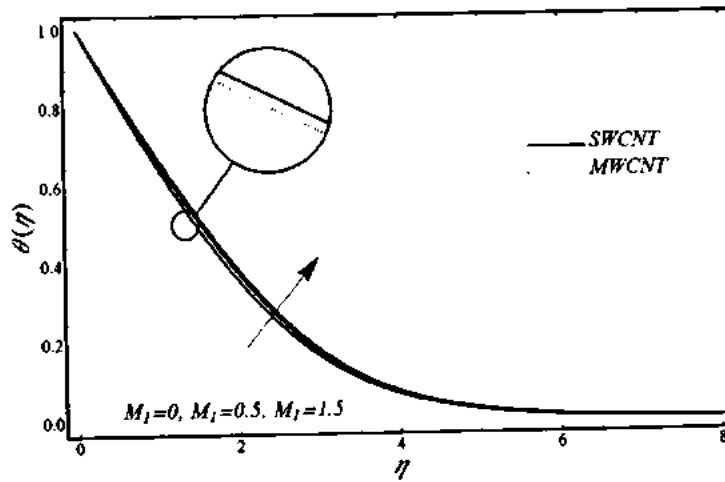


Fig. 4.5. Magnetic parameter effects on temperature field.

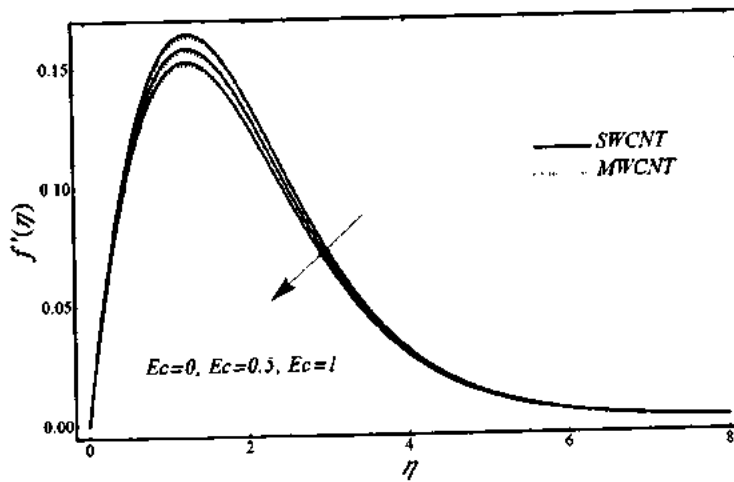


Fig. 4.6. Eckert number effects on velocity field.

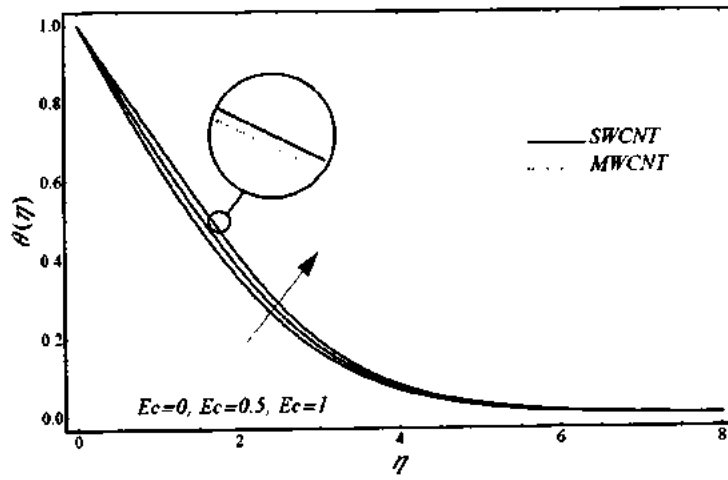


Fig. 4.7. Eckert number effects on temperature field.

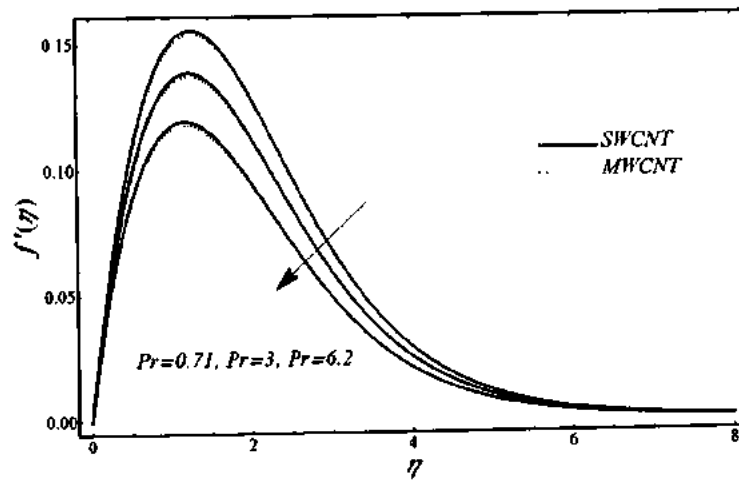


Fig. 4.8. Prandtl number effects on velocity field.

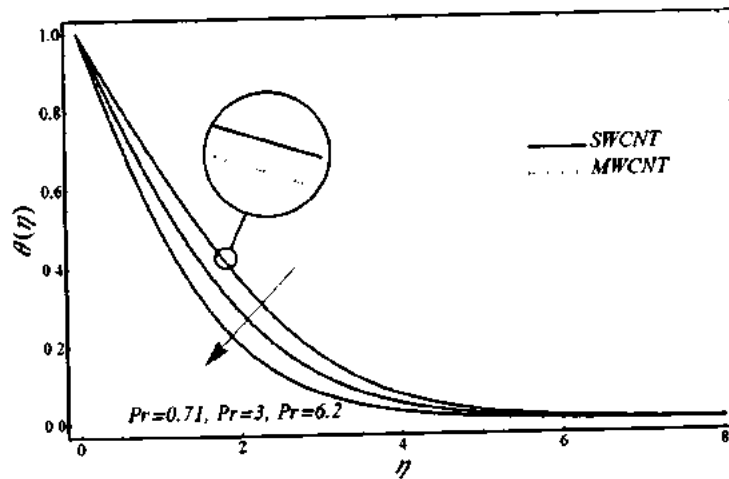


Fig. 4.9. Prandtl number effects on temperature field.

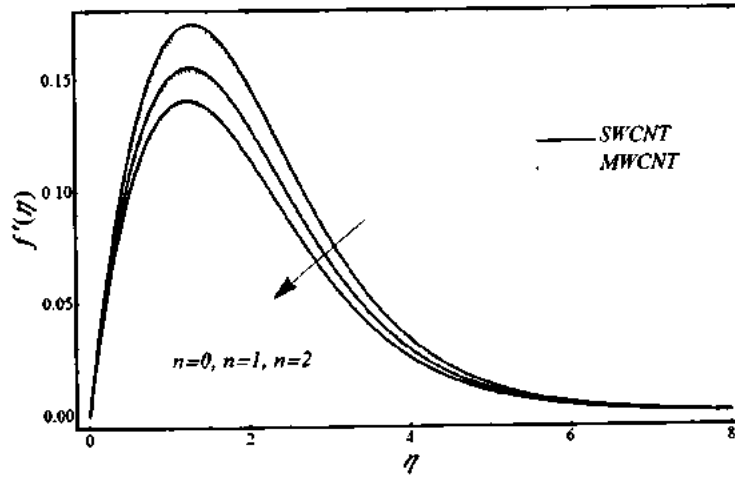


Fig. 4.10. Power law index effects on velocity profile.

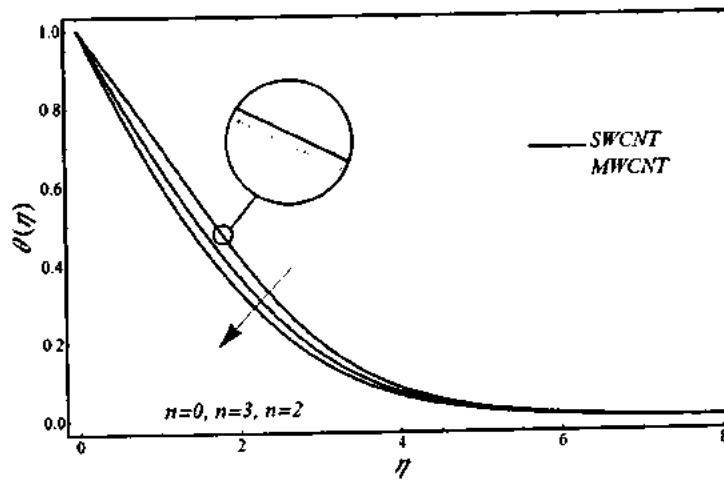


Fig. 4.11. Power law index effects on temperature profile.

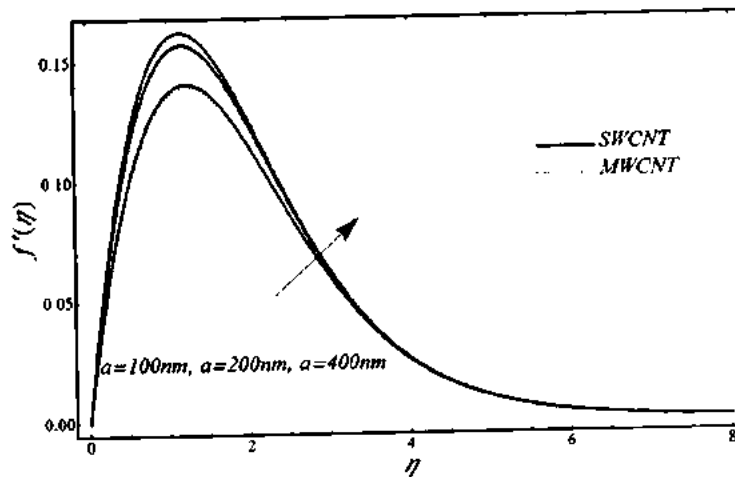


Fig. 4.12. CNTs dimensions effects on velocity profile.

Table 4.3. CNTs dimensions effects on Skin-friction coefficient and Nusselt number.

	<i>Dimension</i>	<i>SWCNT</i>	<i>MWCNT</i>
C_f	$a = 100, b = c = .5$	0.91037	0.90527
	$a = 150, b = c = 1$	0.86283	0.85890
	$a = 300, b = c = 1.5$	0.8645	0.84275
Nu	$a = 100, b = c = .5$	0.99830	0.99228
	$a = 150, b = c = 1$	0.98389	0.98353
	$a = 300, b = c = 1.5$	0.97588	0.97614

Table 4.4. Nanolayer thermal conductivity effects on Skin-friction coefficient and Nusselt number.

	k_f	<i>SWCNT</i>	<i>MWCNT</i>
C_f	<i>1nm</i>	0.89938	0.89422
	<i>2nm</i>	0.91037	0.90527
	<i>3nm</i>	0.91953	0.91447
Nu	<i>1nm</i>	0.91376	0.90822
	<i>2nm</i>	0.99830	0.99228
	<i>3nm</i>	1.08235	1.07578

Table 4.5. Salt Composition effects on Skin-friction coefficient and Nusselt number.

	Salt Composition	<i>SWCNT</i>	<i>MWCNT</i>
C_f	0%	0.90946	0.90456
	15%	0.91037	0.90527
	25%	0.91351	0.90720
Nu	0%	0.99556	0.98949
	15%	0.99830	0.99228
	25%	0.99999	0.99424

4.4 Conclusions

In this chapter, the nanolayer effects on SWCNTs and MWCNTs in salt-water solution based nanofluid with natural convection are analyzed. The magnetohydrodynamic is also taken into account. The resulting boundary value problem governed by nonlinear coupled equations is solved analytically. The influences of the physical parameters on velocity and temperature profiles are studied. One can see that the velocity of nanofluid decreases by increasing the volume fraction of nanotubes, magnetic parameters and the wall temperature power index parameter. On the other hand, the temperature of nanofluid increases by increasing the volume fraction of nanotubes, magnetic parameters, Prandtl and Eckert numbers. The velocity increases by increasing Eckert number whereas the temperature profile decreases with the increase of wall temperature, power index parameter and Prandtl number. The Skin friction is increased by increasing volume fraction, thermal conductivity of the nanolayer and salt composition in water. The heat transfer rate is increased by increasing the volume fraction, Rayleigh number, thermal conductivity of nanolayer and the salt composition in water. It is worth mentioning that all of these deepen observations about the considered boundary-layer flow illustrate the general validity of BVPh 2.0 package for complex boundary layer flows.

Chapter 5

On the modeling of natural convection flow of non-Newtonian nanofluid past a vertical cone

In this chapter, investigate the effects of natural convection flow over a cone. The viscoelastic Polydimethylsiloxane (PDMS) non-Newtonian nanofluid as a base fluid is considered. The nanoparticles of different materials are taken into account. The main emphasis is to find the analytical and numerical solutions to discuss the diverse issues befall for the said model. Effects of energetic parameters like volume concentration, different particles radii on thermal conductivity, wall shear stress, heat transfer characteristics, velocity and temperature profile have been inspected by graphically and tablets forms. It is observed that the nanoparticles have significantly impact on base fluid's thermal conductivity. The temperature profile and rate of heat transfer are increasing function of nanoparticles. There is also found that particles of small sizes contained nanofluids have effective rate of heat transfer as compared to large sizes particles contained nanofluids. Comparison with the existing studies is made as a limiting case of the considered problem. An excellent agreement with the existing results in is noted.

5.1 Mathematical formulation of the problem

The steady-state boundary layer natural convection flow of second grade viscoelastic nanofluid over a cone is assumed. The mathematical depiction of problem geometry is show in Fig. 2.1. The study takes into consideration a Polydimethylsiloxane as viscoelastic base fluid and nanoparticles of different material for nanofluid. This type of base fluid has lots of applications in mechanics and industrial manufacturing. To investigate the heat and mass flow behavior of this, take the governing equations under the Boussinesq approximation as follow

$$\frac{\partial}{\partial x}(ru) + \frac{\partial}{\partial y}(rv) = 0, \quad (5.1)$$

$$\rho_{nf} \left(u \frac{\partial u}{\partial x} + v \frac{\partial u}{\partial y} \right) = \mu_{nf} \frac{\partial^2 u}{\partial y^2} \quad (5.2)$$

$$-\alpha_1 \left\{ u \frac{\partial^3 u}{\partial x \partial y^2} + v \frac{\partial^3 u}{\partial y^3} + \frac{\partial u}{\partial x} \frac{\partial^2 u}{\partial y^2} - \frac{\partial^2 u}{\partial x \partial y} \frac{\partial u}{\partial y} \right\} + (\rho\beta)_{nf} g (T - T_\infty) \cos \Omega, \quad (5.3)$$

$$(\rho C_p)_{nf} \left(u \frac{\partial T}{\partial x} + v \frac{\partial T}{\partial y} \right) = k_{nf} \frac{\partial^2 T}{\partial y^2}.$$

Subject to boundary conditions are

$$u = v = 0, \quad T = T_w(x) = T_\infty + A \left(\frac{x}{L} \right) \quad \text{at } y = 0, \quad (5.4)$$

$$\frac{\partial u}{\partial y} = 0, \quad u = 0, \quad T = T_\infty \quad \text{at } y \rightarrow \infty.$$

The physical properties for nanofluid are given in Eqs. (1.3), (1.7), (1.8), (1.14) and (1.23) respectively.

Let us introduce the following non-dimensional variables

$$X = \frac{x}{L}, \quad Y = \frac{y}{L}, \quad R = \frac{r}{L}, \quad U = \frac{u}{U_o}, \quad (5.5)$$

$$V = \frac{Gr^{1/4} v}{U_o}, \quad \bar{T} = \frac{T - T_\infty}{T_w - T_\infty}, \quad Gr = \left(\frac{U_o L}{\nu_f} \right)^2,$$

where $U_o = [g\beta_f \cos(\Omega)L(T_w - T_\infty)]^{1/2}$.

Substituting Eq. (5.5) in (5.1) to (5.4) and get the dimensionless forms of governing equations as follow

$$\frac{\partial}{\partial X} (RU) + \frac{\partial}{\partial Y} (RV) = 0, \quad (5.6)$$

$$\frac{\rho_{nf}}{\rho_f} \left(U \frac{\partial U}{\partial X} + V \frac{\partial U}{\partial Y} \right) = \frac{\mu_{nf}}{\mu_f} \frac{\partial^2 U}{\partial Y^2} - \varepsilon \cdot \left\{ U \frac{\partial^3 U}{\partial X \partial Y^2} + V \frac{\partial^3 U}{\partial Y^3} + \frac{\partial U}{\partial X} \frac{\partial^2 U}{\partial Y^2} - \frac{\partial^2 U}{\partial X \partial Y} \frac{\partial U}{\partial Y} \right\} + \frac{(\rho\beta)_{nf}}{(\rho\beta)_f} \bar{T}, \quad (5.7)$$

$$\frac{(\rho C_p)_{nf}}{(\rho C_p)_f} Pr \left(U \frac{\partial \bar{T}}{\partial X} + V \frac{\partial \bar{T}}{\partial Y} \right) = \frac{k_{nf}}{k_f} \frac{\partial^2 \bar{T}}{\partial Y^2}, \quad (5.8)$$

subject to boundary conditions

$$\left. \begin{aligned} U(X,0) = 0, \quad V(X,0) = 0, \quad \bar{T}(X,0) = X, \\ \frac{\partial U}{\partial Y}(X,\infty) = 0, \quad U(X,\infty) = 0, \quad \bar{T}(X,\infty) = 0, \end{aligned} \right\} \quad (5.9)$$

The following dimensionless quantities are obtained as

$$R = X \sin(\Omega), \quad \varepsilon' = \frac{U_o \alpha_1}{\nu_f L}. \quad (5.10)$$

Further, using the stream function formulation $\psi = XRf(Y)$ and $\bar{T} = X\theta(Y)$ along with the following transformation

$$U = \frac{1}{R} \frac{\partial \psi}{\partial Y}, \quad V = -\frac{1}{R} \frac{\partial \psi}{\partial X}. \quad (5.11)$$

The resulting Eqs. (5.6) to (5.9) become

$$\frac{\rho_{nf}}{\rho_f} [f'^2 - 2ff''] = \frac{\mu_{nf}}{\mu_f} f''' - \varepsilon' [2f'f''' - ff^{(4)} - f''^2] + \frac{(\rho\beta)_{nf}}{(\rho\beta)_f} \theta, \quad (5.12)$$

$$\text{Pr} \frac{(\rho C_p)_{nf}}{(\rho C_p)_f} [\theta f' - 2f\theta'] = \frac{k_{nf}}{k_f} \theta'', \quad (5.13)$$

$$\begin{aligned} f(0) = 0, \quad f'(0) = 0, \quad \theta(0) = 1, \\ f'(\infty) = 0, \quad f''(\infty) = 0, \quad \theta(\infty) = 0. \end{aligned} \quad (5.14)$$

The physical parameters of importance are Skin friction coefficient and local Nusselt number. The Skin friction coefficient is introduced as

$$C_f = \frac{2\tau_w}{\rho u_w^2}. \quad (5.15)$$

Here

$$\tau_w = \mu_{nf} \left[\frac{\partial u}{\partial y} \right]_{y=0} + \alpha_1 \left[u \frac{\partial^2 u}{\partial x \partial y} + v \frac{\partial^2 u}{\partial y^2} + 2 \frac{\partial u}{\partial x} \frac{\partial u}{\partial y} \right]_{y=0}. \quad (5.16)$$

The dimensionless form of Skin friction is achieved as

$$Gr^{1/4} C_f = 2X \left(\frac{\mu_{nf}}{\mu_f} \right) f''(0). \quad (5.17)$$

The local Nusselt number is obtained as

$$Nu = \frac{Lq_w}{k_f (T_w - T_\infty)}, \quad (5.18)$$

where

$$q_w = -k_{nf} \left(\frac{\partial T}{\partial y} \right)_{y=0}. \quad (5.19)$$

The dimensionless form of Nusselt number is given by

$$Gr^{-1/4} Nu = -\frac{k_{nf}}{k_f} \theta'(0). \quad (5.20)$$

5.2 Solution of the problem

Due to nonlinear nature of Eqs. (5.12) and (5.13), an exact solution is not possible, therefore, we opted to go for analytic solution. In this regard, the based BVPh 2.0 package is employed for solving nonlinear ordinary differential equation. In the package, a great freedom is to choose the initial guess and auxiliary linear operators, thus we choose desire the initial guess and auxiliary linear operators as follow

$$\mathcal{L}_1(f) = \frac{d}{d\eta} \left(\frac{d^2}{d\eta^2} - 1 \right) f, \quad \mathcal{L}_2(\theta) = \left(\frac{d^2}{d\eta^2} - 1 \right) \theta, \quad (5.21)$$

$$f_0(\eta) = 1 - (1 + \eta)e^{-\eta}, \quad \theta_0(\eta) = e^{-\eta}. \quad (5.22)$$

So far, we have defined all the input properly for this problem, except the convergence control parameters. Usually, the convergence-control parameters values are obtained by minimizing the squared residual error

$$E_f = \int_0^\infty \left[\begin{array}{l} -\frac{\rho_{nf}}{\rho_f} [f'^2 - 2ff''] + \frac{\mu_{nf}}{\mu_f} f''' \\ -\varepsilon^* [2f'f''' - ff^{(4)} - f'^2] + \frac{(\rho\beta)_{nf}}{(\rho\beta)_f} \theta \end{array} \right]^2 d\eta, \quad (5.23)$$

$$E_\theta = \int_0^\infty \left[\text{Pr} \frac{(\rho C_p)_{nf}}{(\rho C_p)_f} [\theta f' - 2f\theta'] - \frac{k_{nf}}{k_f} \theta'' \right]^2 d\eta. \quad (5.24)$$

The results for velocity and temperature at second iterations of package are obtained as

$$f(\eta) = 1 + (C_{30} + C_{31}e^{-2\eta} + C_{32}e^{-2z} + C_{33}e^{-3z} + C_{34}e^{-4z})e^{-z}, \quad (5.25)$$

$$\theta(\eta) = (C_{35} + C_{36}e^{-2\eta} + C_{37}e^{-2z} + C_{38}e^{-3z} + C_{39}e^{-4z})e^{-z}. \quad (5.26)$$

The coefficients $C_{30} - C_{39}$ can be easily obtained through the routine calculations.

The numerical results in the table 5.1 are prepared by using computational software

Mathematica 9. A comparison in limiting case of obtaining results with the ones from the open literature for some particular values of the governing parameter. The reported results for $f''(0)$ and $-\theta'(0)$ are not only in accordance with the physical expectations of pertinent parameters as stated overhead but also have good agreement with the existing literature [135, 136].

Table 5.1. Comparison with the existing studies as a limiting case of the considered problem against various values of Prandtl number Pr when $\varepsilon^* = 0$.

Pr	Makanda [135]		Ece [136]		Present	
	$f''(0)$	$-\theta'(0)$	$f''(0)$	$-\theta'(0)$	$f''(0)$	$-\theta'(0)$
1	0.681483	0.638854	0.681483	0.638855	0.681725	0.639421
10	0.433278	1.275529	0.433268	1.275499	0.4339191	1.276061

5.3 Results and discussion

In this chapter non-Newtonian viscoelastic nanofluid is considered as a base fluid. The Polydimethylsiloxane (PDMS) and copper nanoparticles are taken into account. To analysis the effects of emerging parameters Figs. 5.1 to 5.7 have been displayed. For the velocity and the temperature profile, $Pr = 12$ and $\varepsilon^* = 0.01$ are computed whereas the spherical shape of particle, the nano-layer thickness h_{layer} of $1nm$ and nano-layer thermal conductivity k_{layer} of $2k_f$ are used in this investigation. Fig. 5.1 shows the effects of nanofluids' thermal conductivity in the presence of copper nanoparticles. It is found that the thermal conductivity rises by increasing the particle volume fraction for different particle sizes. Considerable thermal conductivity is noted in the smaller size of particle as compared to the larger one. For instance, by considering $5nm$ and $15nm$ radii of particles, thermal conductivities are increased 31% and 27% respectively. The particle volume fraction effects on velocity and temperature profiles are showed in Figs. 5.2 and 5.3 respectively. Fig. 5.2 illustrates that when the particle concentration increases, then the velocity of fluid is condensed. It is in accordance with the physical expectation for which fluid having high viscosity cannot travel easily as compared to low viscosity of the fluid because the growth of particle fraction. On the other side, a quite opposite behavior is noted in Fig. 5.3 It is seen that the temperature of nanofluid escalations by snowballing the particle volume fraction. It is also not unforeseen for physical point of view, obviously with the

increase of volume fraction, thermal conductivity increases and consequently, temperature of fluid is enriched. Figs. 5.4 and 5.5 illustrate the particle radius effects on the velocity and temperature profiles of nanofluid respectively. In Fig. 5.4, the velocity of fluid declines by enhancement in sizes of particles. It is because of that large size particle product more resistance in fluid flow as compared to the small particles. In addition, it is also observed that temperature of fluid turns down when the radius of particle is enhanced shown in Fig. 5.5. Figs. 5.6 and 5.7 respectively demonstrate the behavior of different nanoparticles on the velocity and temperature profiles of nanofluid. The maximum velocity is found by aluminum in Fig. 5.6, followed by window glass, copper and gold particles respectively. The results in Fig. 5.7 elucidates that the maximum enhancement in temperature is occurred by gold and minimum enhanced is observed for window glass.

The numerical results in tables 5.2 and 5.3 are prepared to see the particle volume concentration and diameter of particle effects on the Skin friction and heat transfer rate coefficient of PDMS base nanofluid. The table 5.2 depicts that when volume fraction of nanoparticles increases then the wall shear stress and also heat transfer rate coefficient are increased. For example, when one chooses copper nanoparticles, then an increment in heat transfer rate coefficient of PDMS is observed 21.69% and 44.93% corresponding to 5% and 10% volume concentration of copper nanoparticles. In table 5.2, it is seen that the values for all particles show the same behavior with little bit difference on the wall shear stress and heat transfer rate coefficient. It is known that shear rate of flow and the heat transfer rate strongly depend on physical parameters of fluid. In the physical parameter, thermal conductivity is most important parameter. It is revealed in Fig.5.1 that thermal conductivity of base fluid rises by cumulative the nanoparticle volume fraction. It is seen that an enhancement in thermal conductivity of fluid yields increase in the shear rate and escalation in the shear rate causes upturn in shear stress. The heat transfer rate increases by enhancing the thermal conductivity. In the proposed model nanoparticles of four types such as Gold, Copper, Aluminum and Glass materials are engaged. Since the thermal conductivities of Gold, Copper and Aluminum have a slight difference, therefore, the particles have almost equal values for Skin friction and heat transfer rate coefficient. The effect of radius on wall stress and heat transfer rate coefficient is shown in table 5.3. It is seen that stress at wall reduces by increasing the values of concentration of particles. It has occurred due to the drag force. The heat transfer rate reduces by taking large radius of

particles. This is because of that large radius always increases the thermal resistance that is why the thermal conductivity is curtailed. For instance by taking 10nm radius, the thermal resistance increases 18% as compared to 1nm radius at 10% particle volume fraction.

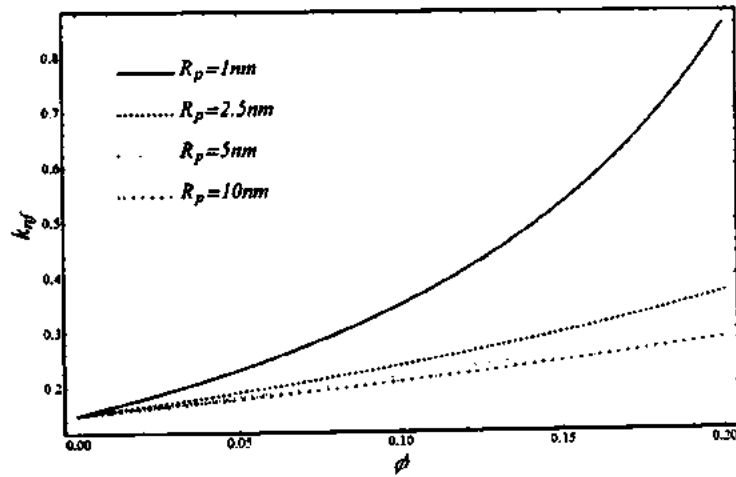


Fig. 5.1. The particle radius and volume fraction effects on thermal conductivity of nanofluid.

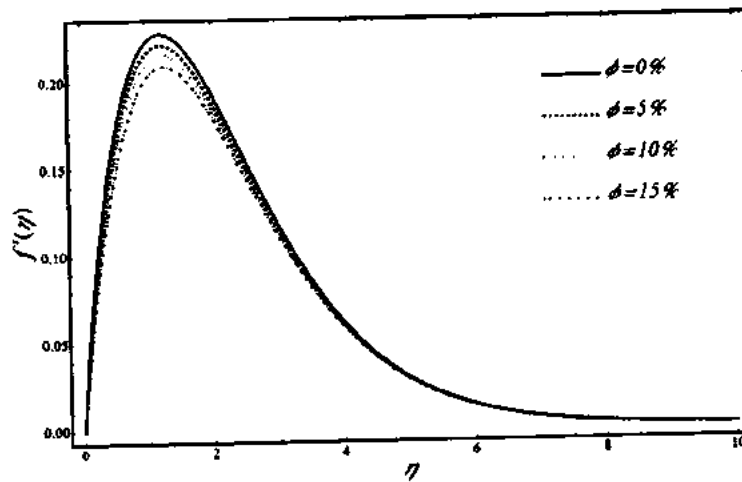


Fig. 5.2. The volume fraction effect on velocity profile when $R_p = 2.5nm$.

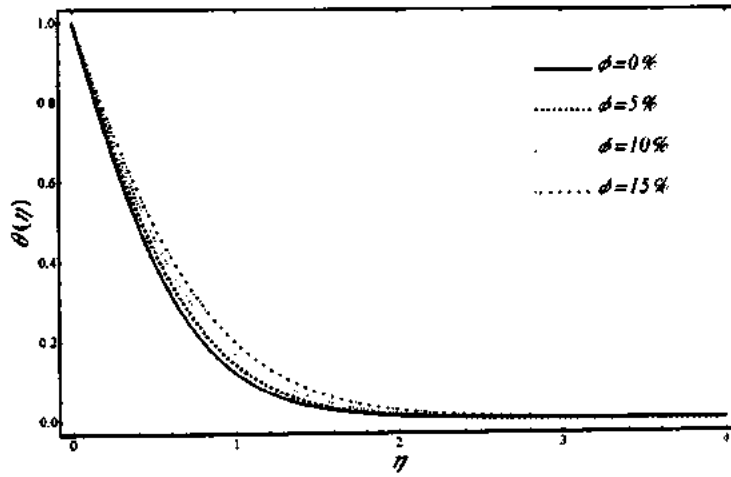


Fig. 5.3. The volume fraction effect on temperature profile when $R_p = 2.5nm$.

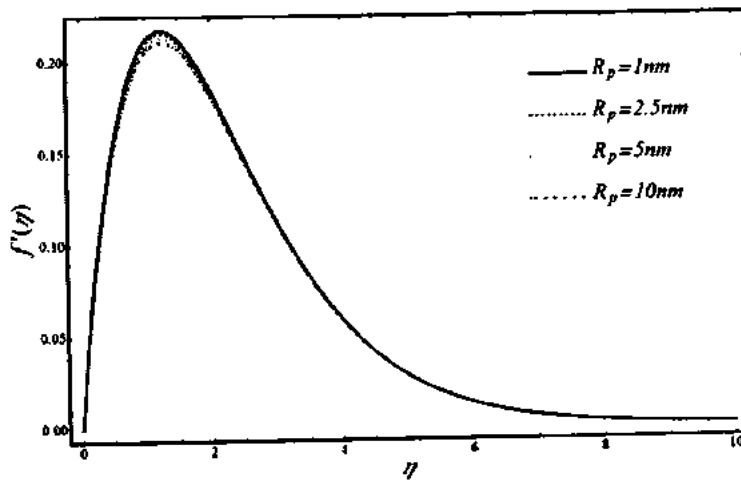


Fig. 5.4. The particle radius effect on velocity profile when $\phi = 10\%$.

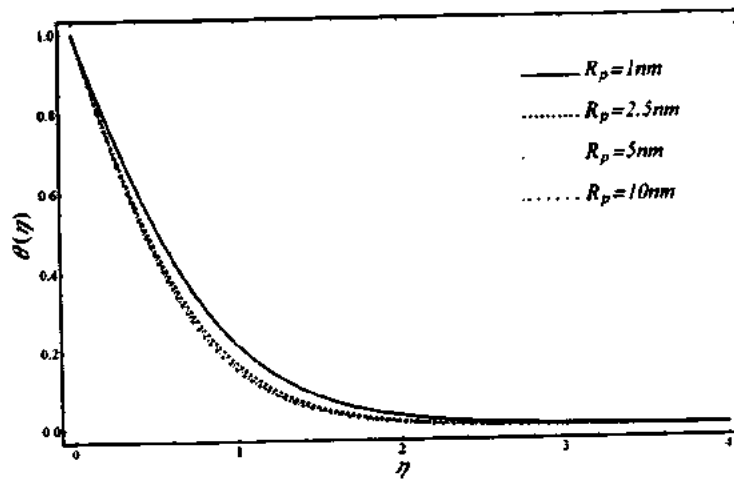


Fig. 5.5. The particle radius effect on temperature profile when $\phi = 10\%$.

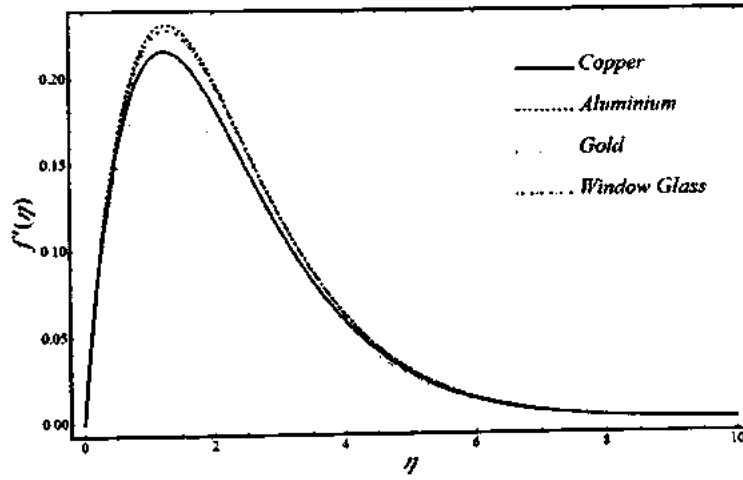


Fig. 5.6. The different particles effect on velocity profile when $\phi = 10\%$ and $R_p = 2.5nm$.

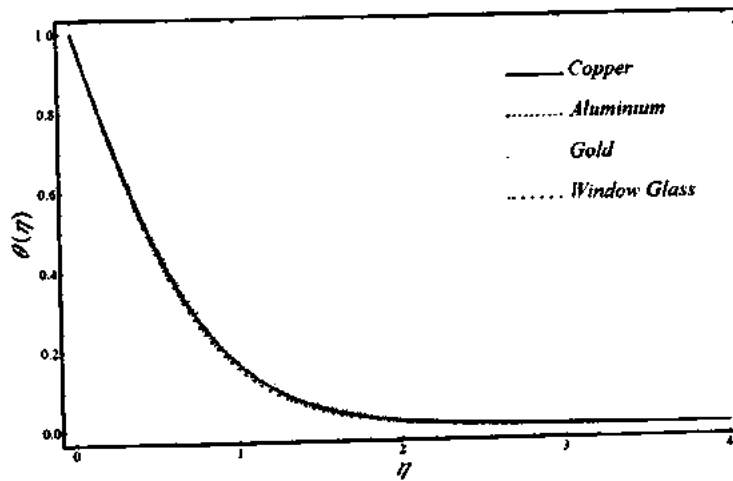


Fig. 5.7. The different particles effect on temperature profile when $\phi = 10\%$ and $R_p = 2.5nm$.

Table 5.2. The nanoparticles volume fraction effect on wall shear stress and heat transfer rate coefficient when $R_p = 2.5nm$.

ϕ	$\frac{\mu_{nf}}{\mu_f} f''(0)$				$-\frac{k_{nf}}{k_f} \theta'(0)$			
	Copper	Aluminum	Gold	Window Glass	Copper	Aluminum	Gold	Window Glass
0%	0.4452	0.4452	0.4452	0.4452	1.3553	1.3553	1.3553	1.3553
5%	0.4391	0.4416	0.4436	0.43326	1.5722	1.5625	1.5492	1.4666
10%	0.4579	0.4619	0.4697	0.4448	1.8046	1.7814	1.7581	1.5767
15%	0.4793	0.4833	0.4996	0.4568	2.0590	2.0179	1.9868	1.6869

Table 5.3. Effect of radius on wall shear stress and heat transfer rate coefficient when $\phi = 10\%$.

$\frac{\mu_{nf}}{\mu_f} f''(0)$					$-\frac{k_{nf}}{k_f} \theta'(0)$			
R_p	Copper	Aluminum	Gold	Window Glass	Copper	Aluminum	Gold	Window Glass
1nm	0.4946	0.4999	0.5056	0.4797	2.3619	2.3361	2.2918	2.0389
2.5nm	0.4579	0.4619	0.4697	0.4448	1.8046	1.7814	1.7581	1.5767
5nm	0.4495	0.45310	0.4614	0.4378	1.6919	1.6696	1.6499	1.4945
10nm	0.4456	0.4491	0.4575	0.4348	1.6418	1.6198	1.6015	1.4618

5.4 Conclusions

In this chapter natural convection in a viscoelastic nanofluid over a vertical cone is presented. The PDMS is used as base fluid along with different materials. These types of base fluid have a lot of applications in mechanical and industrial manufacturing since the low thermal conductivity of convective fluid rises by adding the nanoparticles. Due to increase in thermal conductivity of base fluid, the temperature and heat transfer rate coefficient are also increased. It is also observed that the particles having small radius effectively increase the temperature of the fluid as compared to the large radius. The volume concentration of particle increases the viscosity of viscoelastic fluid and as a matter of facts the velocity of the fluid decreases. A comparison in limiting case of the obtained results is made with the existing literature and has found good agreement.

Chapter 6

CVFEM for MHD natural convection flow of Cu-water nanofluid in elliptics cylinder

In this chapter magnetohydrodynamic influence on natural convection flow of Cu-water nanofluid in an enclosure with hot elliptic cylinder is investigated. The governing equations in dimensionless form are taken to analysis the nanofluid flow as well as heat profile. Control Volume based Finite Element Method (CVFEM) is employed to solution of these equations. The computations are done for various governing parameters, for instance the Hartmann number, nanoparticle volume fraction, the inclined angle inside cylinder and Rayleigh number. It is also investigated the average Nusselt numbers analogous to dynamic parameters.

6.1 Mathematical formulation of the problem

Nanofluid flow in the inclined elliptic cylinder is considered. The demonstration of geometry for problem is shown in Fig. 6.1. Under the Boussinesq approximation and uniform magnetic field $\mathbf{B}=(B_x, B_y)$, the governing equations are as follows

$$\frac{\partial u}{\partial x} + \frac{\partial v}{\partial y} = 0, \quad (6.1)$$

$$\rho_{nf} \left(u \frac{\partial u}{\partial x} + v \frac{\partial u}{\partial y} \right) = -\frac{\partial P}{\partial x} + \mu_{nf} \left(\frac{\partial^2 u}{\partial x^2} + \frac{\partial^2 u}{\partial y^2} \right) + (\sigma_o)_{nf} B^2 \begin{pmatrix} v \sin \lambda_1 \cos \lambda_1 \\ -u \sin^2 \lambda_1 \end{pmatrix}, \quad (6.2)$$

$$\begin{aligned} \rho_{nf} \left(u \frac{\partial v}{\partial x} + v \frac{\partial v}{\partial y} \right) &= -\frac{\partial P}{\partial y} + \mu_{nf} \left(\frac{\partial^2 v}{\partial x^2} + \frac{\partial^2 v}{\partial y^2} \right) + (\rho\beta)_{nf} g (T - T_c) \\ &+ (\sigma_o)_{nf} B^2 (u \sin \lambda_1 \cos \lambda_1 - v \cos^2 \lambda_1), \end{aligned} \quad (6.3)$$

$$(\rho C_p)_{nf} \left(u \frac{\partial T}{\partial x} + v \frac{\partial T}{\partial y} \right) = k_{nf} \left(\frac{\partial^2 T}{\partial x^2} + \frac{\partial^2 T}{\partial y^2} \right), \quad (6.4)$$

where $\lambda_1 = B_x / B_y$ and take equal to zero for current study.

In above, the physical thermal properties are given in Eqs. (1.3), (1.7), (1.8), (1.10) and (1.16) respectively. For the nanofluid, the values of thermo physical properties

are specified in table 6.1. The effective electrical conductivity for nanofluid [137] is given as

$$\frac{(\sigma_o)_{nf}}{(\sigma_o)_f} = 1 + \frac{3 \left(\frac{(\sigma_o)_s}{(\sigma_o)_f} - 1 \right) \phi}{\left(\frac{(\sigma_o)_s}{(\sigma_o)_f} + 2 \right) - \left(\frac{(\sigma_o)_s}{(\sigma_o)_f} - 1 \right) \phi}. \quad (6.5)$$

Let us introduce the following non-dimensional parameters

$$\begin{aligned} X = \frac{x}{L}, Y = \frac{y}{L}, \Omega_1 = \frac{\omega L^2}{\alpha_f}, f = \frac{\psi}{\alpha_f}, \theta = \frac{T - T_c}{T_h - T_c}, U = \frac{uL}{\alpha_f}, V = \frac{vL}{\alpha_f}, u = \frac{x}{L}, \\ Y = \frac{y}{L}, \omega = \frac{\partial v}{\partial x} - \frac{\partial u}{\partial y}, Ha = (r_{out} - r_m) B_s \sqrt{\sigma_f / \mu_f}, \\ Ra = g \beta_f (r_{out} - r_m)^3 (T_h - T_c) / (\alpha_f \nu_f). \end{aligned} \quad (6.6)$$

in above, r_{out} is outer radius, r_m is inner radius and $L = r_{out} - r_m$.

Substituting the transformations given in Eq. (6.6) into Eqs. (6.1) to (6.4) and obtained the governing equations in non-dimensional form as follows

$$\frac{\partial f}{\partial Y} \frac{\partial \Omega_1}{\partial X} - \frac{\partial f}{\partial X} \frac{\partial \Omega_1}{\partial Y} = \frac{\mu_{nf}}{\mu_f} \frac{\rho_f}{\rho_{nf}} \text{Pr} \left(\frac{\partial^2 \Omega_1}{\partial X^2} + \frac{\partial^2 \Omega_1}{\partial Y^2} \right) + Ra \text{Pr} \frac{\beta_s}{\beta_f} \left(\frac{\partial \theta}{\partial X} \right) \quad (6.7)$$

$$+ Ha^2 \text{Pr} \frac{(\sigma_o)_{nf}}{(\sigma_o)_f} \frac{\rho_{nf}}{\rho_f} \left(-\frac{\delta V}{\delta Y} \tan \lambda_1 + \frac{\delta U}{\delta Y} \tan^2 \lambda_1 + \frac{\delta U}{\delta X} \tan \lambda_1 - \frac{\delta V}{\delta X} \right),$$

$$\frac{\partial f}{\partial Y} \frac{\partial \theta}{\partial X} - \frac{\partial f}{\partial X} \frac{\partial \theta}{\partial Y} = \frac{k_{nf}}{k_f} \frac{(\rho C_p)_f}{(\rho C_p)_{nf}} \left(\frac{\partial^2 \theta}{\partial X^2} + \frac{\partial^2 \theta}{\partial Y^2} \right), \quad (6.8)$$

$$\frac{\partial^2 f}{\partial X^2} + \frac{\partial^2 f}{\partial Y^2} = -\Omega_1 \quad (6.9)$$

with subject to boundary conditions by way of Fig. 6.1 are

$$\begin{aligned} \theta = 1.0 & \quad \text{on the inner sinusoidal boundary,} \\ \theta = 0.0 & \quad \text{on the outer circular boundary,} \\ f = 0.0 & \quad \text{on all solid boundaries.} \end{aligned} \quad (6.10)$$

The local Nusselt number of the nanofluid along the cold wall can be expressed as

$$Nu = \left(\frac{k_{nf}}{k_f} \right) \frac{\partial \theta}{\partial r_1}. \quad (6.11)$$

The average Nusselt number on the circular cold wall is calculated as

$$Nu_{ave} = \frac{1}{2\pi} \int_0^{2\pi} Nu(\zeta) d\zeta. \quad (6.12)$$

6.2 Solution of the problem

In this investigation, CVFEM is applied. The triangular elements are used in building block of the discretization. The control volumes are generated by assembling the center of every element with the help of the mid points of the element edges which pass over the central node i that makes a close control volume polygonal (see Fig. 6.1(b, c)). Various mesh combinations were examined for the case of $\phi = 0.06$, $Ra = 10^5$, $a = 0.8L$, $Ha = 100$ and $Pr = 6.2$ as shown in Table 6.2. To the check validity of current results, compared with the results of experimental study [138, 139] at the different Rayleigh numbers as shown in Fig. 6.2(a, b). In addition, Fig. 6.2(c) illustrate an exceptional agreement between the current results with the outcomes of Khanafer et al. [140].

6.3 Results and discussion

Natural convective flow in nanofluid is investigated numerically via the CVFEM. Calculations are carried out for major axis ($a = 0.8L$) and Prandtl $Pr = 6.2$ at diverse values of Rayleigh number, particle concentration, Hartmann number and inclined angle of inner cylinder. The effects of Ra , γ and Ha on Isotherms and streamlines are shown in Figs. 6.3. By increasing of Rayleigh number, isotherm lines are disturbed in the absence of magnetic influence. On the other hand, these became parallel together when apply the magnetic field. This shows that magnetic influence is used to control heat transfer phenomena. On the other hand, streamlines are little magnetized that show the domination of conduction heat transfer mechanism. It is also observed in Fig. 6.3 that value of maximum stream function ($|f_{max}|$) is enlarged by increasing of Rayleigh number whereas value is diminished in the case of magnetic impact. In view of inclination angle, the stream lines and isotherms are symmetric according to the vertical center line of the enclosure when choose $\gamma = 0^\circ$. Each pair cells have two cells. The top vortex is sturdier as hot surface is placed under the cold one which facilitates to flow movement, whereas existence of cold wall below the hot resists the flow motion. As increasing of γ , these both cells have two single cells at diverse positions. The streamlines show symmetric form again with

reference to the vertical centerline when we choose $\gamma = 90^\circ$. In addition, when angle of inclination increases the absolute value of maximum stream function ($|f_{\max}|$) is increasing at different Rayleigh number.

The second set of calculation shows the impact of Hartmann number, Rayleigh number and inclination angle on the heat transfer rate (Nusselt number) along the outer circular wall in Fig. 6.4. As intensifications of Rayleigh number, the the heat transfer rate upturns due to increasing of convection effect. At $Ra = 10^3$ the heat transfer profile at outer wall is nearly symmetry subject to the horizontal center line. When Rayleigh number boosts (e.g. $Ra = 10^4$ and $Ra = 10^5$), the Nu profile is no longer symmetry and local Nusselt number is significantly small over the bottom wall. Increasing Hartmann number causes local Nusselt number to decreases. These local Nusselt number profiles are more complex due to the presence of thermal plume at the vicinity of the top wall of the enclosure.

The resultant polynomial illustration for Nusselt number as follows

$$\begin{aligned} Nu &= a_{13} + a_{23}Y_1 + a_{33}Y_2 + a_{43}Y_1^2 + a_{53}Y_2^2 + a_{63}Y_1Y_2, \\ Y_1 &= a_{11} + a_{21}Ra + a_{31}Ha + a_{41}Ra^2 + a_{51}Ha^2 + a_{61}HaRa, \\ Y_2 &= a_{12} + a_{22}\gamma + a_{32}\phi + a_{42}\gamma^2 + a_{52}\phi^2 + a_{62}\gamma\phi. \end{aligned} \quad (6.13)$$

where a_j are shown in Table 6.3. Impact of the nanoparticles concentrations, inclination angle, Hartmann number and Rayleigh number on average Nusselt number are exposed in Figs. 6.5 and 6.6. Increasing in particle volume fraction leads to raise Nusselt number by reason of decline in temperature gradient is less significant as compared to the thermal conductivity ratio due to the existence of nanoparticles. Increasing Rayleigh number is associated with an increase in the heat transfer. This is due to stronger convective heat transfer for higher Rayleigh number. Increasing Hartmann number causes to a significant dominance of the convection. Also these figures show that inclination angle has direct relationship with average Nusselt number. As seen in Fig. 6.5 inclination angle has no significant effect on average Nusselt number at high Hartmann number.

To calculate the enhancement in heat transfer among the pure fluid and nanofluid with $\phi = 0.06$ is defined as

$$En = \frac{Nu(\phi = 0.06) - Nu(\text{basefluid})}{Nu(\text{basefluid})} \times 100. \quad (6.14)$$

The effects of Ha, γ and Ra on heat transfer improvement with the presence of nanoparticles are shown in Fig. 6.7. Generally, increasing Rayleigh number causes heat transfer enhancement to decrease due to dominance of conduction mechanism in low Rayleigh number. Also Hartmann number is an cumulative function of En . As inclination angle increases En decreases except for $Ra = 10^4$. At $Ra = 10^4$ maximum values of En occur at $\gamma = 30^\circ$ and 45° for $Ha = 0$ and 100 , respectively.

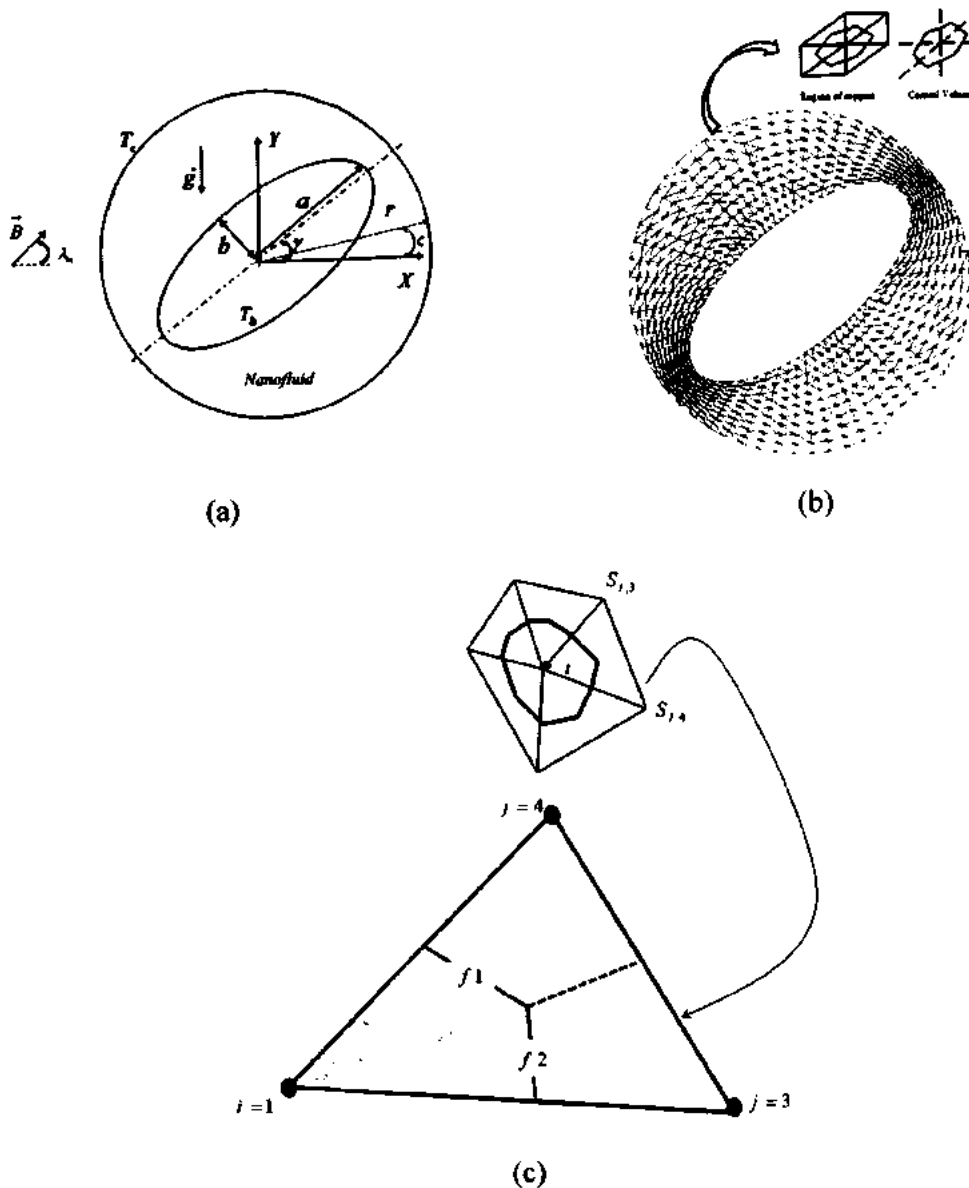


Fig. 6.1. (a) Geometry and the boundary conditions by means of (b) the mesh of enclosure considered in this investigation, (c) A sample triangular element corresponding to control volume.

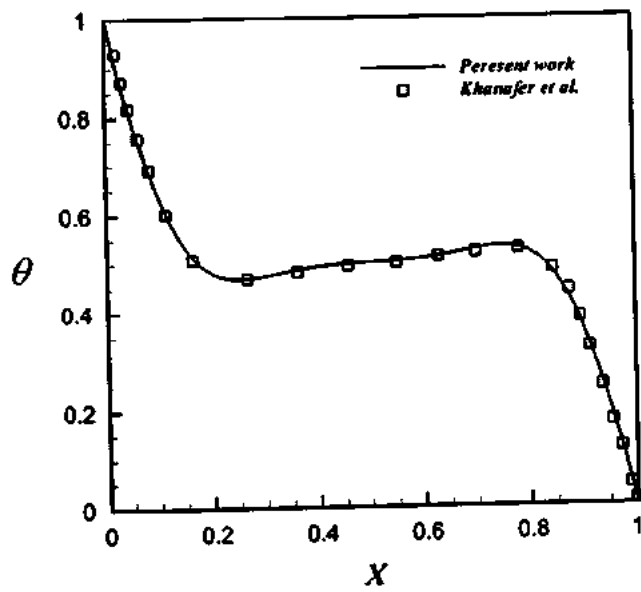
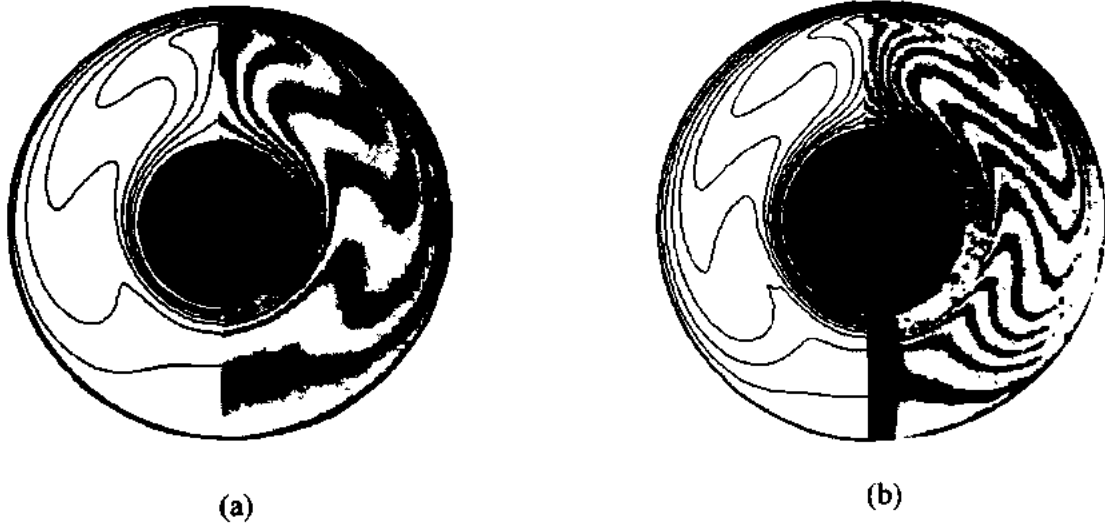
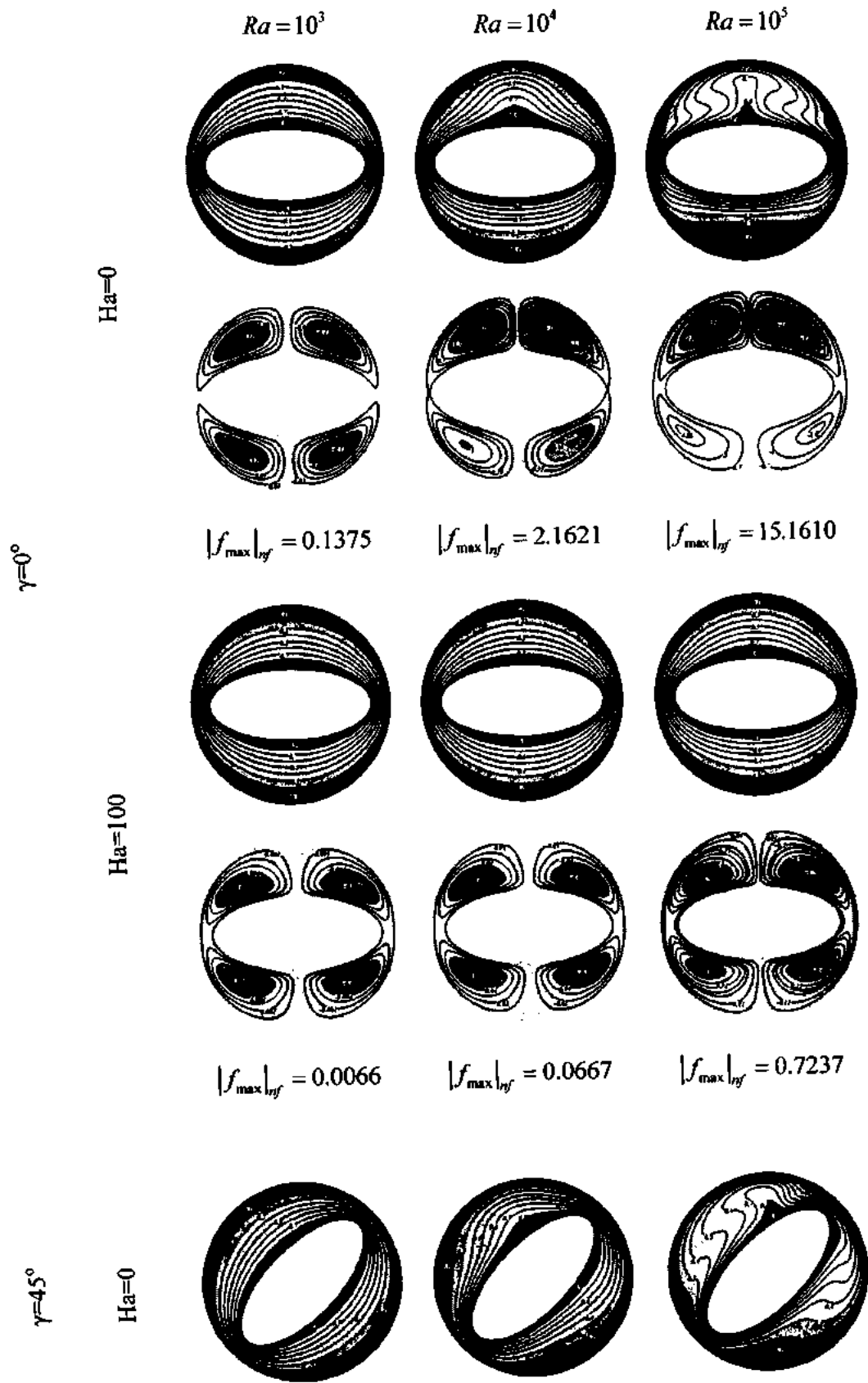


Fig. 6.2. Comparison of current results with experimental results [138, 139] when (a) $Ra = 4.7 \times 10^4$, $R_o / R_i = 2.6$, (b) $R_o / R_i = 2.36$, $Ra = 0.9 \times 10^5$; (c) Comparison of present solution among numerical results found by [140]



$\gamma=60^\circ$

Ha=100



$$|f_{\max}|_{\eta_f} = 0.4241$$



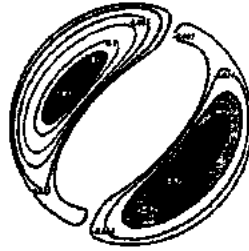
$$|f_{\max}|_{\eta_f} = 4.3791$$



$$|f_{\max}|_{\eta_f} = 20.3412$$



$$|f_{\max}|_{\eta_f} = 0.0319$$



$$|f_{\max}|_{\eta_f} = 0.3174$$



$$|f_{\max}|_{\eta_f} = 3.2041$$



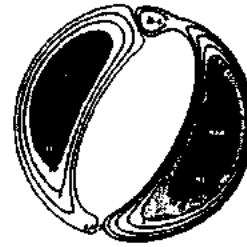
Ha=0



$$|f_{\max}|_{\eta_f} = 0.4953$$



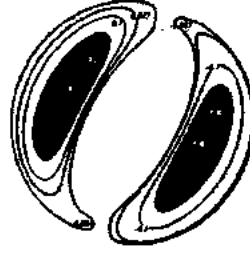
$$|f_{\max}|_{\eta_f} = 4.7301$$



$$|f_{\max}|_{\eta_f} = 21.3011$$

$\gamma=90^\circ$

Ha=100

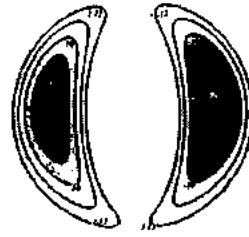
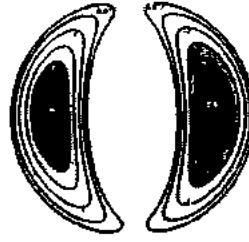
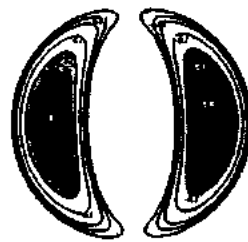
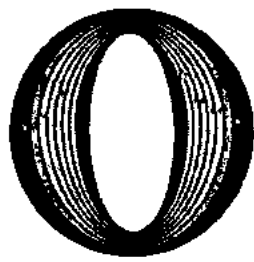


$|f_{\max}|_{\eta_f} = 0.0385$

$|f_{\max}|_{\eta_f} = 0.3837$

$|f_{\max}|_{\eta_f} = 3.7111$

Ha=0



$|f_{\max}|_{\eta_f} = 0.5506$

$|f_{\max}|_{\eta_f} = 4.7821$

$|f_{\max}|_{\eta_f} = 21.1801$

Ha=100



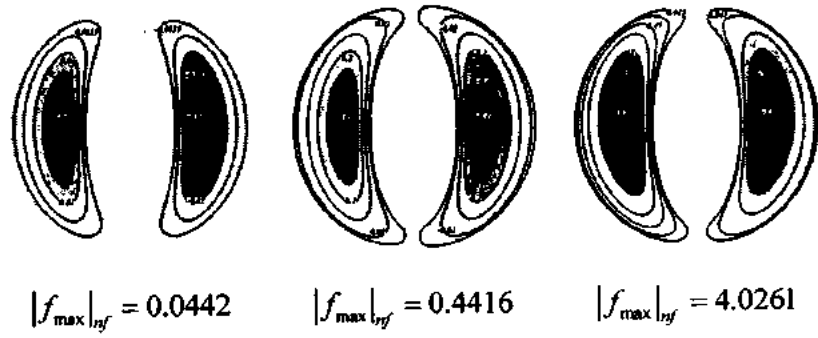
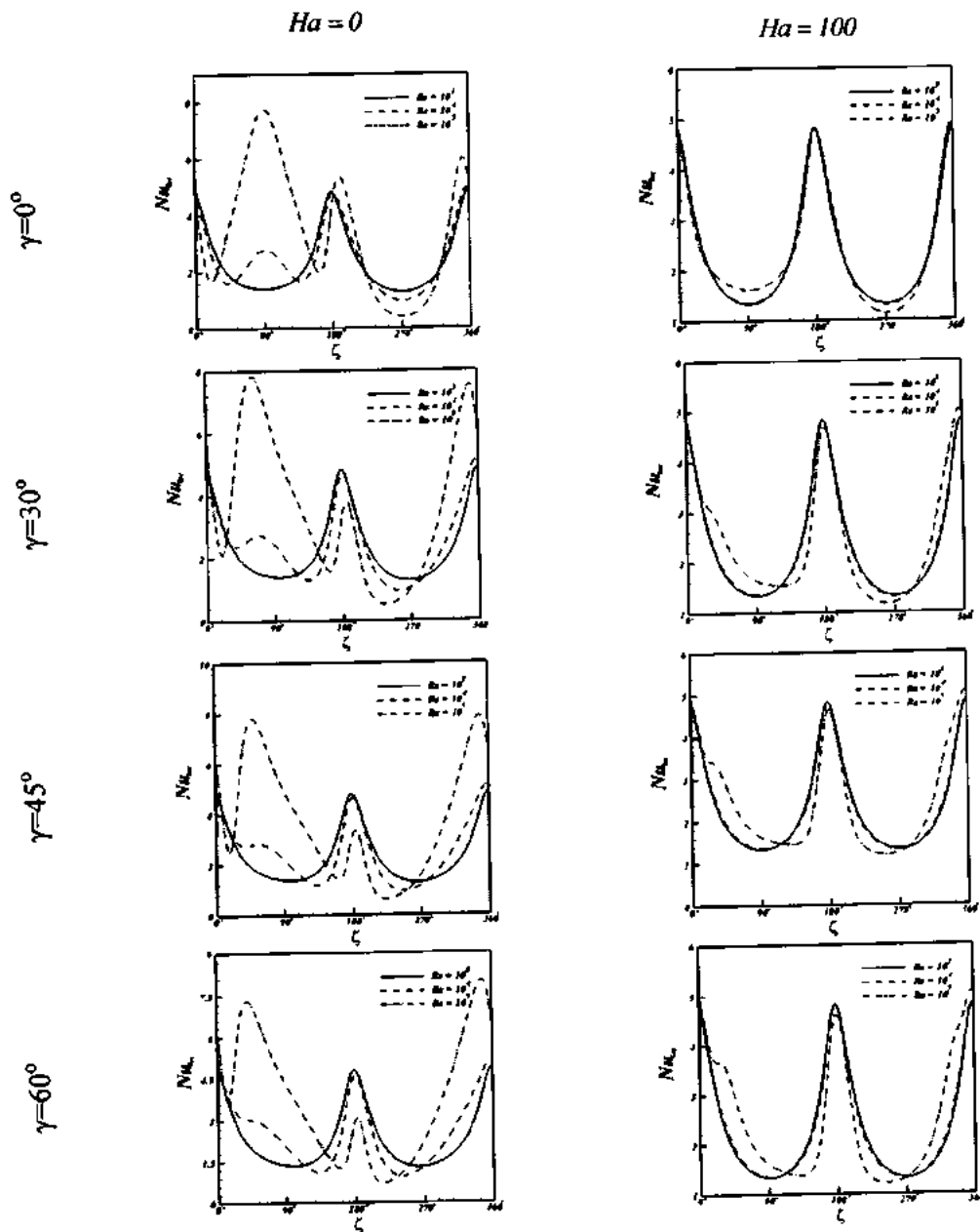


Fig. 6.3. Isotherms (up) and streamlines (down) silhouettes for different values of Ra , γ and Ha at $\phi = 0.06$.



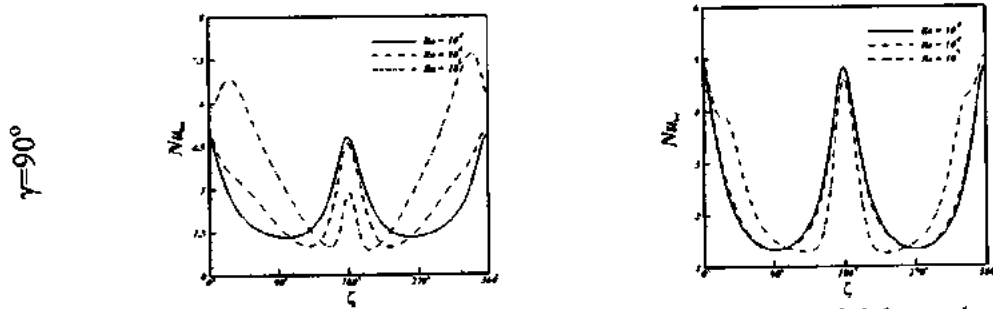


Fig. 6.4. Effects of the inclination angle, Hartmann number and Rayleigh number for *Cu*-water ($\phi = 0.06$) nanofluids on local Nusselt number.

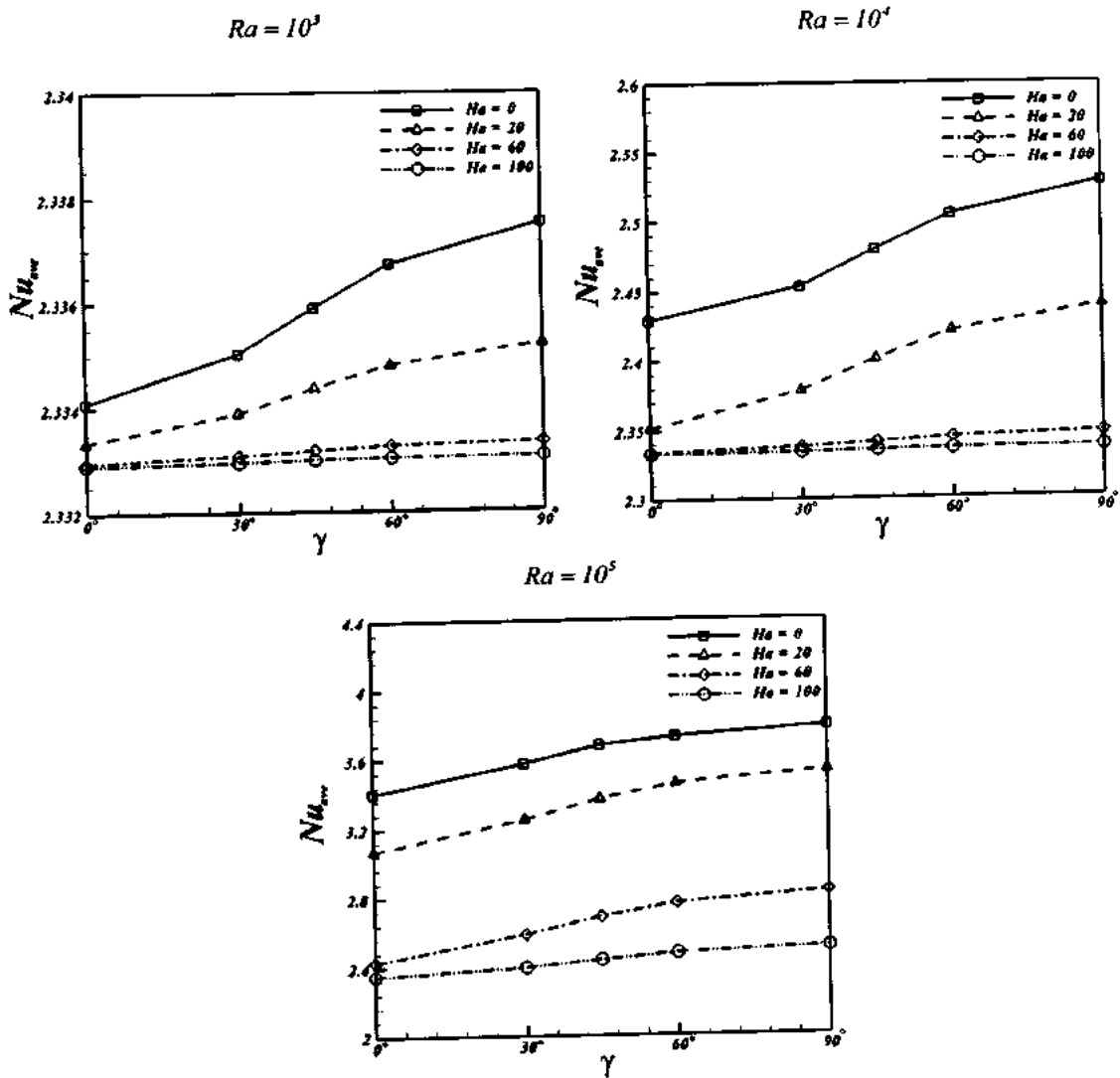
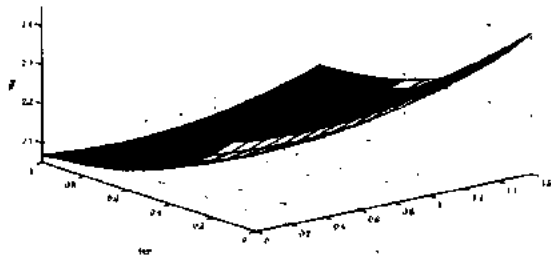
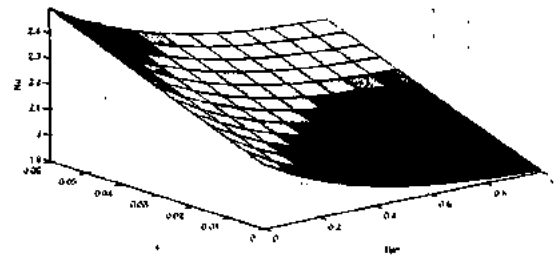


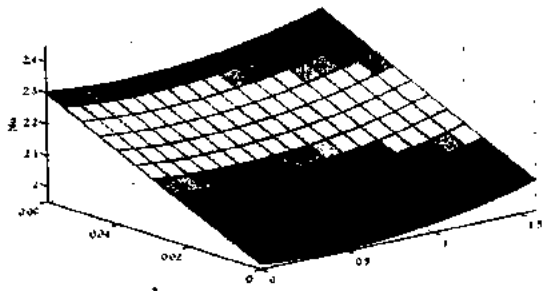
Fig. 6.5. Effects of the inclination angle, Hartmann number and Rayleigh number for *Cu*-water ($\phi = 0.06$) nanofluids on average Nusselt number.



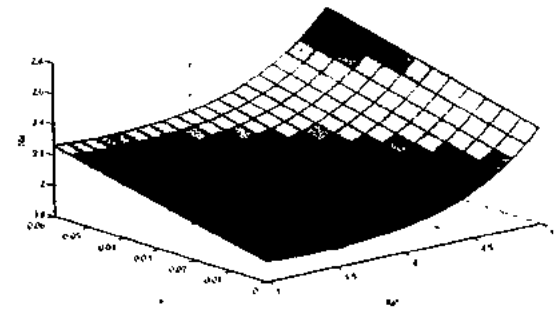
$Ra = 4, \phi = 0.03.$



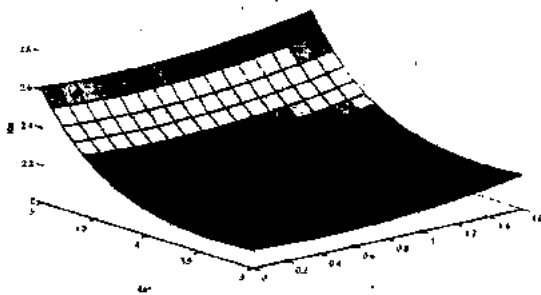
$\gamma = 0.785, Ra = 4.$



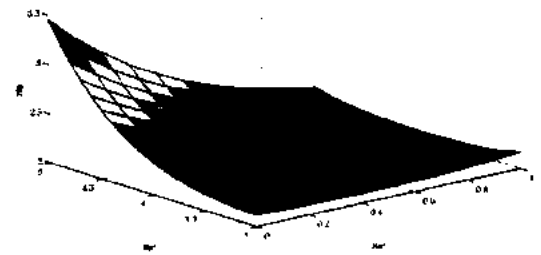
$Ra = 4, Ha = 0.45.$



$\gamma = 0.785, Ha = 0.45.$



$Ha = 0.45, \phi = 0.03.$



$\gamma = 0.785, \phi = 0.03.$

Fig. 6.6. Variation of Nu_{ave} for various input parameters.

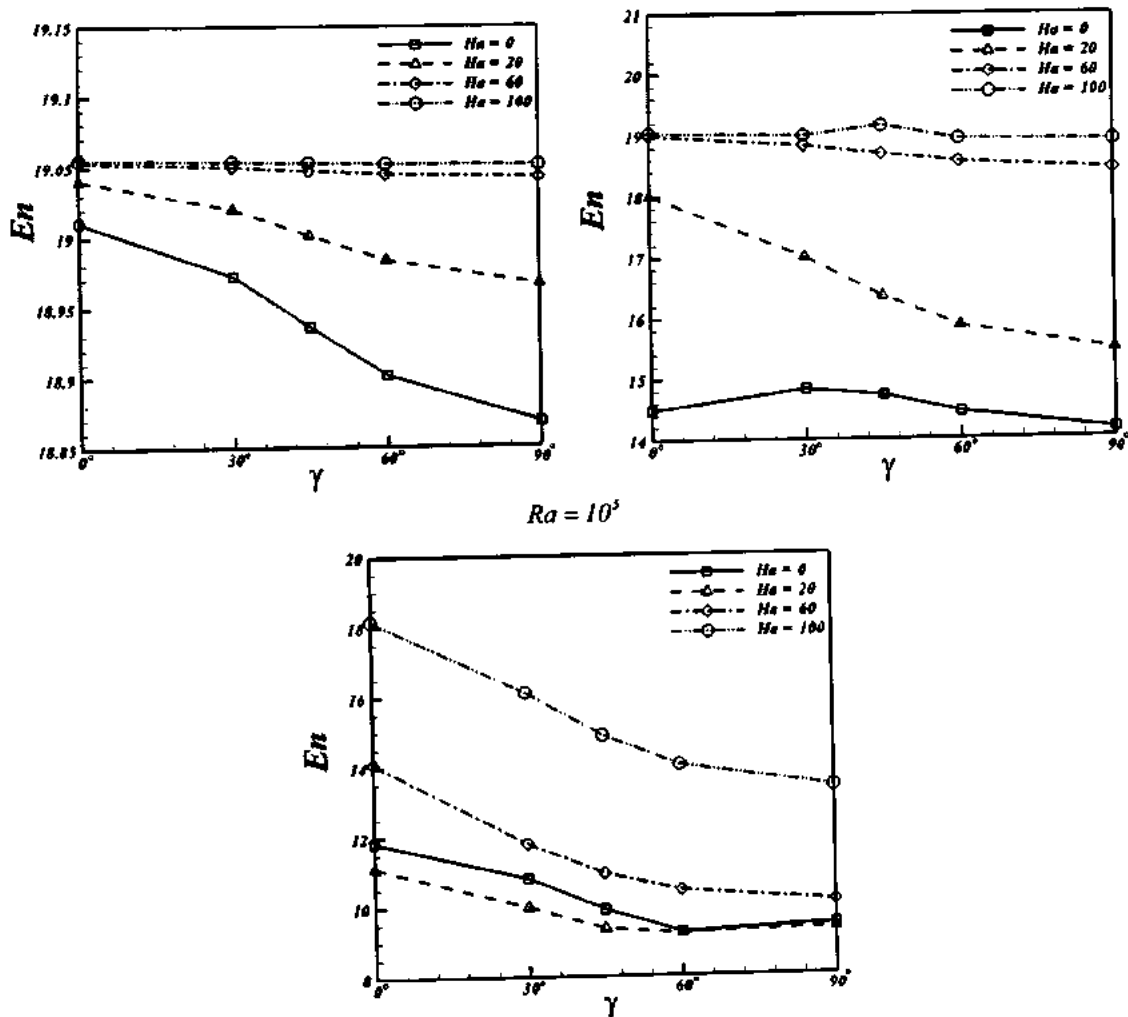


Fig. 6.7. Effects of the inclination angle, Hartmann number and Rayleigh number on the ratio of heat transfer augmentation with presence of nanoparticles at $Pr = 6.2$.

Table 6.1. Thermo physical properties of nanoparticles and base fluid.

	$\rho(\text{kg} / \text{m}^3)$	$C_p(\text{j} / \text{kgk})$	$k(\text{W} / \text{m.k})$	$\beta(\text{K}^{-1})$	$\sigma(\Omega \cdot \text{m})^{-1}$
Pure water	997.1	4179	0.613	21×10^{-5}	0.05
Copper(Cu)	8933	385	401	1.67×10^{-5}	5.96×10^7

Table 6.2. The values of average Nusselt number for various grid resolution when $Ra = 10^5$, $\varepsilon = 0.9$, $a = 0.8L$, $Ha = 100$ and $\phi = 0.06$.

Mesh size in radial direction \times angular direction						
31 \times 91	41 \times 121	51 \times 151	61 \times 181	71 \times 211	81 \times 241	91 \times 271
2.366503	2.35983	2.355852	2.35321	2.351329	2.349921	2.348827
						2.347953

Table 6.3. Constant coefficient for using Eq. (6.13).

a_j	$i=1$	$i=2$	$i=3$	$i=4$	$i=5$	$i=6$
$j=1$	4.302581	-1.52352	1.51045	0.267076	0.380695	-0.59522
$j=2$	2.170725	-0.05626	6.043703	0.071014	-2.55729	-0.09138
$j=3$	3.084162	-2.27497	-0.06891	0.556024	0.155194	0.131637

6.4 Conclusions

In this chapter, CVFEM is applied to simulate natural convection flow of nanofluid between a circular enclosure and an elliptic cylinder under MHD. The effects of inclined angle of elliptic inner cylinder, Rayleigh number, Hartmann number and volume fraction of nanoparticles on the flow of convective heat transfer have been explored. The average Nusselt number rises with intensification of nanoparticle volume fraction, Rayleigh numbers and inclination angle while it decreases with augment of Hartmann number. Effect of inclination angle on Nusselt number becomes smaller in presence of magnetic field. Enhancement in Rayleigh number causes to reduction in ratio of heat transfer enhancement whereas opposite trend is perceived for Hartmann number.

Chapter 7

Study of heat transfer in power law nanofluid

In this chapter investigate the effects of nanoparticles on mixed convection flow of power law fluid. The shear thinning polyvinyl alcohol fluid is considered as base fluid. The nanoparticles of copper for nanofluid are taken into account. To analysis the flow and temperature behavior, various mass concentrations of polyvinyl alcohol in water, different sizes and concentrations of nanoparticles are used. The effects of nanoparticle concentrations on shear stress, heat flux and thermal resistance are also presented.

7.1 Mathematical formulation of the problem

Consider the steady state, incompressible, mixed convection boundary layer flow of power-law fluid a stretching sheet. The positive x -axis is assumed along the direction of the flow and y -axis measured normal to the sheet. The flow phenomena generated as a result of linear stretching of sheet shown in Fig. 7.1.

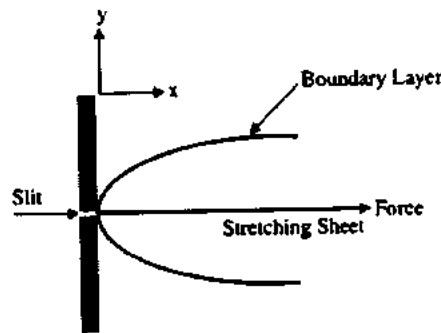


Fig. 7.1 Geometry of the problem.

Under the Boussinesq approximation, the governing equations in component form for power law model Eq. (1.43) can be written as

$$\frac{\partial u}{\partial x} + \frac{\partial v}{\partial y} = 0, \quad (7.1)$$

$$\rho_{nf} \left(u \frac{\partial u}{\partial x} + v \frac{\partial u}{\partial y} \right) = \frac{\partial}{\partial y} \left(\mu_{nf} \frac{\partial u}{\partial y} \right) + (\rho\beta)_{nf} g (T - T_{\infty}), \quad (7.2)$$

$$(\rho C_p)_{nf} \left(u \frac{\partial T}{\partial x} + v \frac{\partial T}{\partial y} \right) = k_{nf} \frac{\partial^2 T}{\partial y^2}. \quad (7.3)$$

The subjects to the following boundary condition are

$$\left. \begin{aligned} u(x,0) = u(x) = U = ax, \quad v(x,0) = 0, \\ T(x,0) = T_\infty + A \left(\frac{x}{l} \right), \\ u(x,\infty) = 0, \quad T(x,\infty) = T_\infty \end{aligned} \right\}. \quad (7.4)$$

In the above, u and v are the velocity components in the x and y directions respectively. In the Eqs. (7.2) and (7.3), the models for physical parameters are given in Eqs. (1.3), (1.7) and (1.8) respectively. The thermal conductive model of nanofluid for nano-layer effect and the viscosity model of nanofluid are defined in Eqs. (1.14) and (1.23) respectively. The μ_f is defined for power law fluid as follow

$$\mu_f = K \left(\frac{\partial u}{\partial y} \right)^{n-1}. \quad (7.5)$$

In order to solve of equations, introduce the following similarity variables

$$\left. \begin{aligned} \eta = \frac{y}{x} (\text{Re}_x)^{\frac{1}{1+n}}, \quad \psi = Ux (\text{Re}_x)^{\frac{1}{1+n}} f(\eta), \\ \theta(\eta) = \frac{T - T_\infty}{T_w - T_\infty}, \quad u = \frac{\partial \psi}{\partial y}, \quad v = -\frac{\partial \psi}{\partial x} \end{aligned} \right\} \quad (7.6)$$

and substituting into equations (7.1) to (7.4). The non-dimensional ordinary differential equations along with the associated boundary conditions can be written as

$$\frac{\rho_{nf}}{\rho_f} \left\{ f'^2 - \left(\frac{2n_1}{n_1+1} \right) f f'' \right\} = \left(\frac{1 + (2.5\phi_c)}{+(2.5\phi_c)^2 + \dots} \right) (n_1 |f'|^{n-1}) f''' + \lambda \frac{(\rho\beta)_{nf}}{(\rho\beta)_f} \theta, \quad (7.7)$$

$$\text{Pr} \frac{(\rho C_p)_{nf}}{(\rho C_p)_f} \left\{ f' \theta - \left(\frac{2n_1}{n_1+1} \right) f \theta' \right\} = \frac{k_{nf}}{k_f} \theta'', \quad (7.8)$$

$$\left. \begin{aligned} f(0) = 0, \quad f'(0) = 1, \quad f'(\infty) = 0, \\ \theta(0) = 1, \quad \theta(\infty) = 0 \end{aligned} \right\}. \quad (7.9)$$

Where $\text{Pr} = \frac{ax^2}{\alpha_f} (\text{Re}_x)^{\frac{2}{1+n}}$ is modified Prandtl number, $Gr_x = \frac{g\beta(T_w - T_\infty)\rho_f x a^{-n}}{K}$ is

local Grashof number, $\text{Re}_x = \frac{\rho_f U^{2-n} x^n}{K}$ is local Reynolds number and $\lambda = \frac{Gr_x}{\text{Re}_x}$ is

the mixed convection parameter.

Shear stress and heat flux

The shear stress can be expressed as

$$\tau = K \left(1 + (2.5\phi_c) + (2.5\phi_c)^2 + (2.5\phi_c)^3 + \dots \right) \left(\frac{\partial u}{\partial y} \right)^{n_1-1} \frac{\partial u}{\partial y}, \quad (7.10)$$

where the consistency index K and exponent index n_1 have the different values for different concentration of polyvinyl alcohol as follow below the table 7.1.

Table 7.1. Rheological properties of PVC solutions [143] and power law equation.

PV C (%)	consistenc y index	exponen t index	Shear stress
2	0.00494	0.790	$\tau = 4.94 \times 10^{-3} \left(1 + (2.5\phi_c) + (2.5\phi_c)^2 + (2.5\phi_c)^3 + \dots \right) \left(\frac{\partial u}{\partial y} \right)^{0.79}$
3	0.00925	0.764	$\tau = 9.27 \times 10^{-3} \left(1 + (2.5\phi_c) + (2.5\phi_c)^2 + (2.5\phi_c)^3 + \dots \right) \left(\frac{\partial u}{\partial y} \right)^{0.76}$
4	0.01557	0.734	$\tau = 1.56 \times 10^{-2} \left(1 + (2.5\phi_c) + (2.5\phi_c)^2 + (2.5\phi_c)^3 + \dots \right) \left(\frac{\partial u}{\partial y} \right)^{0.73}$
5	0.02170	0.718	$\tau = 2.17 \times 10^{-2} \left(1 + (2.5\phi_c) + (2.5\phi_c)^2 + (2.5\phi_c)^3 + \dots \right) \left(\frac{\partial u}{\partial y} \right)^{0.72}$

The wall shear stress can be expressed in term of Skin friction coefficient is given

$$C_f = \frac{2\tau_w}{\rho u_w^2}, \quad (7.11)$$

where

$$\tau_w = K \left(1 + (2.5\phi_c) + (2.5\phi_c)^2 + (2.5\phi_c)^3 + \dots \right) \left(\frac{\partial u}{\partial y} \right)^n_{y=0} \quad (7.12)$$

and the dimensionless form of Skin friction is as follow

$$\text{Re}_x^{1/2} C_f = 2 \left(1 + (2.5\phi_c) + (2.5\phi_c)^2 + (2.5\phi_c)^3 + \dots \right) f''(0)^n. \quad (7.13)$$

The heat flux can be found in terms as

$$q_1 = -k_w \left(\frac{\partial T}{\partial y} \right). \quad (7.14)$$

The heat flux and expressions at concentrations of polyvinyl alcohol are shown in table 7.2.

Table 7.2. Thermal conductivity of PVC solutions and heat flux equation.

PVC (%)	Thermal conductivity	Heat flux
2	0.586	$q_1 = -0.586 \frac{k_{pe} + 1.172 + 2(k_{pe} - .586)(1 + \beta^*)^3 \phi \left(\frac{\partial T}{\partial y}\right)}{k_{pe} + 1.172 - (k_{pe} - .586)(1 + \beta^*)^3 \phi}$
3	0.579	$q_1 = -0.579 \frac{k_{pe} + 1.158 + 2(k_{pe} - .579)(1 + \beta^*)^3 \phi \left(\frac{\partial T}{\partial y}\right)}{k_{pe} + 1.158 - (k_{pe} - .579)(1 + \beta^*)^3 \phi}$
4	0.572	$q_1 = -0.572 \frac{k_{pe} + 1.44 + 2(k_{pe} - .572)(1 + \beta^*)^3 \phi \left(\frac{\partial T}{\partial y}\right)}{k_{pe} + 1.144 - (k_{pe} - .572)(1 + \beta^*)^3 \phi}$
5	0.566	$q_1 = -0.566 \frac{k_{pe} + 1.132 + 2(k_{pe} - .566)(1 + \beta^*)^3 \phi \left(\frac{\partial T}{\partial y}\right)}{k_{pe} + 1.132 - (k_{pe} - .566)(1 + \beta^*)^3 \phi}$

The heat transfer coefficient defined as

$$h = -\frac{k_{ef} \left(\frac{\partial T}{\partial y}\right)_{y=0}}{T_w - T_\infty} \quad (7.15)$$

and the local Nusselt number is which defined as

$$Nu = \frac{hx}{k_f} \quad (7.16)$$

The dimensionless form of Nusselt number is as follow

$$Re_s^{-1/2} Nu = -\frac{k_{ef}}{k_f} \theta'(0) \quad (7.17)$$

7.2 Solution of the problem

We now solve these nonlinear boundary value equations by the OHAM. For the requirement of method, we choose initial guesses and linear operators are follow

$$\mathcal{L}_1 = \frac{d^3}{d\eta^3} - \frac{d}{d\eta}, \quad \mathcal{L}_2 = \frac{d^2}{d\eta^2} - 1, \quad (7.18)$$

$$f_0(\eta) = \frac{1}{2} + \left(\frac{1}{2}e^{-\eta} - 1\right)e^{-\eta}, \quad \theta_0(\eta) = e^{-\eta}. \quad (7.19)$$

Construct the zero-order deformation

$$(1-q)\mathcal{L}_1[\hat{f}(\eta, q) - f_0(\eta)] = qc_0^f N_s[\hat{f}(\eta, q), \hat{\theta}(\eta, q)], \quad (7.20)$$

$$(1-q)\mathcal{L}_2[\hat{\theta}(\eta, q) - \theta_0(\eta)] = qc_0^\theta N_6[\hat{f}(\eta, q), \hat{\theta}(\eta, q)], \quad (7.21)$$

$$\left. \begin{aligned} \hat{f}(\eta, q) = 0, \quad \frac{\partial \hat{f}(\eta, q)}{\partial \eta} = 1, \quad \hat{\theta}(\eta, q) = 1 \text{ at } \eta = 0 \\ \frac{\partial \hat{f}(\eta, q)}{\partial \eta} = 0, \quad \hat{\theta}(\eta, q) = 0, \quad \text{at } \eta \rightarrow \infty \end{aligned} \right\}. \quad (7.22)$$

In above, c_0^f and c_0^θ auxiliary parameters. Moreover the nonlinear operators N_s and N_6 defined as

$$\begin{aligned} N_s[\hat{f}(\eta, q), \hat{\theta}(\eta, q)] = & -\frac{\rho_f}{\rho_f} \left\{ n_1 \hat{f}^{\prime 2}(\eta, q) - \left(\frac{n_1 + 1}{2} \right) \hat{f}(\eta, q) \hat{f}''(\eta, q) \right\} \\ & + \frac{\mu_f}{\mu_f} \left(n_1 |\hat{f}''(\eta, q)|^{\epsilon_1} \right) \hat{f}'''(\eta, q) + \lambda \frac{(\rho\beta)_f}{(\rho\beta)_f} \hat{\theta}(\eta, q). \end{aligned} \quad (7.23)$$

$$\begin{aligned} N_6[\hat{f}(\eta, q), \hat{\theta}(\eta, q)] = & -Pr \frac{(\rho C_p)_f}{(\rho C_p)_f} \left\{ \hat{f}'(\eta, q) \hat{\theta}(\eta, q) - \left(\frac{2n}{n+1} \right) \hat{f}(\eta, q) \hat{\theta}'(\eta, q) \right\} \\ & + \frac{k_f}{k_f} \hat{\theta}''(\eta, q). \end{aligned} \quad (7.24)$$

Here $\epsilon_1 = n_1 - 1$. When $q = 0$ and $q = 1$, we have,

$$\begin{aligned} \hat{f}(\eta, 0) = f_0(\eta), \quad \hat{\theta}(\eta, 0) = \theta_0(\eta), \\ \hat{f}(\eta, 1) = f(\eta), \quad \hat{\theta}(\eta, 1) = \theta(\eta). \end{aligned} \quad (7.25)$$

Expand $\hat{f}(\eta, q)$ and $\hat{\theta}(\eta, q)$ in Taylor's series as

$$\begin{aligned} \hat{f}(\eta, q) = f_0(\eta) + \sum_{l=1}^{\infty} f_l(\eta) q^l, \\ \hat{\theta}(\eta, q) = \theta_0(\eta) + \sum_{l=1}^{\infty} \theta_l(\eta) q^l, \end{aligned} \quad (7.26)$$

where

$$\theta_l(\eta) = \frac{1}{l!} \frac{\partial \theta^l(\eta, q)}{\partial q^l} \Big|_{q=0}, \quad f_l(\eta) = \frac{1}{l!} \frac{\partial f^l(\eta, q)}{\partial q^l} \Big|_{q=0}. \quad (7.27)$$

When $q = 1$, series converge and thus

$$f(\eta) = f_0(\eta) + \sum_{k=1}^l f_k(\eta), \quad \theta(\eta) = \theta_0(\eta) + \sum_{k=0}^l \theta_k(\eta). \quad (7.28)$$

The resulting problems at the l th – order deformation are

$$\mathcal{L}_1[f_l(\eta) - \chi_l f_{l-1}(\eta)] = c_0^f R1_l(\eta), \quad (7.29)$$

$$\mathcal{L}_2[\theta_l(\eta) - \chi_l \theta_{l-1}(\eta)] = c_0^\theta R2_l(\eta), \quad (7.30)$$

$$f_l(0) = 0, \quad \frac{\partial f_l(0)}{\partial \eta} = 1, \quad \theta_l(0) = 0, \quad (7.31)$$

$$\frac{\partial f_l(\infty)}{\partial \eta} = 0, \quad \theta_l(\infty) = 0,$$

where

$$R1_l(\eta) = -\frac{\rho_{nf}}{\rho_f} \left\{ \sum_{k=0}^l f_k' f_{l-k}' - \left(\frac{2n_1}{n_1+1} \right) \sum_{k=0}^l f_k' f_{l-k}'' \right\} \\ + \left(1 + (2.5\phi_e) + (2.5\phi_e)^2 + \dots \right) n_1 H_{e_1,k} + \lambda \frac{(\rho\beta)_{nf}}{(\rho\beta)_f} \theta_l, \quad (7.32)$$

$$R2_l(\eta) = \text{Pr} \frac{(\rho C_p)_{nf}}{(\rho C_p)_f} \left[\sum_{k=0}^l \theta_k f_{l-k}' - \left(\frac{2n_1}{n_1+1} \right) \sum_{k=0}^l f_k \theta_{l-k}' \right] - \frac{k_{nf}}{k_f} \theta_l''. \quad (7.33)$$

In which

$$H_{e_1,k} = \frac{1}{k!} \left\{ \frac{\partial^k}{\partial q^k} \left(\frac{\partial^3 \hat{f}}{\partial \eta^3} \left[\frac{\partial^3 \hat{f}}{\partial \eta^3} \right]^{n_1} \right) \right\} \Bigg|_{q=0}. \quad (7.34)$$

Note that the series solutions contain the nonzero auxiliary parameters c_0^f and c_0^θ determine the convergence-region and rate of the Homotopy series solutions. The optimal values c_0^f and c_0^θ , are found by using average residual error which is defined as

$$E_f = \int_0^\infty \left[\frac{-\rho_{nf}}{\rho_f} \left\{ n_1 f'^2 - \left(\frac{n_1+1}{2} \right) f f'' \right\} + \left(\frac{1 + (2.5\phi_e)}{(2.5\phi_e)^2 + \dots} \right) (n_1 |f|^{n_1-1}) f'' + \lambda \frac{(\rho\beta)_{nf}}{(\rho\beta)_f} \theta \right]^2 d\eta, \quad (7.35)$$

$$E_\theta = \int_0^\infty \left[\text{Pr} \frac{(\rho C_p)_{nf}}{(\rho C_p)_f} \left\{ f' \theta - \left(\frac{2n_1}{n_1+1} \right) f \theta' \right\} - \frac{k_{nf}}{k_f} \theta'' \right]^2 d\eta. \quad (7.36)$$

The total squared residual error is follow

$$E_{total} = E_f + E_\theta. \quad (7.37)$$

To check the accuracy of this code for OHAM, compare values of $Re_x^{-1/2} Nu$ with the results obtained by Azeem [144] shown in table 7.3 The optimal values are also shown in table 7.3 on which results show the good agreement for the accuracy.

Table 7.3. Comparison of the obtained results with the ones from the open literature against.

$n_1 = 1$ and $Pr = 1.$					$n_1 = 2$ and $Pr = 1.$			
λ	c_0^f	c_0^θ	Present	Azeem	c_0^f	c_0^θ	Present	Azeem
0	-1.15	-0.88	0.6762	0.6762	-0.85	-0.81	0.7232	0.7215
0.5	-1.04	-0.84	0.7170	0.7188	-0.82	-0.80	0.7520	0.7560
1	-0.56	-0.79	0.7532	0.7546	-0.54	-0.77	0.7869	0.7875

7.3 Results and discussion

To effects of emerging parameters involved in the expression of velocity and temperature distributions of shear shear-thinning based nanofluids contained Cu nanoparticles are examined through Figs. 7.2 to 7.7. In the study, the value of Modified Prandtl number Pr and λ mixed convection parameter depend on stretching velocity and fluid nature. To see the effect of particle volume fraction, particle size and different concentration of PVC on velocity and temperature, take the values of modified Prandtl number and mixed convection parameter shown in table 7.2.

Table 7.4. The values of different parameters corresponding to different nanofluids.

$U(m/s)$	$x(m)$	PVC (%)	Pr	Gr_x	Re_x	λ
0.2	0.01	2	8.491	4.1004	764.22	0.00536
		3	14.24	2.3658	442.95	0.00534
		4	20.85	1.5438	289.04	0.00534
		5	27.36	1.1666	218.44	0.00534

In addition, consider the spherical shape of particle, the nanolayer thickness h_{layer} of $1nm$ and nanolayer thermal conductivity k_{layer} of $2k_f$ used in our calculation. The effect of particle volume fraction on velocity and temperature profile shown in Figs.

7.2 and 7.3 respectively. Fig. 7.2 point out that when the particle concentration is increased, the velocity of fluid is reduced. On the other hand, in Fig. 7.3, the temperature profile is enhanced by raising the particle volume fraction. This is due fact that the temperature of fluid is enlarged when the thermal conductivity is raised. Figs. 7.4 and 7.5 illustrate the effect of particle radius on the velocity and temperature profiles of nanofluid respectively. In Fig. 7.4, the velocity of fluid is decreased when size of particle is increased. In addition, it is also observe that temperature of fluid is turn down when radius of particle enhanced. It is observing that when size of particle increase the Brownian motion of particles slowdown that effect on velocity and temperature of the fluid. Figs. 7.6 and 7.7 demonstrate the behavior of different concentrations of PVC on the velocity and temperature profiles of nanofluid respectively. It is examined in Fig. 7.6, the velocity of nanofluid is increased when concentration of PVC is enhanced. The results in Fig. 7.7 demonstrate that decrement in temperature is occurred near to wall and far from wall is enhanced by mass concentration increasing in water.

The second set of results show the effect on shear stress and heat flux by adding nanoparticles in PVC solution. Figs. 7.8 and 7.9 illustrate the effects of particles volume fraction on shear stress in x and y directions respectively. In Fig. 7.8, shear stress is increased by increasing particle volume fraction. It is also observe that shear stress is increase near to slit and after some distance in shear stress have no effective change. The shear stress in the direction of y -axis is increase by increasing particles volume fraction shown in Fig. 7.9. Figs. 7.10 and 7.11 show the effect of particle volume fraction on heat flux along x -axis and y -axis. It is analysis in Fig. 7.10 that heat flux along x -axis is increased by increasing particle volume fraction. This due to that thermal conductivity increases by enrichment of volume concentration of nanoparticles and notice that nanoparticles act the behavior like bridge to pass heat flow. It is also noticed that heat flux near to slit increase readily and then became constant after some length of plate. Fig. 7.11 depicts that when volume fraction of nanoparticles is increased, the heat flux also increase in the region of boundary layer. Fig. 7.12 shows the effect of volume concentration of particles on thermal resistance at the wall. It is seen that thermal resistance reduce by increasing the concentration of particles. It is happen due to increasing the heat flux enhancement in particle concentration.

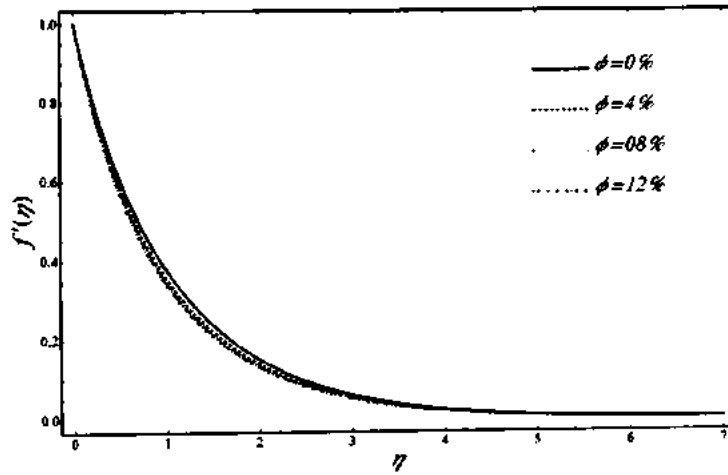


Fig. 7.2. Effect of particle volume fraction on velocity profile when $R_p = 10nm$.

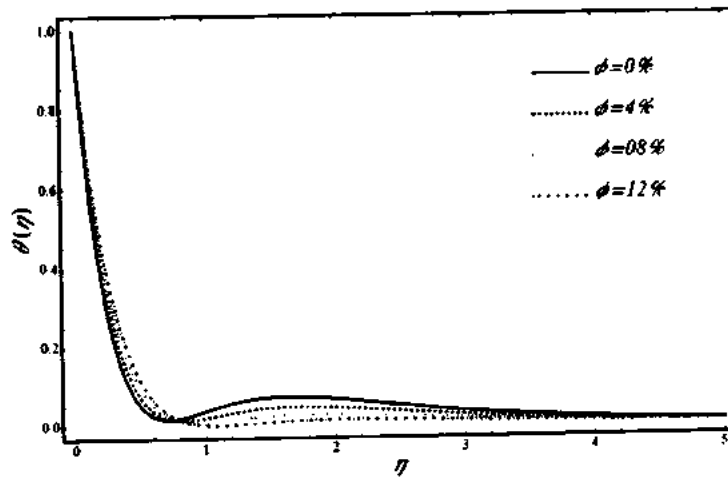


Fig. 7.3. Effect of particle volume fraction on temperature profile when $R_p = 10nm$.

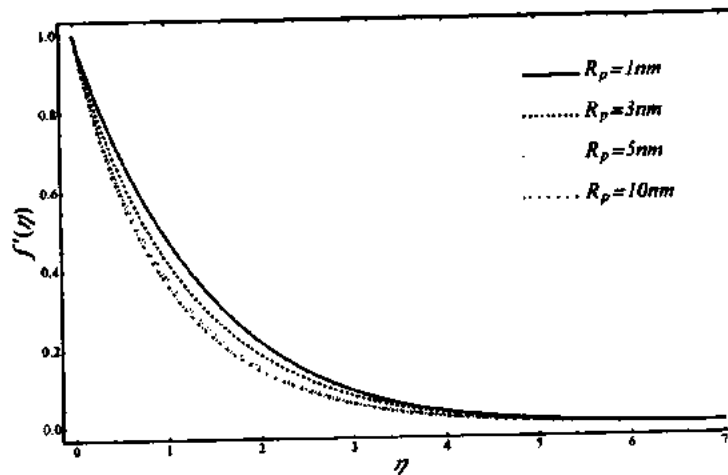


Fig. 7.4. Effect of particle radius on velocity profile when $\phi = 4\%$.

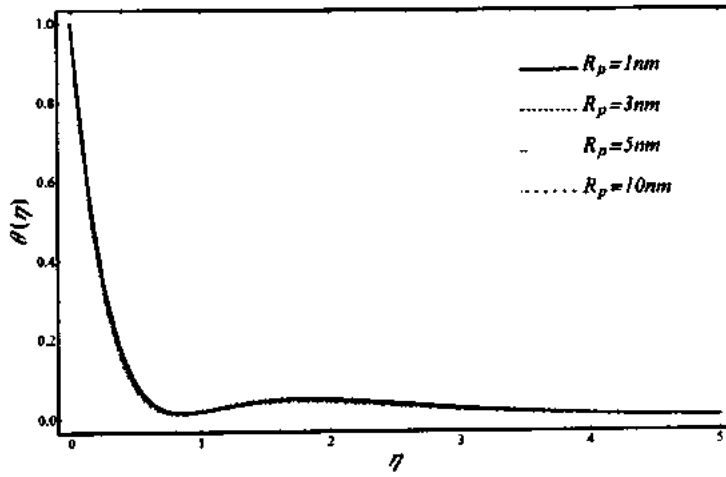


Fig. 7.5. Effect of particle radius on temperature profile when $\phi = 4\%$.

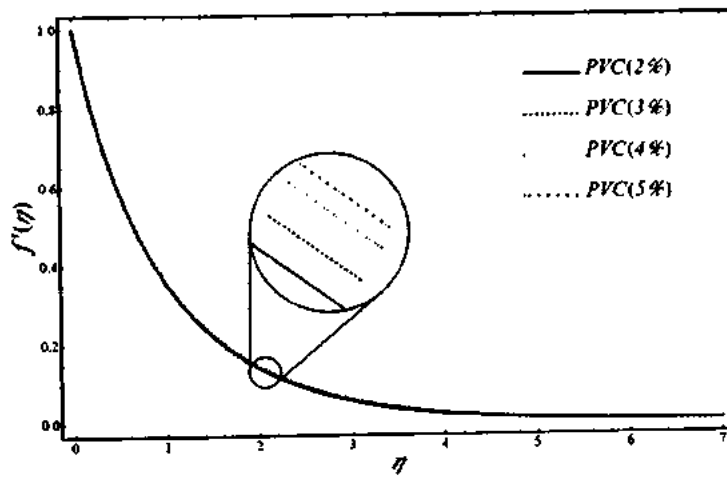


Fig. 7.6. Effect of PVC concentration on velocity profile when $\phi = 4\%$ and $R_p = 10nm$.

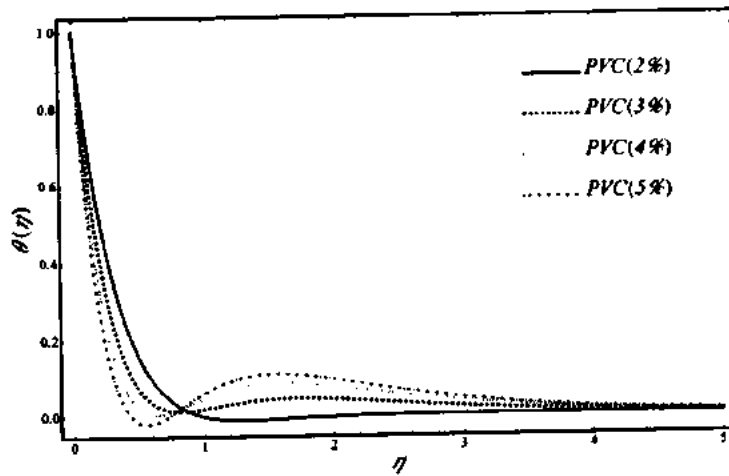


Fig. 7.7. Effect of PVC concentration on temperature profile when $\phi = 4\%$ and $R_p = 10nm$.

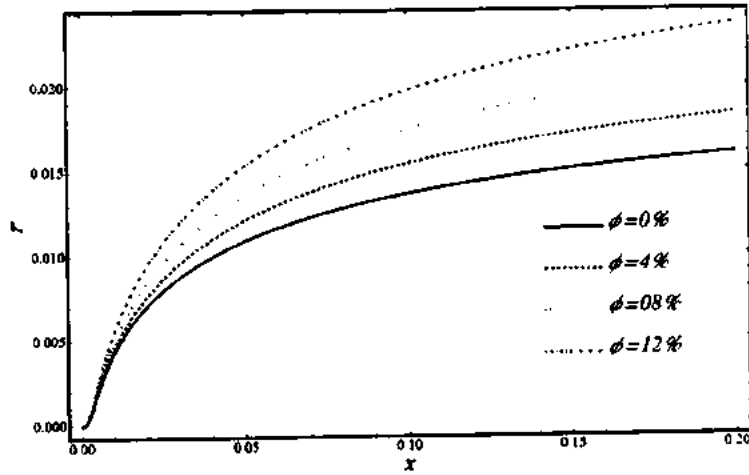


Fig. 7.8. Effect of particle volume fraction on shear stress in x -direction when $R_p = 10nm$.

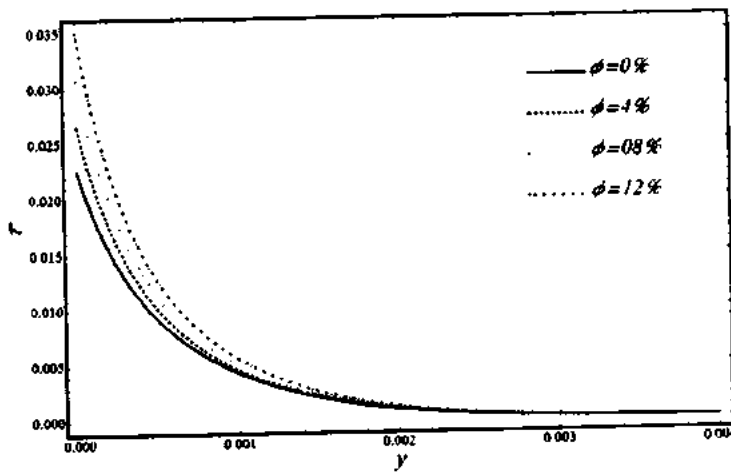


Fig. 7. 9. Effect of particle volume fraction on shear stress in y -direction when $R_p = 10nm$.

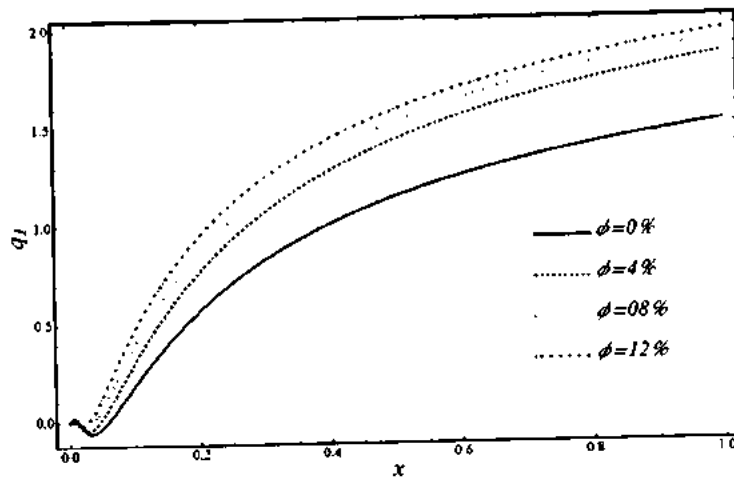


Fig. 7.10. Effect of particle volume fraction on heat flux in x -direction when $R_p = 10nm$.

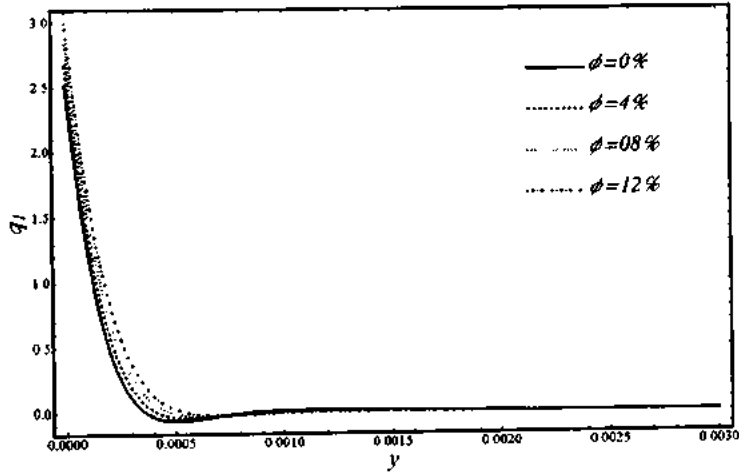


Fig. 7.11. Effect of particle volume fraction on heat flux in y -direction when $R_p = 10nm$.

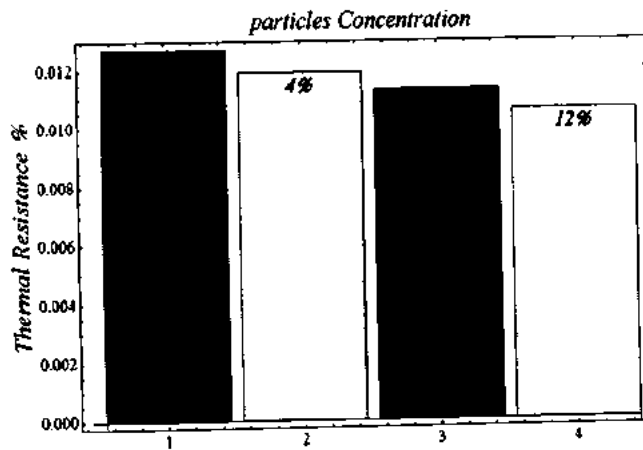


Fig. 7.12. Effect of particle volume fraction on thermal resistance when $R_p = 10nm$.

7.4 Conclusions

In this chapter, mixed convection heat transfer flow of power law nanofluid over stretching plate is investigated. The effects of nanoparticle on velocity, temperature, shear stress, heat flux and thermal resistance polymer solution with different concentration of PVC are analyzed. It is found that the velocity of shear thinning fluid decline when particle volume concentration, PVC mass concentration and size of particle rise. It is seen that the shear stress is increased due to increasing of volume concentration. It is observed that the temperature and heat flux of shear thinning fluid enlarged by enhancement of particle volume concentration and also improvement found in temperature with small size of particle.

Under the Boussinesq approximation, the governing equations can be written as

$$\frac{\partial u}{\partial x} + \frac{\partial v}{\partial y} = 0, \quad (8.1)$$

$$\rho_{nf} \left(u \frac{\partial u}{\partial x} + v \frac{\partial u}{\partial y} \right) = \mu_{nf} \frac{\partial^2 u}{\partial y^2} + (\rho\beta)_{nf} g (T - T_\infty), \quad (8.2)$$

$$(\rho C_p)_{nf} \left(u \frac{\partial T}{\partial x} + v \frac{\partial T}{\partial y} \right) = k_{nf} \frac{\partial^2 T}{\partial y^2}. \quad (8.3)$$

The subject to the following boundary condition are

$$\left. \begin{aligned} u(x,0) = u_w = U_w x^n, \quad v(x,0) = v_w(x), \\ T(x,0) - T_w = T_w - T(x,0) = Cx^n \\ u(x,\infty) = 0, \quad T(x,\infty) = T_\infty \end{aligned} \right\} \quad (8.4)$$

In view of Eqs. (8.2) and (8.3), the models of physical properties are defined in Eqs. (1.3), (1.7), (1.8), (1.11) and (1.18). The values of parameters that are involved in thermal conductive and viscosity models are shown in table 8.1.

Table 8.1. The value of parameters for thermal conductive and viscosity models.

Nanoparticles Shape	Sphericity (Ψ)	Shape Factor (n^*)	A_1	A_2
Needle	0.62	4.9	13.5	904.4
Disk	0.36	8.6	14.6	123.3
Sphere	1	3	2.5	6.2

The physical properties of the base fluid and particles are shown table 8.2.

Table 8.2. Physical properties of base fluid and particles for nanofluid.

Physical properties	HFE-7100	HFE-7200	HFE-7500	Nimonic 80a
$\rho (kgm^{-3})$	1510	1430	1610	8190
$C_p (J/kg-k)$	1180	1220	1130	448
$\beta (1/K)$	0.0018	0.0016	0.0013	0.00013
$k (W/m-K)$	0.0678	0.07	0.65	112

Using the similarity and dimensionless variables Eq. (6.4) and substitute into Eqs. (8.1) to (8.4) and get the non-dimensional Eqs. (8.5) to (8.7) which are expressed as

follows

$$\frac{\rho_{nf}}{\rho_f} \left\{ m f'^2 - \left(\frac{m+1}{2} \right) f f'' \right\} = \frac{\mu_{nf}}{\mu_f} \left(\frac{m+1}{2} \right) f'' + \frac{\lambda}{m+1} \theta, \quad (8.5)$$

$$\text{Pr} \frac{(\rho C_p)_{nf}}{(\rho C_p)_f} \left\{ n f' \theta - \left(\frac{m+1}{2} \right) f \theta' \right\} = \frac{k_{nf}}{k_f} \left(\frac{m+1}{2} \right) \theta''. \quad (8.6)$$

The corresponding boundary conditions are given by

$$\left. \begin{aligned} f'(0) = 1, f(0) = f_w, f(\infty) = 0 \\ \theta(0) = 1, \theta(\infty) = 0 \end{aligned} \right\}. \quad (8.7)$$

where $f_w = -v_w \sqrt{\frac{x^{1-m}}{\nu U_o}} \sqrt{\frac{2}{m+1}}$ is the porosity parameter (suction or injection),

$\text{Re}_x = \frac{U_o x^{m+1}}{\nu_f}$ is local Reynolds number, $\text{Gr}_x = \frac{g \beta_f C x^{n+3}}{\nu_f^2}$ is the local Grashof

number and $\lambda = \frac{\text{Gr}_x}{\text{Re}_x^2}$ is the mixed convection parameter.

The wall shear stress which is known as the Skin friction coefficient can be written as

$$C_f = \frac{2\tau_w}{\rho u_w^2}, \quad (8.8)$$

where

$$\tau_w = \mu_{nf} \left(\frac{\partial u}{\partial y} \right)_{y=0}. \quad (8.9)$$

The local Nusselt number which is known as heat transfer rate can be written as

$$Nu = \frac{x q_w}{k_f C x^n}, \quad (8.10)$$

where

$$q_w = -k_{nf} \left(\frac{\partial T}{\partial y} \right)_{y=0}. \quad (8.11)$$

The Skin friction and Nusselt number reduce to the following dimensionless forms

$$\text{Re}_x^{1/2} C_f = 2 \sqrt{\frac{m+1}{2}} \left(\frac{\mu_{nf}}{\mu_f} \right) f''(0), \quad (8.12)$$

$$\text{Re}_x^{-1/2} Nu = -\frac{k_{nf}}{k_f} \sqrt{\frac{m+1}{2}} \theta'(0). \quad (8.13)$$

8.2 Solution of the problem

Here, we will give the analytic solutions by means of BVP4c 2.0 package. The BVP4c 2.0 requires to put the governing equations along with corresponding boundary conditions, auxiliary linear operators and initial guess. Thus choose the auxiliary linear operators corresponding to the Eqs. (8.5) and (8.6) as

$$\mathcal{L}_1(f) = \frac{d^3 f}{d\eta^3} - \frac{df}{d\eta}, \quad \mathcal{L}_2(\theta) = \frac{d^2 \theta}{d\eta^2} - \theta. \quad (8.14)$$

Considering the boundary conditions in Eq. (8.7), we respectively choose the following initial approximation for variable wall temperature

$$f_0(\eta) = 1 + f_w - e^{-\eta}, \quad \theta_0(\eta) = e^{-\eta}. \quad (8.15)$$

Using the linear auxiliary operators in Eq. (8.14) and the initial approximations in Eq. (8.15), the coupled nonlinear Eqs. (8.5) and (8.6) subject to the boundary conditions (8.7) can be solved directly via BVP4c 2.0 package. Get the results for velocity profile, temperature profile, sink friction and Nusselt numbers for different non-dimensional numbers at 30th iterations of package. The solution of f and θ at first iteration is given by

$$\begin{aligned} f = & 1 + \frac{11C_1}{240} - \frac{11C_2}{480} + \frac{11C_1 m}{240} - \frac{11C_2 m}{160} + e^{-3\eta} \left(\frac{11C_1}{960} - \frac{11C_2 m}{960} \right) + f_w - \frac{11C_2 f_w}{240} \\ & - \frac{11C_2 m f_w}{240} + \left(\frac{11C_1}{240} - \frac{11C_2}{240} + \frac{11C_1 m}{240} \right) e^{-2\eta} + \frac{11C_3 \lambda}{75} + \frac{22}{75} C_3 e^{-3\eta/2} \lambda \\ & + \left(-1 - \frac{11C_1}{120} + \frac{11C_2}{192} - \frac{11C_1 m}{120} + \frac{121C_2 m}{960} + \frac{11C_2 f_w}{120} + \frac{11C_2 m f_w}{120} - \frac{11C_3 \lambda}{25} \right) e^{-\eta} \\ \theta = & e^{-\eta/2} + \left(-\frac{169C_4}{420} - \frac{169C_5 m}{420} + \frac{169C_5 n}{105} \right) e^{-5\eta/2} \\ & + \left(-\frac{676C_5}{525} - \frac{676C_5 m}{525} - \frac{169C_5 n}{105} + \frac{169C_4}{200 \text{Pr}} + \frac{169C_4 m}{200 \text{Pr}} - \frac{169C_5 f_w}{100} - \frac{169C_5 m f_w}{100} \right) e^{-\eta} \\ & + \left(\frac{169C_5}{100} + \frac{169C_5 m}{100} - \frac{169C_4}{200 \text{Pr}} - \frac{169C_4 m}{200 \text{Pr}} + \frac{169C_5 f_w}{100} + \frac{169C_5 m f_w}{100} \right) e^{-3\eta/2} \end{aligned} \quad (8.18)$$

8.3 Results and discussion

In this section, the behavior of developing parameters in the expressions of velocity and temperature distributions are examined through Figs. 8.1 to 8.10 with HEF-7100

based nanofluids contained Nimonic 80a nanoparticles. The governing equations along boundary conditions are transferred into ordinary differential equations. These equations include the nanoparticles volume fraction ϕ , mixed convection parameter λ , suction or injection parameter f_w and temperature power index n and stretching power index m . In this study, for velocity and temperature profile, we prepare the particles of different shapes by applying the Eq. (1.18). We take sphere shape particle of $5nm$ radius, needle shape of $5nm$ radius and $250nm$ length and disk shape of $250nm$ radius and thickness of $5nm$. In the thermal conductive model, chose $a = b = c = 5$ for sphere shape, $a = 250, b = c = 5$, for needle shape particle and $a = b = 250, c = 5$ for disk particle. It also consider nanolayer thickness $2nm$ of base fluid on particle and for this take the value $t_1 = 24$. The thermal conductive of nanolayer k_f is considered $2k_f$.

Figs. 8.1 and 8.2 illustrate the volume fraction effect on velocity and temperature of the fluid. These Figs. are prepare within range of particle volume fraction $2\% \leq \phi \leq 6\%$. In Fig. 8.1, the momentum boundary layer thickness and velocity of fluid is increased when volume fraction is increased. It is also observe that the maximum velocity decrease is caused by sphere, followed by disk and needle shape particles respectively. In Fig. 8.2, the thermal boundary layer thickness and temperature of fluid increase by increasing particle volume fraction. It is noticed that the maximum temperature of nanofluid increase is caused by disk, followed by sphere and needle shape particles respectively. Figs. 8.3 and 8.4 show the behavior of non-dimensional mixed convection parameters on velocity and temperature profile of nanofluid. It is examined in Figs. 8.3 and 8.4, momentum and thermal boundary layer thickness is enhanced and decline respectively with the enhancement in the influence of mixed convection parameter. These Figs. also point out that velocity and temperature is increase and decrease by raising the value of mixed convection parameter. The effect of suction or injection parameter on velocity and temperature has been plotted in Figs. 8.5 and 8.6. In Fig. 8.5, the result demonstrates the enhancement in velocity distribution in flow region by decreasing the value of f_w . In these figure, It is observe that the momentum boundary layer thickness is maximum obtain in case of injection than section. It is also examined, particles of different shape in both section and injection cases have different behavior for velocity profile. In injection case, we see that maximum velocity is obtained by sphere particles.

Moreover, in case of section, due to needle shape nanoparticle maximum velocity is realized. In Fig. 8.6, it is noted that the temperature and thermal boundary layer is reduced when the value of f_w is enlarge. The given nanoparticles of three different shapes change the behavior in section and injection cases for temperature profile. In case of injection and section, the needle shape and disk shape nanoparticles give the maximum temperature respectively. Figs. 8.7 and 8.8 illustrate the effect of stretching power index on the non-dimensional velocity and temperature in presence of sphere and non-sphere nanoparticles. As it is seen, when stretching power index number m is increases, the velocity profile and momentum boundary layer thickness is decreased. On the other hand, the temperature of nanofluid and thermal boundary layer is enhanced with increment in the value of m . It is also realized that the maximum momentum boundary layer thickness is caused by needle shape nanoparticles as compare to other particle's shape. The maximum and minimum thermal boundary layer thickness is basis by disk and needle shape particle respectively. Figs. 8.9 and 8.10 indicate the influence of temperature power index on velocity and temperature profile with the present of shape effect. In these Figs., the effect of increasing value of n is to decrease velocity as well as temperature profiles for all shapes of nanoparticles. Additionally, the thickness of momentum and thermal boundary layer is decrease in the consequence of temperature power index n rising.

The numerical results in tables 8.3 to 8.7 illustrate the consequences of different parameters on the Skin friction coefficient and heat transfer rate of spherical and non-spherical nanoparticles suspended in *HEF-7100* fluid. These tables are repaired by fixing the parameters $\phi = 0.03$, $\lambda = 1$, $f_w = 0.5$, $m = 0.5$ and $n = 1$. The effect of particle volume fraction on the local Skin friction coefficients and local Nusselt number is shown in table 8.3. Table 8.3 depicts that with the increasing of nanoparticle volume fraction, local Skin friction coefficient and heat transfer rate is decreases and increase respectively. The maximum wall shear stress causes by needle shape particle. The maximum heat transfer rate is due to disk shape particle. In addition, the heat transfer rate of *HEF-7100* based nanofluid is improve 19%, 25% and 10% corresponding to needle shape, disk shape and sphere shape particle in that order at 6% particle volume fraction. The effect of particle's size on Skin friction coefficient and heat transfer is shown in table 8.4 to 8.6. In this table, we also analysis that local Skin friction as well as local Nusselt number is decrease with the

enhancement in length and radius of needle shape, radius and thickness of disk shape and radius of sphere shape particles. It also examines that small size particles are more effective for heat transfer rate as compare to large size particle. For example, when take sphere particle, the heat transfer rate is improved 4.89% and 4.42% corresponding to radius of 5nm and 30nm respectively. To investigate wall shear stress and heat transfer rate, examined the three different Novec based fluids in table 8.7. It is seen that the effect of wall shear stress reduce by *HFE-7200* fluid than other and heat transfer rate is enhance by *HFE-7500* fluid as compare to other Novec fluids.

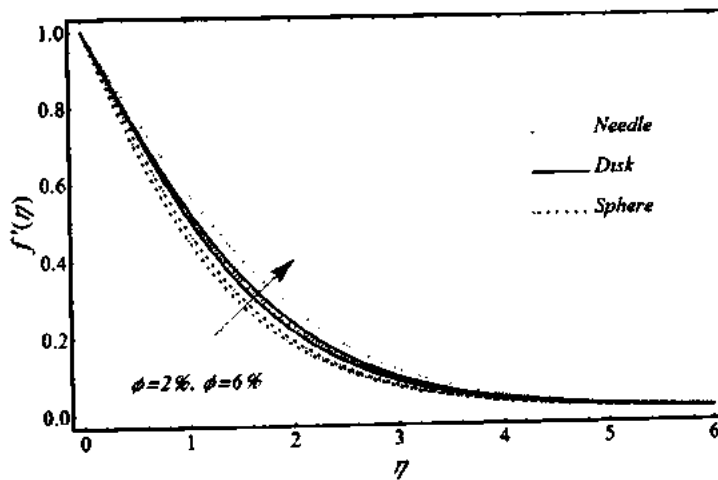


Fig. 8.1. Effect of volume fraction on velocity profile when $\lambda = 1$, $f_w = 0.5$, $m = 0.5$ and $n = 1$.

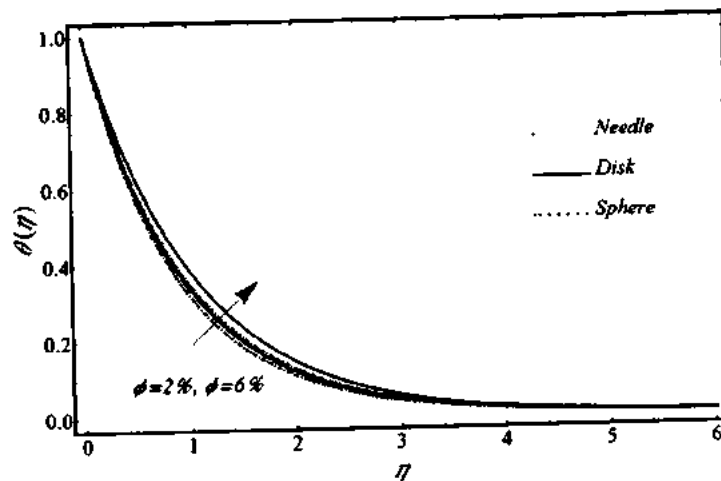


Fig. 8.2. Effect of volume fraction on temperature profile $\lambda = 1$, $f_w = 0.5$, $m = 0.5$ and $n = 1$.

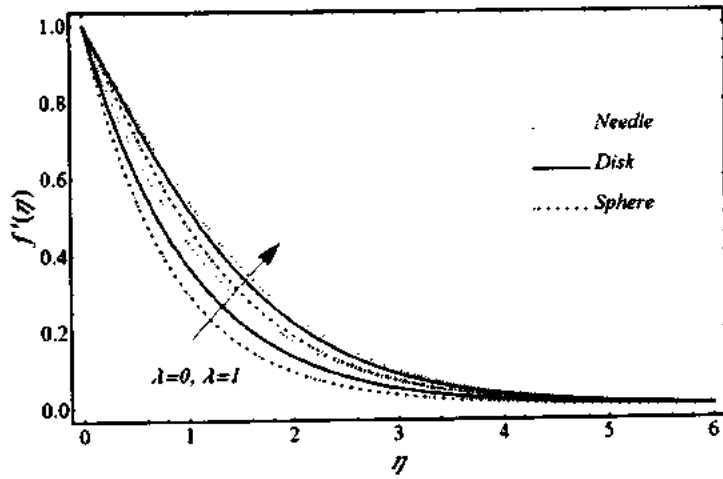


Fig. 8.3. Effect of convection parameter on velocity profile when $\phi = 3\%$, $f_w = .5$, $m = .5$ and $n = 1$.

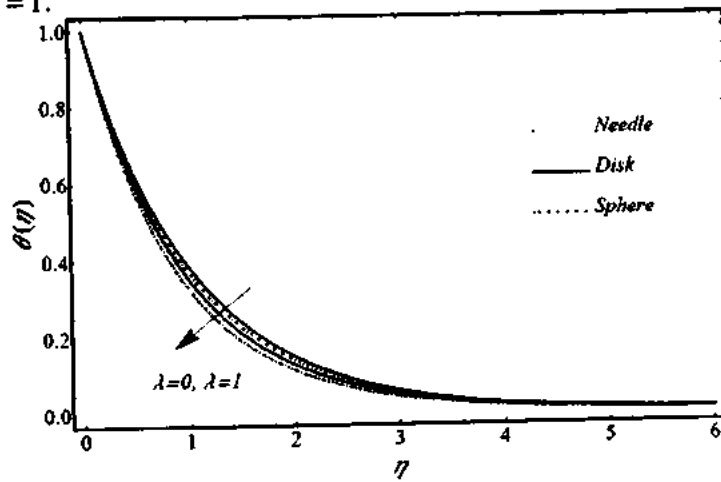


Fig. 8.4. Effect of convection parameter on temperature when $\phi = 3\%$, $f_w = .5$, $m = .5$ and $n = 1$.

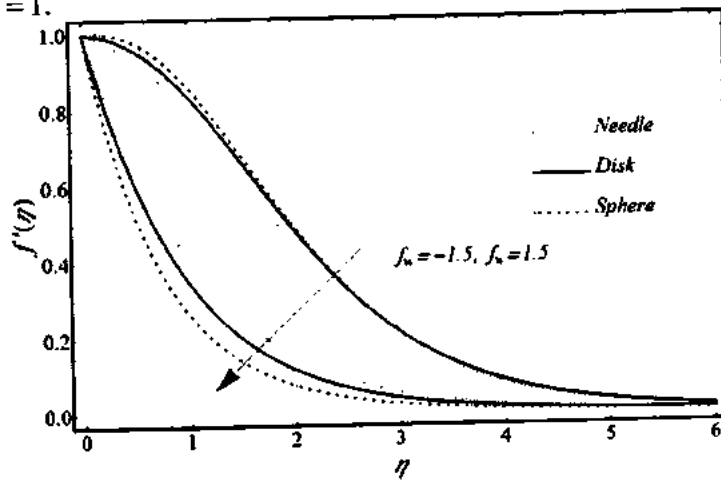


Fig. 8.5. Effect of suction or injection parameter on velocity profile when $\phi = 3\%$, $\lambda = 1$, $m = .5$ and $n = 1$.

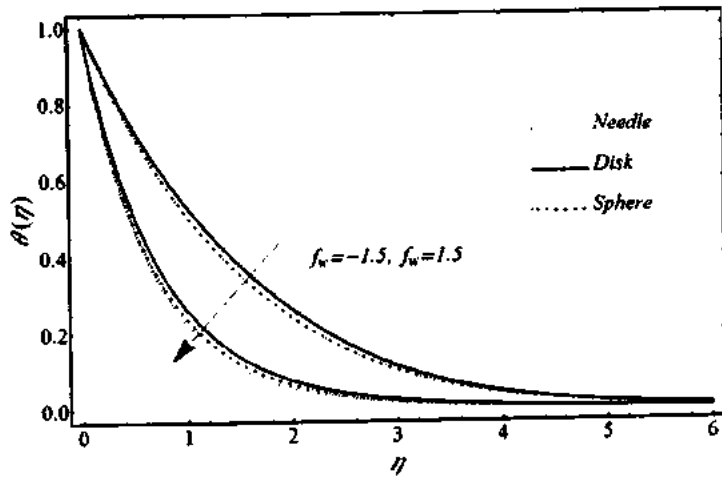


Fig. 8.6. Effect of suction or injection parameter on temperature profile when $\phi = 3\%$, $\lambda = 1$, $m = .5$ and $n = 1$.

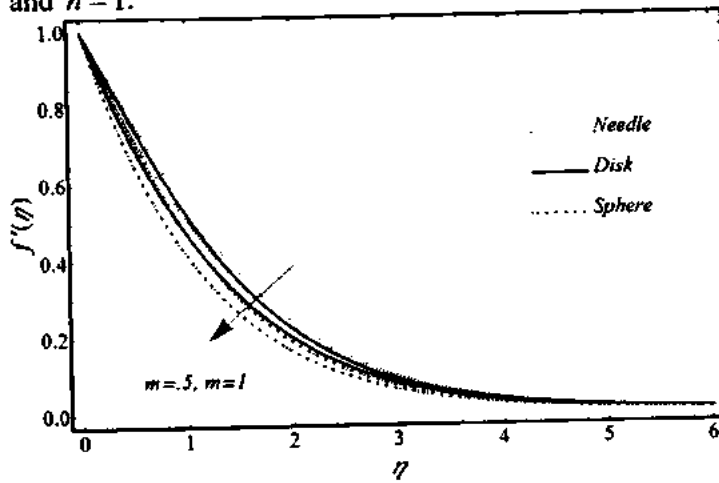


Fig. 8.7. Effect of stretching power index on velocity profile when $\phi = 3\%$, $\lambda = 1$, $f_w = 0.5$ and $n = 1$.

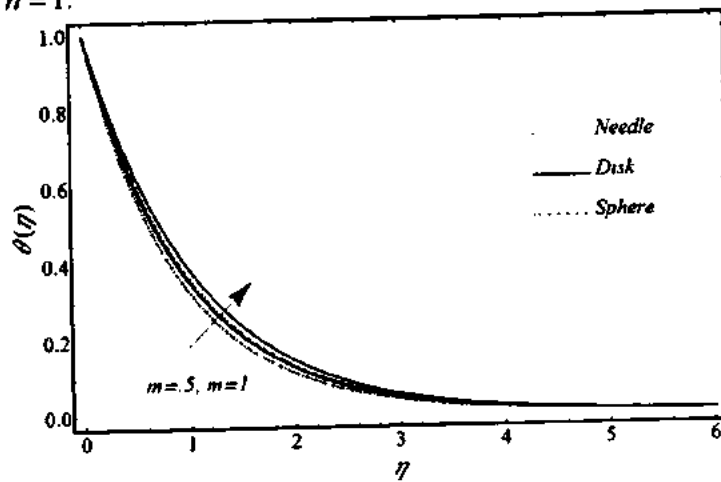


Fig. 8.8. Effect of stretching power index on temperature profile when $\phi = 3\%$, $\lambda = 1$, $f_w = 0.5$ and $n = 1$.

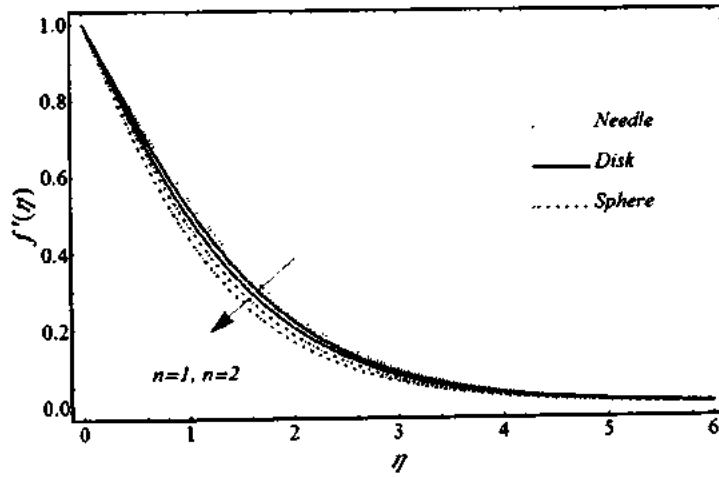


Fig. 8.9. Effect of temperature index on velocity profile $\phi = 3\%$, $\lambda = 1$, $f_w = 0.5$ and $m = 0.5$.

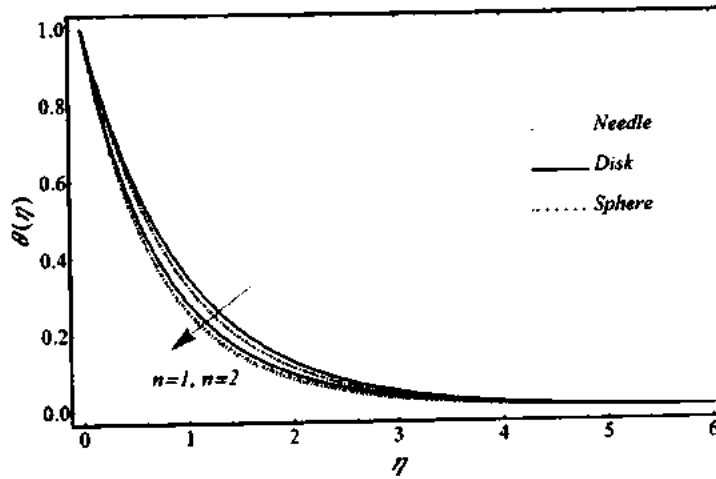


Fig. 8.10. Effect of temperature index on temperature profile when $\phi = 3\%$, $\lambda = 1$, $f_w = 0.5$ and $m = 0.5$.

Table 8.3. Effect of volume fraction on Skin-friction coefficient and Nusselt number.

	ϕ	Needle	Disk	Sphere
$C_f Re_x^{1/2}$	2%	-1.3618	-1.1526	-1.0117
	4%	-2.2217	-1.4943	-1.1581
	6%	-3.4084	-1.8971	-1.3088
$Nu Re_x^{-1/2}$	2%	1.1161	1.1334	1.0791
	4%	1.1950	1.2213	1.1137
	6%	1.2478	1.3090	1.1494

Table 8.4. Effect of dimension of Needle on Skin-friction coefficient and Nusselt number.

	Dimension	Needle
$C_f Re_x^{1/2}$	$a = 250, b = c = 5$	-1.7504
	$a = 500, b = c = 15$	-1.7594
	$a = 1000, b = c = 30$	-1.7613
$Nu Re_x^{-1/2}$	$a = 250, b = c = 5$	1.1468
	$a = 500, b = c = 15$	1.1438
	$a = 1000, b = c = 30$	1.1423

Table 8.5. Effect of dimension of disk on Skin-friction coefficient and Nusselt number.

	Dimension	Disk
$C_f Re_x^{1/2}$	$a = b = 5, c = 250$	-1.3162
	$a = b = 15, c = 500$	-1.3262
	$a = b = 30, c = 1000$	-1.3266
$Nu Re_x^{-1/2}$	$a = b = 5, c = 250$	1.1774
	$a = b = 15, c = 500$	1.1687
	$a = b = 30, c = 1000$	1.1683

Table 8.6. Effect of dimension of sphere on Skin-friction coefficient and Nusselt number.

	Dimension	Sphere
$C_f Re_x^{1/2}$	$a = b = c = 5$	-1.0845
	$a = b = c = 15$	-1.0846
	$a = b = c = 30$	-1.0914
$Nu Re_x^{-1/2}$	$a = b = c = 5$	1.0963
	$a = b = c = 15$	1.0941
	$a = b = c = 30$	1.0914

Table 8.7. The values of Skin-friction coefficient and Nusselt number for different base fluids.

	Base Fluids	Needle	Disk	Sphere
$C_f Re_x^{1/2}$	HFE-7100	-1.7504	-1.3162	-1.0845
	HFE-7200	-1.7645	-1.3291	-1.0960
	HFE-7500	-1.7340	-1.3013	-1.0712
$Nu Re_x^{-1/2}$	HFE-7100	1.15592	1.7745	1.0963
	HFE-7200	1.15590	1.1773	1.0961
	HFE-7500	1.15591	1.1777	1.0966

8.4 Conclusions

In this chapter, the shape effect with nanolayer effect on *HFE-7100* based nanofluid with influence of different parameters is analyzed. It is seen that the velocity of nanofluid decrease by increasing value of temperature power index n , stretching power index m and suction (or injection) parameter f_w . On the hand, velocity profile increases by increasing the values of mixed convection λ and particle volume fraction ϕ . The temperature of nanofluid increases by increasing the volume fraction and stretching parameter. Moreover, temperature is decreased due to enhancement in the effect of mixed convection parameter, suction (or injection) parameter and temperature power index. The lowest velocity and highest temperature of nanofluid are caused by sphere and disk shape particles respectively.

Chapter 9

A study of Fe_3O_4 nanoparticles aggregation in engine oil base nanofluid over vertical stretching permeable sheet in mixed convection

In this chapter investigate the effects of aggregations in two-dimensional heat transfer mixed convection flow of a nanofluid near a vertical stretching permeable sheet when the buoyancy force opposes or assists the flow. The engine oil having Fe_3O_4 metal nanoparticles is considered as a base fluid. The variable wall temperature and magnetohydrodynamic (MHD) with interfacial layer are also taken into account. The said model is not yet extensively investigated. In particular, when aggregate is embedded within a sphere and is composed of a few approximately linear chains, which span the whole aggregate and side chains. The work undertaken is a blend of numerical and analytical studies under the assumption of Boussinesq approximation. The resulting nonlinear governing equations with associated boundary conditions are solved using homotopy analysis method. The effects of aggregation parameters on velocity and temperature for essential physical parameters are demonstrated in the form of graphs whereas the tabular results are displayed to see the effects of chemical dimensions, radius of gyration, volume fraction and fractal dimensions. The correlation of Skin friction and Nusselt number are computed and examined.

9.1 Mathematical formulation of the problem

Consider mixed convection boundary layer flow of nanofluid over vertically upward stretching permeable sheet. The formulation of stretching sheet is shown in Fig. 8.1. Take the engine oil as a base fluid with Fe_3O_4 metal nanoparticles for nanofluid. It is also suppose that the temperature is the power function of the distance. Under the Boussinesq approximation, the governing equations can be written as

$$\frac{\partial u}{\partial x} + \frac{\partial v}{\partial y} = 0, \quad (9.1)$$

and non-percolation contributing dead-end particles are defined in Eqs. (1.25) and (1.26). Following the definition of the fractal dimension d_f , the number of particles in the aggregation is given by

$$N_{int} = (R_g / R_p)^{d_f}, \quad (9.13)$$

where R_p is the radius of the primary particle and R_g is average radius of gyration.

The number of particles belonging to backbone N_c is defined by the chemical dimension is given by

$$N_c = (R_g / R_p)^{d_l}, \quad (9.13)$$

where d_l ranges between one and d_f . When $d_l = d_f$ all of the particles belong to the backbone and there are no dead ends.

In order to solve the governing Eqs. (9.1) to (9.3), introduce the following similarity variables

$$\left. \begin{aligned} \eta = \frac{y}{x} \sqrt{\frac{m+1}{2}} \sqrt{\text{Re}_x}, \quad T - T_\infty = Cx^n \theta(\eta) \quad u = U_o x^m f'(\eta), \\ v = -\sqrt{\frac{2\nu U_o}{m+1}} x^{\frac{m-1}{2}} \left(\frac{m+1}{2} f + \frac{m-1}{2} \eta f' \right) \end{aligned} \right\}. \quad (9.14)$$

Substituting Eq. (9.14) into Eqs. (9.1) to (9.3), obtain the following ordinary differential in non-dimensional form

$$\frac{\rho_{nf}}{\rho_f} \left\{ m f'^2 - \left(\frac{m+1}{2} \right) f f'' \right\} = \frac{\mu_{nf}}{\mu_f} \left(\frac{m+1}{2} \right) f'' + \lambda \frac{(\rho\beta)_{nf}}{(\rho\beta)_f} \theta - M_2 f', \quad (9.15)$$

$$\text{Pr} \frac{(\rho C_p)_{nf}}{(\rho C_p)_f} \left\{ n f' \theta - \left(\frac{m+1}{2} \right) f \theta' \right\} = \frac{k_{nf}}{k_f} \left(\frac{m+1}{2} \right) \theta'' + \text{Pr} Ec M_2 f'^2 \quad (9.16)$$

along with the boundary conditions

$$\left. \begin{aligned} f'(0) = 1, \quad f(0) = f_w, \quad f(\infty) = 0 \\ \theta(0) = 1, \quad \theta(\infty) = 0, \end{aligned} \right\}, \quad (9.17)$$

where $M_2 = \frac{\sigma \beta_o^2 x^{1-m}}{\rho_f U_o}$ is magnetic parameter.

The Skin friction and Nusselt number in dimensionless form are given in Eqs. (9.12) and (9.13)

9.2 Solution of the problem

Here, in this section we will provide the analytical and uniformly valid solutions by using BVP4c 2.0 package. For the BVP4c 2.0, requires to put the governing equations along corresponding boundary conditions, initial guess and auxiliary linear operators. Therefore, take the initial guess and auxiliary linear operators for the desire solutions as follow

$$f_0 = 1 + f_w - e^{-\eta}, \quad \theta_0 = e^{-\eta}, \quad (9.18)$$

$$\mathcal{L}_1(f) = \frac{d}{d\eta} \left(\frac{d^2}{d\eta^2} - 1 \right) f, \quad \mathcal{L}_2(\theta) = \left(\frac{d^2}{d\eta^2} - 1 \right) \theta. \quad (9.19)$$

By means of the this package, get the results for velocity, temperature distribution; sink friction and Nusselt numbers for different non-dimensional numbers at 30th iterations. The solution for velocity and temperature at first iteration is given as

$$\begin{aligned} f' = & \left(1 + \frac{11C_1}{120} - \frac{11C_2}{192} + \frac{11C_1m}{120} - \frac{121C_2m}{960} - \frac{11M_2}{60} - \frac{11C_2s}{120} - \frac{11C_2mf_w}{120} + \frac{11C_3\lambda}{25} \right) e^{-\eta} \\ & + \left(-\frac{11C_1}{120} + \frac{11C_2}{120} - \frac{11C_1m}{120} + \frac{11C_2m}{120} + \frac{11M_2}{60} + \frac{11C_2f_w}{120} + \frac{11C_2mf_w}{120} \right) e^{-2\eta} \\ & + \left(-\frac{11C_2}{320} + \frac{11C_2m}{320} \right) e^{-3\eta} - \frac{11}{25} C_3 e^{-3\eta/2} \lambda \end{aligned} \quad (9.20)$$

$$\begin{aligned} \theta = & e^{-\eta/2} - \frac{169}{160} EcM_2 e^{-3\eta} + \left(-\frac{169C_5}{420} - \frac{169C_5m}{420} + \frac{169C_5n}{105} \right) e^{-5\eta/2} \\ & + \left(-\frac{676C_5}{525} - \frac{676C_5m}{525} + \frac{169EcM_2}{160} - \frac{169C_5n}{105} + \frac{169C_4}{200Pr} + \frac{169C_4m}{200Pr} - \frac{169C_5f_w}{100} - \frac{169C_5mf_w}{100(9.2)} \right) e^{-\eta} \\ & + \left(\frac{169C_5}{100} + \frac{169C_5m}{100} - \frac{169C_4}{200Pr} - \frac{169C_4m}{200Pr} + \frac{169C_5f_w}{100} + \frac{169C_5mf_w}{100} \right) e^{-3\eta/2} \end{aligned}$$

9.3 Results and discussion

In this section, the behavior of emerging parameters intricated in the governing equations are examined through Figs. 9.1 to 9.6 with Engine oil based nanofluids contained Fe_3O_4 nanoparticles. In this study, for velocity and temperature profile, we keep fixed the value of $\lambda = 0.1$, $M_2 = 0.5$, $Ec = 0.01$, $f_w = -0.5$, $n = 1$, $m = 2$, $Pr = 132$ and see the effect of radius of gyration R_g , the fractal dimensions d_f and chemical dimensions d_c . We also consider sphere shape particles of 10nm radius.

Figs. 9.1 and 9.2 illustrate the fractal dimension effect on velocity and temperature of the nanofluid. For preparing these figures, consider the radius of gyration is 150 nm and there are 50 particles belong to backbone in single aggregation. In single aggregation, when consider the total particles are 100, 200 and 300, get the values of fractal dimensions 1.70, 1.95 and 2.10 respectively. Fig. 9.1 point out that velocity is decrease when effect of fractal dimensions is increase. It means that the velocity of nanofluid will slow down when number of particles in aggregations are increase. Fig. 9.1 also point out that velocity is decreased by increasing the volume fraction of nanoparticles. In Fig. 9.2, temperature of nanofluid is decrease when effect of fractal dimensions is increased. It is because of that when dead end particles are increase, temperature of nanofluid is decreased. In addition, temperature of nanofluid is increase with raising the volume fraction of nanoparticles. Figs. 9.3 and 9.4 indicate the influence of chemical dimension on velocity and temperature profile respectively. For preparing these figures, we take total 200 particles in an aggregation which are spread in 150 nm diameter. The values 1.45, 1.70 and 1.85 of chemical dimension are taken by considering 50, 100 and 150 particles in backbone respectively. The velocity profile of nanofluid is declined by decreasing the value of chemical dimension shown in Fig. 9.3. The temperature profile of nanofluid is increased by increasing the influence of chemical dimension shown in Fig. 9.4. It means when number of particles are increase in backbone, temperature is increased. The effects of radius of gyration on the velocity and the temperature have been plotted in Figs. 9.5 and 9.6. These Figs. are prepared by considering the 200 particles in an aggregation and each aggregation contain 150 dead ends particles and 50 nanoparticles belong to backbone. The results demonstrate the enhancement in velocity distribution in flow region by increasing the radius of gyration shown in Fig. 9.5. In Fig. 9.6, it is noticed that the temperature of nanofluid is increased when radius of gyration is increased. Its mean, temperature is increased, if particles belong to backbone are spread in large radius as compare to particles in small radius.

The numerically results in the tables 9.1 to 9.4 illustrate the effects of radius of gyration R_g , the fractal dimensions d_f and chemical dimensions d_c on Skin friction coefficient and heat transfer rate of spherical nanoparticles spend in Engine oil fluid. These tables are repaired by fixing the $\lambda = 0.1$, $M = 0.5$, $Ec = 0.01$, $f_w = -0.5$, $n = 1$, $m = 2$, $Pr = 132$. The effect of particle volume fraction on the local Skin friction

coefficients and local Nusselt number is shown in table 9.1. Table 9.1 depicts that with the increase in volume fraction of nanoparticles suspension in the base fluid, local Skin friction coefficient and heat transfer rate is increased and decreased respectively. In this table, when we choose 5% and 10% mass concentration of Fe_3O_4 nanoparticles, the heat transfer rate of base fluid is rise 23.46% and 33.76% respectively. The investigation of fractal dimensions on wall shear stress and heat transfer rate is shown in table 9.2. In this table, we also analysis that local Skin friction as well as heat transfer rate is decreased with the enhancement in the value of fractal dimensions. This is due to fact that when number of dead ends particles is increased, the heat transfer rate is decreased. For example, when consider 50 dead ends particles and 50 backbone's nanoparticle in an aggregation, the heat transfer rate is 43.73%. On the other hand, when we take 150 dead ends particles and 50 backbone's nanoparticles in single aggregate the heat transfer rate is calculated 33.76%. Its means 11.97% heat transfer rate is decreased by increasing 100 dead ends particle in aggregation. Table 9.3 shows the effects of chemical dimensions on Skin friction and heat transfer rate. In this table, it is seen that the local Skin friction coefficient and heat transfer rate of nanofluid is enhanced by enhancement in the chemical dimensions. The reason of enhancement in heat transfer rate is due to increment of particle in backbone. Table 9.4 depicts the impact of aggregation radius on Skin friction and heat transfer rate. For preparing of table 9.4, we consider 200 dead ends particles and 50 backbone particles spread in single aggregation of different radius. Table 9.4 demonstrates that, by increasing the aggregation radius, local Skin friction coefficient and heat transfer rate of nanofluid is increased. It is observed that when connectivity of particles in backbone is spread in large radius, the heat transfer rate is much improves as compare to backbone in small radius.

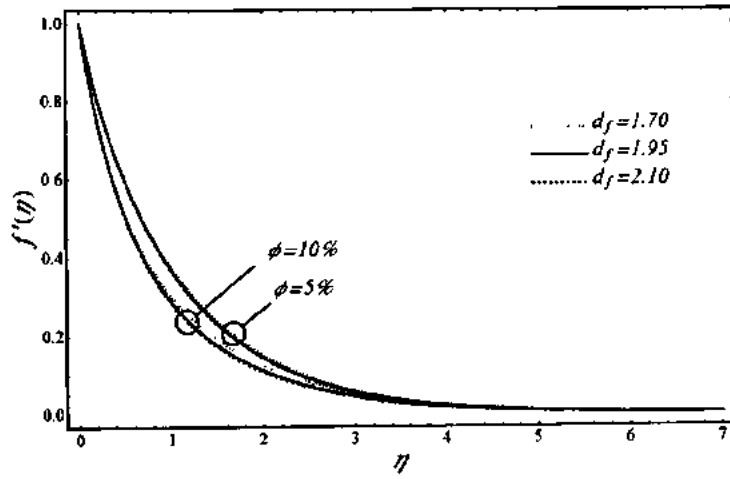


Fig. 9.1. Effect of fractal dimensions on velocity profile.

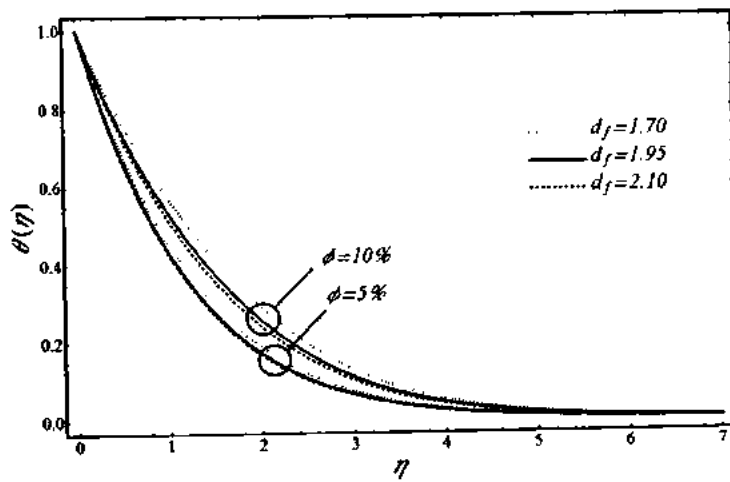


Fig. 9.2. Effect of fractal dimensions on temperature profile.

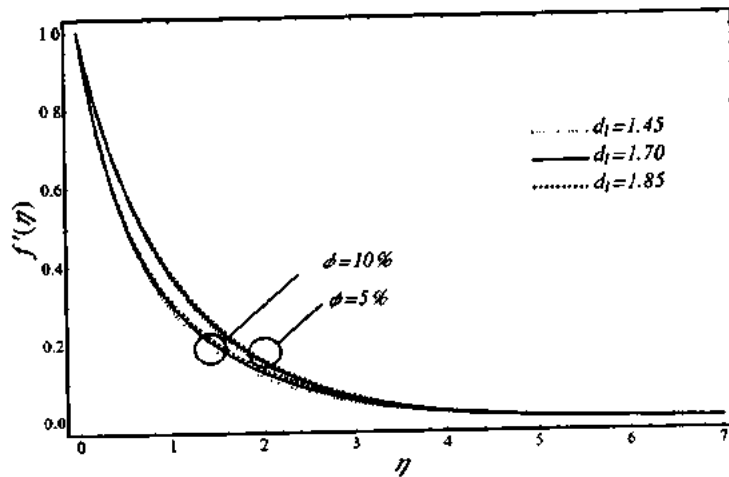


Fig. .9.3. Effect of chemical dimensions on velocity profile.

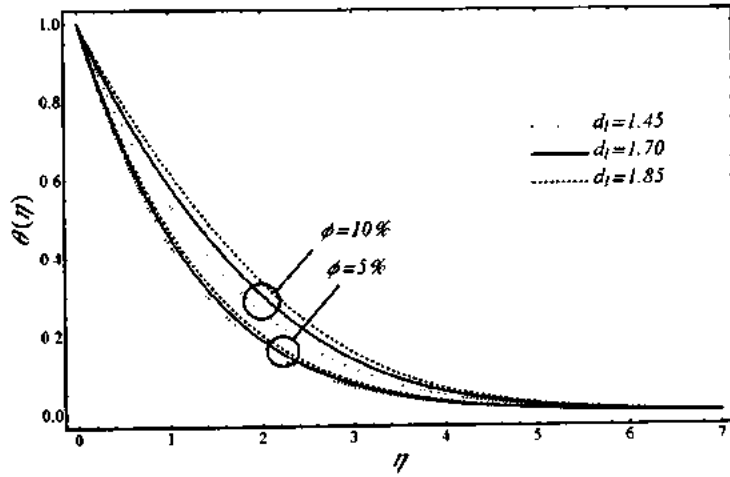


Fig. 9.4. Effect of chemical dimensions on temperature profile.

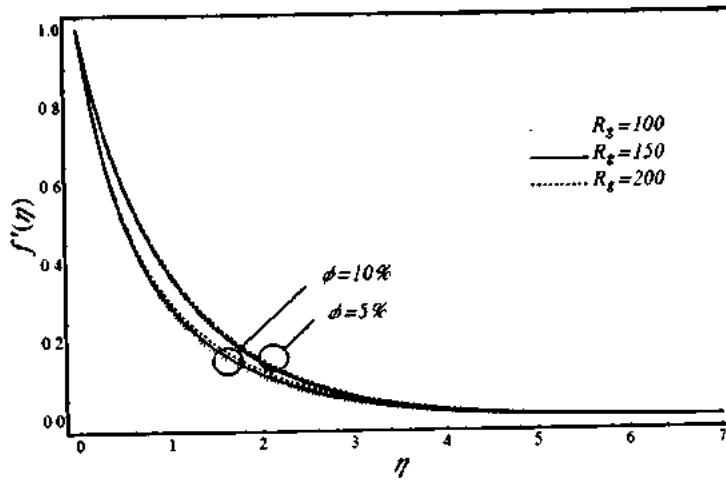


Fig. 9.5. Effect of radius of gyration on velocity profile.

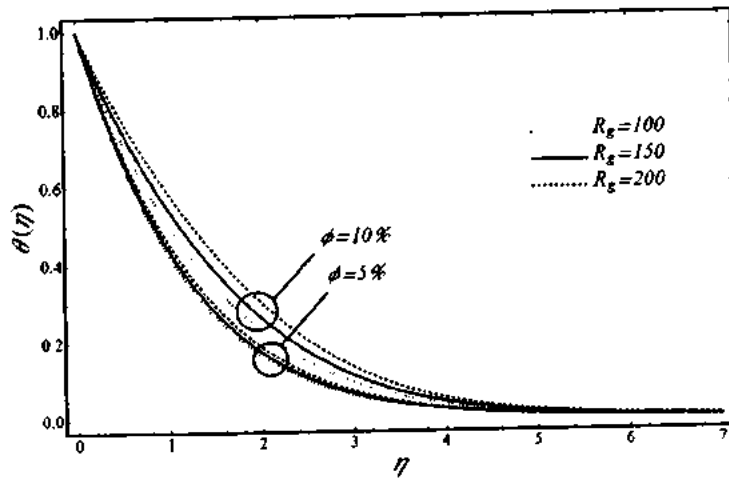


Fig. 9.6. Effect of radius of gyration on temperature profile.

Table 9.1. Effect of volume fraction on Skin-friction coefficient and Nusselt number.

ϕ	$Re_x^{-1/2} Nu$	$Re_x^{1/2} C_f$
0%	1.58318	-2.46824
5%	1.95467	-2.98641
10%	2.39011	-3.54109

Table 9.2. Effect of fractal dimension on Skin-friction coefficient and Nusselt number.

d_f	$Re_x^{-1/2} Nu$	$Re_x^{1/2} C_f$
1.70	2.91731	-3.54086
1.95	2.39011	-3.54109
2.10	2.23785	-3.54113

Table 9.3. Effect of chemical dimension on Skin-friction coefficient and Nusselt number.

d_i	$Re_x^{-1/2} Nu$	$Re_x^{1/2} C_f$
1.45	2.39011	-3.54109
1.70	2.84238	-3.54095
1.85	3.33543	-3.54081

Table 9.4. Effect of radius of gyration on Skin-friction coefficient and Nusselt number.

R_g	$Re_x^{-1/2} Nu$	$Re_x^{1/2} C_f$
100	2.15762	-3.54116
150	2.39011	-3.54109
200	2.64649	-3.54101

9.4 Conclusions

In this chapter, we have analyzed the aggregation effects on engine oil based nanofluid contained Fe_3O_4 nanoparticles with the influence of different parameters. It is found that the velocity of nanofluid decrease by increasing the particle volume fraction and fractal dimensions. On the hand, velocity increases by increasing the

chemical dimensions and radius of gyration. The temperature of nanofluid is increased by increasing the volume fraction, chemical dimensions and radius of gyration. Moreover, temperature decreases due to enhancement in the fractal dimensions. Some consequence for wall shear stress and heat transfer rate are obtained by numeric set of results. It is observed that the wall shear stress is declined by particle volume fraction and fractal dimensions. The behavior of heat transfer rate is enhanced by particle volume fraction, chemical dimensions and radius of gyration.

Chapter 10

Particle shape effects on marangoni convection boundary layer flow of a nanofluid

In this chapter, particle shape effects on marangoni convective flow of a nanofluid are investigated. The aqueous solutions of ethylene glycol are considered as base fluid. Spherical and non-spherical shapes of nanoparticles having different sizes with nano-layer effects for nanofluid are used. The work undertaken is a blend of numerical and analytical studies. The effects of nanoparticles volume fraction and similarity parameter on velocity and temperature are illustrated graphically. The tabular results are displayed to see the effects of nanoparticle shape, size and concentrations of ethylene glycol in water for heat transfer rate and interface velocity. Finally a comparison with the existing literature is also made.

10.1 Mathematical formulation of the problem

Consider two-dimensional steady laminar Marangoni boundary layer flow of aqueous solutions of ethylene glycol based on nanofluid containing different shapes of copper nanoparticles. The nano-layer effect of aqueous solutions of copper nanoparticles is also taken into account. The interface temperature is supposed to be a power-law function of distance x along the interface. Further, choose coordinate system x and y are respectively beside the interface S and normal to it as it is shown in Fig. 10.1.

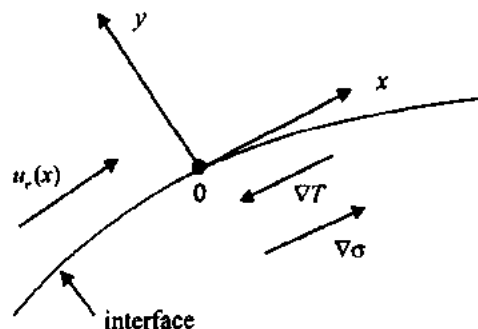


Fig. 10.1. Geometry for the Problem.

The steady boundary layer equations for a nanofluid can be written as

$$\frac{\partial u}{\partial x} + \frac{\partial v}{\partial y} = 0, \quad (10.1)$$

$$u \frac{\partial u}{\partial x} + v \frac{\partial u}{\partial y} = u_e \frac{\partial u_e}{\partial x} + \frac{\mu_{nf}}{\rho_{nf}} \frac{\partial^2 u}{\partial y^2}, \quad (10.2)$$

$$(\rho C_p)_{nf} \left(u \frac{\partial T}{\partial x} + v \frac{\partial T}{\partial y} \right) = k_{nf} \frac{\partial^2 T}{\partial y^2}, \quad (10.3)$$

subject to the boundary conditions

$$\begin{aligned} v = 0, \quad T = T_o(x), \quad \frac{\mu_{nf}}{\mu_f} \frac{\partial u}{\partial y} = \frac{\partial T}{\partial x} \quad \text{at } y = 0, \\ u = u_e(x), \quad T = T_e \quad \text{at } y \rightarrow \infty. \end{aligned} \quad (10.4)$$

In the above equations; $T_o(x)$ is the interface temperature distribution, T_e is the constant temperature of the external flow and $u_e(x)$ is the velocity of the external flow.

In the Eqs. (10.2) and (10.3), the models for physical properties are defined in Eqs. (1.3), (1.7), (1.8), (1.11) and (1.17). In the thermal conductivity and viscosity models, the values of empirical shape factor n^* , sphericity ψ , the constants A_1 and A_2 are shown in table 10.1.

Table 10.1. The value of parameters for thermal conductivity and viscosity models.

Nanoparticles Shape	Sphericity (ψ)	Shape Factor (m)	A_1	A_2
Needle	0.62	4.9	13.5	904.4
Disk	0.36	8.6	14.6	123.3
Sphere	1	3	2.5	6.2

Physical properties of base fluid and particles shown table 10.2.

Table 10.2. Physical properties of base fluid and particles for nanofluid.

Physical properties	30%	60%	90%	Cu
$\rho(kgm^{-3})$	1045.25	1086.27	1121.23	8933
$C_p(J/kg-k)$	3645	3084	2438	385
$k(W/m-K)$	0.453	0.349	0.276	400

The last condition of (10.4) signifies the Marangoni coupling condition at the interface. The surface tension σ is defined as (see Chamkha et al. [145])

$$\sigma = \sigma^o [1 - \gamma^*(T - T_e)], \quad (10.5)$$

here σ^o is the constant surface tension at origin and $\gamma^* = -(1/\sigma^o)\partial\sigma/\partial T > 0$ is the temperature coefficient of surface tension.

Now using the following transformations [146]

$$\begin{aligned} u(x, y) &= u_o x^{(2\alpha-1)/3} f'(\eta), \\ v(x, y) &= -\frac{1}{3} u_o \zeta_o x^{(\alpha-2)/3} [(2-\alpha)\eta f'(\eta) - (1+\alpha)f(\eta)], \\ T(x, y) &= T_e - h_o x^\alpha \theta(\eta), \quad \eta = x^{(\alpha-2)/3} y / \zeta, \end{aligned} \quad (10.6)$$

where u_o , h_o and ζ_o are constants. If choose $h_o = 1$ then u_o and ζ_o have the resulting unique values

$$u_o = \left(\frac{3}{1+\alpha}\right)^{1/3} \beta^{2/3}, \quad \zeta_o = \left(\frac{3}{1+\alpha}\right)^{1/3} \alpha^{-1/3}. \quad (10.7)$$

Substituting (10.7) into (10.1) to (10.3), get the resulting ordinary differential equations

$$\frac{\mu_{nf}}{\mu_f} \frac{\rho_f}{\rho_{nf}} f'''' + ff'' - \frac{2\alpha-1}{\alpha+1} (f'^2 - 1) = 0, \quad (10.8)$$

$$\frac{k_{nf}}{k_f} \theta'' + \frac{(\rho C_p)_{nf}}{(\rho C_p)_f} Pr \left(f\theta' - \frac{3\alpha}{\alpha+1} f'\theta \right) = 0 \quad (10.9)$$

and the boundary conditions (10.4) become

$$\begin{aligned} f(0) &= 0, & \frac{\mu_{nf}}{\mu_f} f''(0) &= -1, & g(0) &= 1, \\ f'(\infty) &= 1, & g(\infty) &= 0. \end{aligned} \quad (10.10)$$

Now determine the dimensional temperature and the temperature gradient normal to the interface as

$$T(x, y) = T_e - h_o x^\alpha g(\eta, \phi, Pr, \alpha), \quad (10.11)$$

$$\left(\frac{\partial T}{\partial y} \right)_{y=0} = -(h_o / \xi_o) x^{2(2\alpha-1)/3} g'(0, \phi, Pr, \alpha). \quad (10.12)$$

The last condition indicates the impracticality of procurement similar solutions for an adiabatic interface ($\theta'(0) = 0$).

10.2 Solution of the problem

Here, we give the analytic and uniformly valid solutions by using BVP4c package.

For

BVP4c, it is essential to put the governing equations, corresponding boundary conditions, initial guess and auxiliary linear operators for required solution. Choose the auxiliary linear operator and initial guess as follows

$$\mathcal{L}_1(f) = \frac{d^3 f}{d\eta^3} - \frac{df}{d\eta}, \quad \mathcal{L}_2(\theta) = \frac{d^2 \theta}{d\eta^2} - \theta. \quad (10.13)$$

$$f_0(\eta) = \frac{\mu_f}{\mu_{nf}} + x - \frac{\mu_f}{\mu_{nf}} e^{-\eta}, \quad \theta_0(\eta) = e^{-\eta/\alpha}. \quad (10.14)$$

Using the auxiliary operators and the initial approximations given in Eqs. (10.13) and (10.14) respectively, the coupled nonlinear Eqs. (10.8) and (10.9) subject to the boundary conditions (10.11) can be solved directly via BVP4c. In order to validate the results, we have compared our results with those obtained by Golia et al. [146] and Arifin et al. [147] different values of Pr and α for pure water as shown in table 10.3.

Table 10.3. Comparison of the solutions with Golia and Arifin.

α	$f'(0)$			$-\theta'(0)$			$-\theta'(0)$		
	Present	Golia	Arifin	Present	Golia	Arifin	Present	Golia	Arifin
	Pr=0.74			Pr=0.74			Pr=6.9		
.5	1.9834	1.98	1.9843	1.3949	1.39	1.3954	4.5125	4.51	4.5125
1	1.6961	1.69	1.6969	1.4854	1.48	1.4856	4.7675	4.76	4.7690
2	1.5657	1.56	1.5660	1.5897	1.59	1.5967	5.0978	5.10	5.1002

10.3 Results and discussion

The impact parameters involved in the expression of velocity and temperature distributions are examined in this section through Figs. 10.2 to 10.7 with aqueous solutions of ethylene glycol based nanofluid containing different shapes of copper nanoparticles. The governing equations along with corresponding boundary conditions are transferred to ordinary differential equations. These equations include the nanoparticles volume fraction ϕ and similarity parameter α . Particularly interesting are the flow-fields relative to value of α . When one choose $\alpha = 0.5$, the interface and external velocities are uniform and the temperature gradient at the interface is constant at the value of $\alpha = 1$. We consider 30% composition of ethylene glycol in water as a base fluid for velocity and temperature profiles. For particle shape effect on velocity and temperature profile, applying the Eq. (1.17). Take sphere shape particle of $5nm$ radius, needle shape of $5nm$ radius and $250nm$ length and disc shape of $250nm$ radius and thinness of $5nm$. In the thermal conductive model, chose $a = b = c = 5$ for sphere shape, $a = 250$, $c = b = 5$ for needle shape particle and $a = b = 2500$, $c = 5$ for disc particle. It also considers nano-layer thickness $2nm$ of base fluid on particle and for this take the value $t_1 = 24$. The thermal conductive of nano-layer k_f is considered $2k_f$. Figs. 10.2 and 10.3 illustrate the volume friction effect on velocity and temperature of the fluid. These figures are prepared within the range of particle volume fraction $2\% \leq \phi \leq 4\%$ with the postulation that the interface and external velocities remain uniform. Fig. 10.2 illustrates the effect of particle volume friction on velocity profile of nanofluids. It is observed that the momentum boundary layer thickness and velocity of fluid are increased and decreased respectively with the enhancement in the influence of volume friction of nanoparticle. It is also noted that the maximum decrease in the velocity is caused by the needle

shape, which followed by disc and sphere shape particles respectively. It is in accordance with the physical expectation in which nano-fluid contains needle shape particle require maximum viscosity as compare to disc and sphere shape particle contained nanofluids. Fig. 10.3 shows the effect of nanoparticle volume fraction on temperature profile of nanofluids. It is seen that the thermal boundary layer thickness and temperature of fluid are increased by increasing the particle volume fraction. It is also perceived that the maximum increase in the temperature of nanofluid is motivated by the disk, followed by needle and sphere shape particles respectively. It is just because of that nano-fluid which contains disk shape particle having maximum thermal conductivity then other needle and sphere shape particle contained nanofluids. Figs. 10.4 and 10.5 display the behavior of similarity parameter α on velocity and temperature profiles of nanofluid. It is seen that the value of α increases the velocity profile and as a result momentum boundary layer thickness is declined. It is also realized that the maximum momentum boundary layer thickness is caused by the needle shaped nanoparticles as compare to other particle's shapes. In Fig. 10.5, the result demonstrates that temperature profile and thermal boundary layer are decreased by increasing the value of α . The maximum thermal boundary layer thickness is found by disc shape particle than other particle's shapes. It is shown in Figs. 10.6 and 10.7 that with the increase of concentration of nanoparticles, the interface velocity and surface temperature gradient decrease.

The numerically results in tables 10.4 to 10.8 illustrate the effects of various parameters on interface velocity $f'(0)$ and the surface temperature gradient $-\theta'(0)$ in the presence of spherical and non-spherical nanoparticles in aqueous solutions of ethylene glycol base fluid. Table 10.4 shows the behavior of nanoparticle volume fraction on interface velocity $f'(0)$ and the surface temperature gradient $-\theta'(0)$ that represents the heat transfer rate at the surface. It is found that when nanoparticle volume fraction is increased both the interface velocity $f'(0)$ and the surface temperature gradient $-\theta'(0)$ decrease for all shapes of particle. It is also noticed that the entire values of $-\theta'(0)$ remain positive and the heat is transferred from the hot interface to the cold fluid always. On the other hand, a decrease in thermal conductivity enhances the heat transfer rate at the surface. The thermal conductive of needle and disk shapes contained nanofluids are 5% and 2% maximum as compared to sphere shape particle contained nanofluid at 2% volume fraction.

Therefore the enhancement in heat transfer rate of spherical particle contained nanofluid is achieved 2.94% and 5.14% to the needle and disc shapes particle contained nanofluids respectively. The effects of particle's size on interface velocity $f'(0)$ and the surface temperature gradient $-\theta'(0)$ are shown in tables 10.5 to 10.8. In these tables, we examine that surface temperature gradient increase with the enhancement in length and radius of needle shaped, radius and thickness of disc shaped and radius of sphere shaped particles. One can easily observe that the thermal conductivity of nanofluid decreases when size of particle is increased. For instance, when one takes a sphere particle of 30nm radius, the thermal conductivity of nanofluid is decreased 17.4% corresponding to a particle of radius 5nm at 2% particle volume fraction. Therefore, heat transfer rate at the surface increases when size of particle is increased. The improvement in heat transfer rate at the surface is happened due to sphere shape of particle as compared to other shapes. These tables also spectacle that there is no effective change is happened in interface velocity. To investigate the interface velocity $f'(0)$ and $-\theta'(0)$, the heat transfer rate measure the three different concentrations of ethylene glycol in water as base fluids. It is detected that the concentrations of ethylene glycol increases then the heat transfer rate at surface is improved 2%, 4.8% and 8.7% correspondence to 30%, 60% and 90% volume concentrations of ethylene glycol in water respectively when choose spherical particle and 2% volume fraction of particles for interface velocity $f'(0)$ and heat transfer rate at surface $-\theta'(0)$.

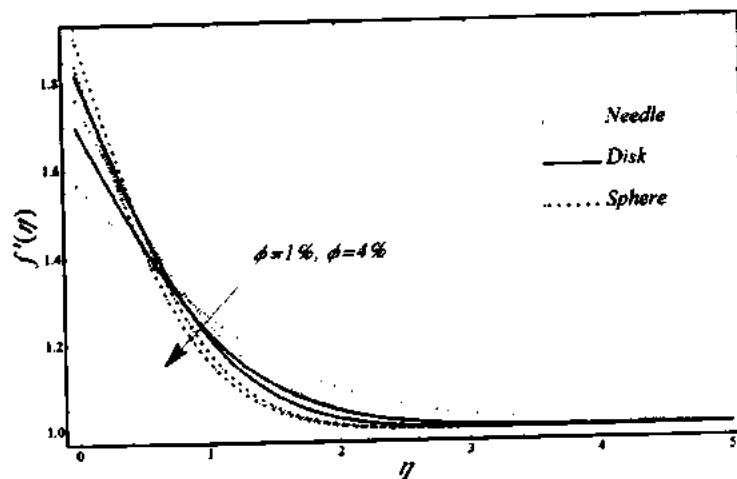


Fig. 10.2. Effect of volume fraction on velocity profile when $\alpha = 0.5$.

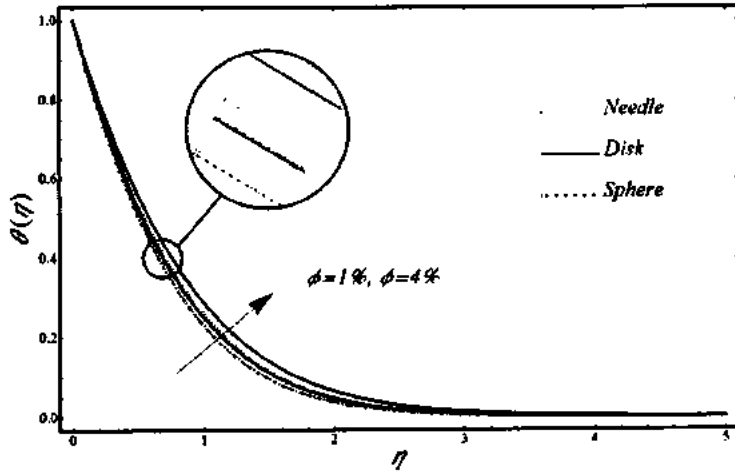


Fig. 10.3. Effect of volume fraction on temperature profile when $\alpha = 0.5$.

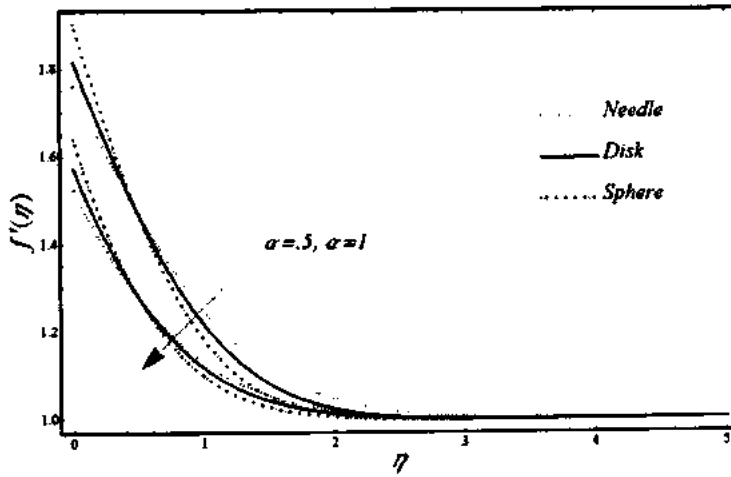


Fig. 10.4. Effect of similarity parameter on velocity profile when $\phi = 2\%$.

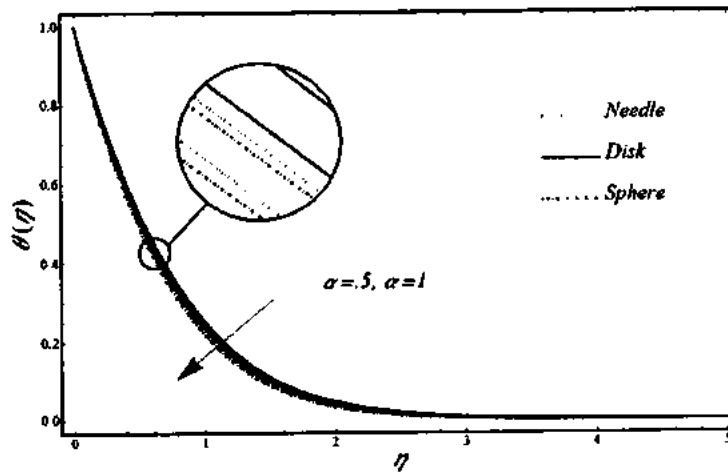


Fig. 10.5. Effect of similarity parameter on temperature profile $\phi = 2\%$.

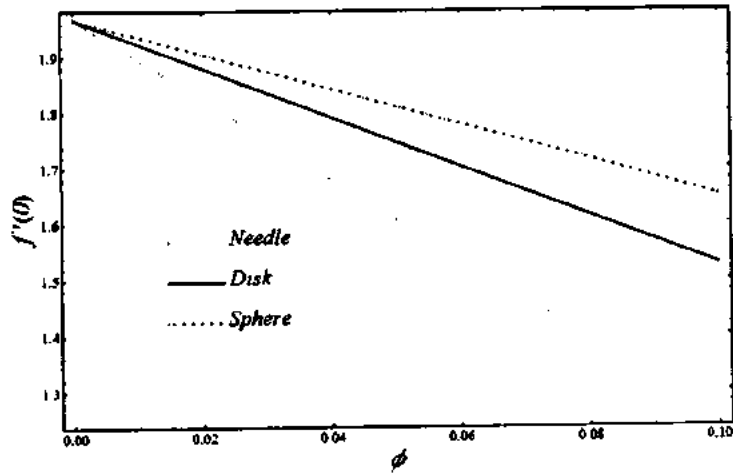


Fig. 10.6. Effect of particle volume fraction on interface velocity.

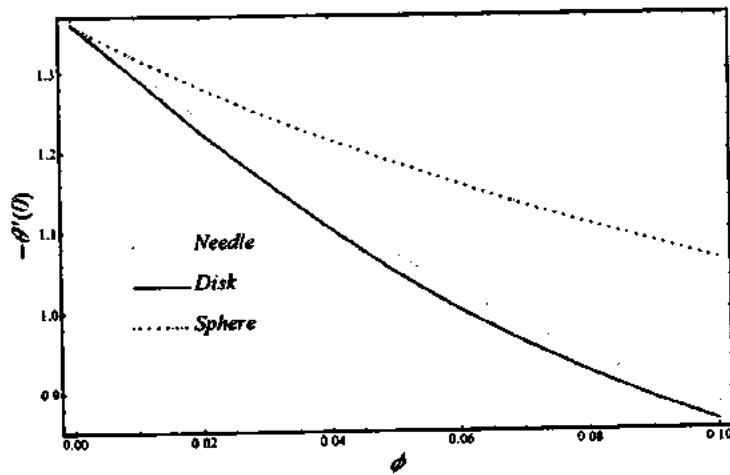


Fig. 10.7. Effect of particle volume fraction on surface temperature gradient.

Table 10.4. Effect of volume fraction on interface velocity and surface temperature.

	ϕ	Needle	Disk	Sphere
$-\theta'(0)$	0%	1.36398	1.36398	1.36398
	2%	1.23704	1.20492	1.28485
	4%	1.12956	1.08295	1.21497
$f'(0)$	0%	1.98343	1.98343	1.98343
	2%	1.75216	1.81697	1.90750
	4%	1.55574	1.6832	1.84232

Table 10.5. Effect of size of Needle on interface velocity and surface temperature.

	Dimension	Needle
$-\theta'(0)$	$a = 250, b = c = 5$	1.23704
	$a = 500, b = c = 15$	1.24386
	$a = 1000, b = c = 30$	1.24542
$f'(0)$	$a = 250, b = c = 5$	1.75216
	$a = 500, b = c = 15$	1.75215
	$a = 1000, b = c = 30$	1.75214

Table 10.6. Effect of size of disk on interface velocity and surface temperature.

	Dimension	Disk
$-\theta'(0)$	$a = b = 5, c = 250$	1.20492
	$a = b = 15, c = 500$	1.21375
	$a = b = 30, c = 1000$	1.21443
$f'(0)$	$a = b = 5, c = 250$	1.81697
	$a = b = 15, c = 500$	1.81698
	$a = b = 30, c = 1000$	1.81698

Table 10.7. Effect of size of sphere on interface velocity and surface temperature.

	Dimension	Sphere
$-\theta'(0)$	$a = b = c = 5$	1.28485
	$a = b = c = 15$	1.28758
	$a = b = c = 30$	1.29064
$f'(0)$	$a = b = c = 5$	1.90750
	$a = b = c = 15$	1.90751
	$a = b = c = 30$	1.90751

Table 10.8. Effect of concentrations of Ethylene Glycol on interface velocity and surface temperature.

	ϕ	Needle	Disk	Sphere
$-\theta'(0)$	30%	1.2370	1.2049	1.2848
	60%	1.2393	1.2072	1.2876
	90%	1.2429	1.2107	1.2915
$f'(0)$	30%	1.7521	1.8169	1.9075
	60%	1.7541	1.8189	1.9096
	90%	1.7554	1.8204	1.9113

10.4 Conclusions

In this chapter, we have analyzed the shape effect with nano-layer effect on aqueous solutions based nanofluid with influence of different parameters. The velocity of nanofluid decreases by increasing particle volume fraction and similarity parameters. With the increase in particle volume fraction and similarity parameter, temperature profile is correspondingly enhanced and decline. The lowest velocity and highest temperature of nanofluid is cause by Needle and disk shaped particle. Consequence for interface velocity and the surface temperature gradient are perceived by numeric set of results. It is found that the interface velocity is declined by increasing particle volume fraction and volume concentration of ethylene glycol in the water. The minimum interface velocity is seen by needle shaped particle and 30% concentrations of ethylene glycol. With increase in volume fraction and size of particle, the behaviors of surface temperature gradient are found decreasing and increasing function respectively. The maximum heat transfer rate at the surface is achieved when we chose sphere nanoparticles and 90% concentrations of ethylene glycol as compared to other shapes and concentrations. It is worth mentioning that no such analysis exists in the literature yet. The results obtained are specifically important in the processes of polymer industry and metallurgical.

References

- [1] M. Sheikholeslami, M. G. Bandpy, D. D. Ganji, S. Soleimani and S. M. Seyyedi, Natural convection of nanofluids in an enclosure between a circular and a sinusoidal cylinder in the presence of magnetic field, *International Communications in Heat and Mass Transfer*, 39 (2012) 1435-1443.
- [2] D. Y. Shang, *Free convection film flows and heat transfer: Models of laminar free convection with phase change for heat and mass transfer analysis*, 2nd Ed. Springer, 2012.
- [3] I. A. Popov, Y. F. Gortyshov and V. V. Olimpiev, Industrial applications of heat transfer enhancement: The modern state of the problem (a Review), *Thermal Engineering*, 59 (2012) 1-12.
- [4] I. A. Popov, Y. F. Gortyshov, V. V. Olimpiev, Industrial applications of heat transfer enhancement: The modern state of the problem (a Review), *Thermal Engineering*, 59 (2012) 1-12.
- [5] D. S. Wen and Y. L. Ding, Experimental investigation into convective heat transfer of nanofluids at the entrance region under laminar flow conditions, *International Journal of Heat and Mass Transfer*, 47 (2004) 5181-5188.
- [6] J. Niu, C. Fu and W. Tan, Slip-flow and heat transfer of a non-Newtonian nanofluid in a microtube, 7 (2012) 37274-37283
- [7] R. Ellahi, M. Raza, and K. Vafai, Series solutions of non-Newtonian nanofluids with Reynolds' model and Vogel's model by means of the homotopy analysis method, *Mathematical and Computer Modelling*, 55 (2012) 1876–1891.
- [8] N. Bachok, A. Ishak and I. Pop, Boundary-layer flow of nanofluids over a moving surface in a flowing fluid, *International Journal of Thermal Sciences*, 49 (2010), 1663-1668.
- [9] K. V. Wong and O. D. Leon, Applications of nanofluids: current and future, *Advances in Mechanical Engineering*, 2010 (2010) 11-21.
- [10] S. K. Das, S. U. S. Choi and H. E. Patel, Heat transfer in nanofluids-a review, *Heat Transfer Engineering*, 27 (2006) 3-19.

- [11] C. Fetecau, M. Rana, and C. Fetecau, Radiative and porous effects on free convection flow near a vertical plate that applies shear stress to the fluid, *Zeitschrift fur Naturforschung Section A-J*, 68 (2013) 130–138.
- [12] M. I. A. Othman, S. M. Abo-Dahab and K. Lotfy, Gravitational effect and initial stress on generalized magneto-thermo-microstretch elastic solid for different, *Applied Mathematics and Computation*, 230 (2014) 597-615.
- [13] I. A. Abbas, M. F. El-Amin and A. Salama, Effect of thermal dispersion on free convection in a fluid saturated porous medium, *International Journal of Heat and Fluid Flow*, 30 (2009) 229-236.
- [14] F. N. Lin, Laminar free convection from a vertical cone with uniform surface heat flux, *Heat Mass Transfer*, 3 (1976) 49–58.
- [15] I. Pop and T. Watanabe, Free convection with uniform suction or injection from a vertical cone for constant wall heat flux, *International Communications in Heat and Mass Transfer*, 19 (1992) 275–283.
- [16] M. A. Hossain, S. C. Paul and A. C. Mandal, Natural convection flow along a vertical circular cone with uniform surface temperature and surface heat flux in a thermally stratified medium, *International Journal of Numerical Methods for Heat & Fluid Flow*, 12 (2002) 290-305.
- [17] K. A. Yih, Couoled heat and mass transfer in mixed convection over a truncated cone in porous media, *Acta Mechanica*, 137 (1999) 83-97.
- [18] S. Nadeem, R. U. Haq, N. S. Akbar, Z. H. Khan, MHD three-dimensional Casson fluid flow past a porous linearly stretching sheet, *Alexandria Engineering Journal*, 52 (2013) 577–682.
- [19] P. Vadasz, *Emerging topics in heat and mass transfer in porous media*, Springer, New York, (2008).
- [20] D. B. Ingham and I. Pop, *Transport phenomena in porous media*, Vol. III, Elsevier, Oxford, (2005).
- [21] R. L. Hamilton and O. K. Crosser, Thermal conductivity of heterogeneous two-component system, *Industrial & Engineering Chemistry Fundamentals*, 1 (1962) 187-191.
- [22] Y. Rao, Nanofluids stability, phase diagram, rheology and applications, *Particuology*, 8 (2010) 549-555.

- [23] S. K. Das, N. Putra, P. Thiesen and W. Roetzel, Temperature dependence of thermal conductivity enhancement for nanofluids, *Journal of Heat Transfer*, 125 (2003) 567-574.
- [24] J. A. Eastman, S. U. S. Choi, S. Li, W. Yu and L. J. Thompson, Anomalously increased effective thermal conductivities of ethylene glycol-Based nanofluids containing copper nanoparticles, *Applied Physics Letters*, 78 (2001) 718-720.
- [25] H. E. Patel, S. k. Das, T. Sundararajan, A. S. Nair, B. George and T. Pradeep, Thermal conductivities of naked and monolayer protected metal nanoparticle based nanofluids: Manifestation of anomalous enhancement and chemical effects, *Applied Physics Letters*, 83 (2003) 2931-2933.
- [26] H. Xie, J. Wang, T. Xi, Y. Liu, F. Ai and Q. Wu, Thermal conductivity enhancement of suspensions containing nanosized alumina particles, *Journal of Applied Physics*, 91 (2002) 4568-4572.
- [27] C. H. Chon, K. D. Kihm, S. P. Lee and S. U. S. Choi, Empirical correlation finding the role of temperature and particle size for nanofluid (Al_2O_3) thermal conductivity enhancement, *Applied Physics Letters*, 87 (2005) 1531071-1531073.
- [28] H. Xie, J. Wang, T. Xi and Y. Liu, Thermal Conductivity of Suspensions Containing Nanosized SiC Particles, *International Journal of Thermophysics*, 23 (2002) 571-580.
- [29] H. Xie, H. Lee, W. Youn and M. Choi, Nanofluids containing multiwalled carbon nanotubes and their enhanced thermal conductivities, *Journal of Applied Physics*, 94 (2003) 4967-4971.
- [30] S. Lee, S. U. S. Choi, S. Li and J. A. Eastman, measuring thermal conductivity of fluids containing oxide nanoparticles, *Transactions of the ASME, Journal of Heat Transfer*, 121 (1999) 280-289.
- [31] Y. Xuan and Q. Li, Heat transfer enhancement of nanofluids, *International Journal of Heat and Fluid Flow*, 21 (2000) 58-64.
- [32] S. M. S. Murshed, K. C. Leong and C. Yang, Enhanced thermal conductivity of TiO_2 -water based nanofluids, *International Journal of Thermal Sciences*, 44 (2005) 367-373.
- [33] D. Lee, J. W. Kim and B. G. Kim, A new parameter to control heat transport in nanofluids: surface charge state of the particle in suspension, *Journal of Physical Chemistry B*, 110 (2006) 4323-4328.

- [34] D. Lee, Thermophysical properties of interfacial layer in nanofluids, *Langmuir*, 23 (2007) 6011-6018.
- [35] M. Sheikholeslami, M. Gorji-Bandpy, D. D. Ganji, P. Rana and S. Soleimani, Magneto hydrodynamic free convection of Al₂O₃-water nanofluid considering thermophoresis and Brownian motion effects, *Computers & Fluids*, 94 (2014) 147--160.
- [36] M. Sheikholeslami and D. D. Ganji, Numerical investigation for two phase modeling of nanofluid in a rotating system with permeable sheet, *Journal of Molecular Liquids*, 194 (2014) 13-19.
- [37] M. Sheikholeslami, M. Gorji-Bandpy and D.D. Ganji, Lattice Boltzmann method for MHD natural convection heat transfer using nanofluid, *Powder Technology*, 254 (2014) 82-93.
- [38] H. F. Oztop and E. Abu-Nada, Numerical study of natural convection in partially heated rectangular enclosures filled with nanofluids, *International Journal of Heat and Mass Transfer*, 29 (2008) 1326-1336.
- [39] D. A. Nield and A. V. Kuznetsov, The Cheng-Minkowycz problem for natural convective boundary layer flow in a porous medium saturated by a nanofluid, *International Journal of Heat and Mass Transfer*, 52 (2009) 5792-5795.
- [40] W. C. Tan and T. Masuoka, Stokes' first problem for a second grade fluid in a porous half space with heated boundary, *International Journal of Non-Linear Mechanics*, 40 (2005) 512-522.
- [41] W. C. Tan and T. Masuoka, Stability analysis of a Maxwell fluid in a porous medium heated from below, *Physics Letters A*, 360 (2007) 454-460.
- [42] A. Ibrahim, M. F. El-Amin and A. Salama, Effect of thermal dispersion on free convection in a fluid saturated porous medium, *International Journal for Numerical Methods for Heat and Fluid Flow*, 3 (2009) 229-236.
- [43] N. Sinha and J. Yeow., Carbon nano tube, *IEEE Transaction on Nano-Science*, 4 (2005) 180-195.
- [44] M. J. Biercuk, M. C. Llaguno, M. Radosavljevic, J. K. Hyun and A. T. Johnson, Carbon nanotube composites for thermal management, *Applied Physics Letters*, 80 (2002) 2767-2769.
- [45] G. D. Zhan, J. D. Kuntz, J. Wan and A. K. Mukherjee, Single-wall carbon nanotubes as attractive toughening agents in alumina-based nanocomposites, *Nature Mater*, 2 (2003) 38-42.

- [46] C. H. Liu, H. Huang, Y. Wu and S. S. Fan, Thermal conductivity improvement of silicone elastomer with carbon nanotube loading, *Applied Physics Letters*, 84 (2004) 4248-4250.
- [47] R. Sivakumar, S. Q. Guo, T. Nishimura and Y. Kagawa, Thermal conductivity in multi-wall carbon nanotube/silica-based nanocomposites, *Scripta Materialia*, 56 (2007) 265-268.
- [48] K. Chu, Q. Wu, C. Jia, X. Liang, J. Nie, W. Tian, G. Gai and H. Guo, Fabrication and effective thermal conductivity of multi-walled carbon nanotubes reinforced Cu matrix composites for heat sink applications, *Composites Science and Technology*, 70 (2010) 298-304.
- [49] L. Chen, H. Xie, Y. Li and W. Yu, Nanofluids containing carbon nanotubes treated by mechanochemical reaction, *Thermochim. Acta*, 477 (2008) 21-24.
- [50] T. X. Phuoc, M. Massoudi and R. H. Chen, Viscosity and thermal conductivity of nanofluids containing multi-walled carbon nanotubes stabilized by chitosan, *International Journal of Thermal Sciences*, 50 (2011) 12-18.
- [51] S. U. S. Choi, Z. G. Zang, W. Yu, F. E. Lookwood and E. A. Grulke, Anomalous thermal conductivity enhancement in nanotube suspensions, *Applied Physics Letters*, 79, (2001) 2252-2254.
- [52] P. Garg, J. L. Alvarado, C. Marsh, T. A. Carlson, D. A. Kessler and K. Annamalai, An experimental study on the effect of ultrasonication on viscosity and heat transfer performance of multi-wall carbon nanotube-based aqueous nanofluids, *International Journal of Heat and Mass Transfer*, 52 (2009) 5090-5101.
- [53] Y. Bakhshan, A. Hajhosseini and F. Kamel, Using of multi-wall carbon nanotube (MWCNT) based nanofluid in the heat pipe to get better thermal performance, 2014, (2014) 1-7.
- [54] G. H. Ko, K. Heo, K. Lee, D. S. Kim, C. Kim, Y. Sohn and M. Choi, An experimental study on the pressure drop of nanofluids containing carbon nanotubes in a horizontal tube, *International Journal of Heat and Mass Transfer*, 50 (2007) 4749-4753.
- [55] Y. Zhao and S. Liao, HAM-based package BVPh 2.0 for nonlinear boundary value problems, in: S. Liao (Ed.), *Advances in Homotopy Analysis Method*, World Scientific Press, 2013.

- [56] E. E. Bajestan, H. Niazmand and M. Renksizbulut, Flow and heat transfer of nanofluids with temperature dependent properties, Proceedings of ASME 2010 3rd Joint US-European Fluids Engineering Summer Meeting and 8th International Conference on Nanochannels, Microchannels and Minichannels, FEDSM2010-ICNMM2010, Montreal, Canada, 2010.
- [57] E. E. Bajestan and H. Niazmand, Convective heat transfer of nanofluids flows through an isothermally heated curved pipe, Iranian Journal of Chemical Engineering, 8 (2011) 81-97.
- [58] N. K. Ghaddar, Natural convection heat transfer between a uniformly heated cylindrical element and its rectangular enclosure, International Journal of Heat and Mass Transfer, 35 (1992) 2327-2334.
- [59] T. H. Kuehn and R. J. Goldstein, An experimental and theoretical study of natural convection in the annulus between horizontal concentric cylinders, Journal of Fluid Mechanics, 74 (1976) 695-719.
- [60] S. C. Halder, Combined convection in developing flow through a horizontal concentric annulus, Numerical Heat Transfer A, 34 (1998) 673-685.
- [61] E. Abu-Nada, Z. Masoud and A. Hijazi, Natural convection heat transfer enhancement in horizontal concentric annuli using nanofluids, International Communications in Heat and Mass Transfer, 35 (2008) 657-665.
- [62] H. Saleh, R. Roslan and I. Hashim, Natural convection heat transfer in a nanofluid-filled trapezoidal enclosure, International Journal of Heat and Mass Transfer, 54 (2001)194-201.
- [63] S. Nadeem, R. U. Haq, Z. H. Khan, Heat transfer analysis of water-based nanofluid over an exponentially stretching sheet, Alexandria Engineering Journal, 53 (2014) 219-224.
- [64] S. Nadeem, S. T. Hussain, Flow and heat transfer analysis of Williamson nanofluid, Applied Nanoscience, 4 (2013) 1005-1012.
- [65] E. Abu-Nada and F. Oztop, Effects of inclination angle on natural convection in enclosures filled with Cu-water nanofluid. International Journal for Numerical Methods for Heat and Fluid Flow, 30 (2009) 669-678.
- [66] E. Abu-Nada, Effects of variable viscosity and thermal conductivity of Al_2O_3 -water nanofluid on heat transfer enhancement in natural convection

- International Journal for Numerical Methods for Heat and Fluid Flow, 30 (2009) 679-690.
- [67] S. H. Noie, M. Kahani and S. M. Nowee, Heat transfer enhancement using Al_2O_3 /water nanofluid in a two-phase closed thermosyphon. International Journal for Numerical Methods for Heat and Fluid Flow, 30 (2009) 700-705.
- [68] S. M. Fotukian and M. N. Esfahany, Experimental investigation of turbulent convective heat transfer of dilute $\gamma\text{-Al}_2\text{O}_3$ /water nanofluid inside a circular tube. International Journal for Numerical Methods for Heat and Fluid Flow, 31 (2009), 606-612.
- [69] B. R. Baliga, Control-volume finite element methods for fluid flow and heat transfer. In: W.J. Minkowycz, E.M. Sparrow, editors. Advances in numerical heat transfer, first Ed. Taylor & Francis, New York, 1996.
- [70] B. R. Baliga and S. V. Patankar, A control volume finite-element method for two-dimensional fluid flow and heat transfer, Numerical Heat Transfer 6 (1983) 245-261.
- [71] V. R. Voller, Basic Control Volume Finite Element Methods for Fluids and Solids, World Scientific Publishing Co. Pte. Ltd. 5 Tohccxxvc, University of Minnesota, USA, 2009.
- [72] M. Sheikholeslami, M. Gorji-Bandpy, I. Pop and S. Soleimani, Numerical study of natural convection between a circular enclosure and a sinusoidal cylinder using control volume based finite element method, International Journal of Thermal Sciences, 72 (2013) 147-158.
- [73] M. Sheikholeslami, M. G. Bandpy, R. Ellahi, M. Hassan and S. Soleimani, Effects of MHD on Cu-water nanofluid flow and heat transfer by means of CVFEM, Journal of Magnetism and Magnetic Materials. 349 (2014) 188–200.
- [74] M. Sheikholeslami, M. Gorji-Bandpy, D. D. Ganji and S. Soleimani, Effect of a magnetic field on natural convection in an inclined half-annulus enclosure filled with Cu–water nanofluid using CVFEM, Advanced Powder Technology, 24 (2013) 980–991.
- [75] A. R. Sajadi, S. S. Ssdati, M. Nourimotlagh, O. Pakbaz, D. Ashtiani and F. Kowsari, Experimental study on turbulent convective heat transfer, pressure drop and thermal performance of ZnO /Water nanofluid in a circular tube, Thermal Science, 18 (2014) 1315-1326.

- [76] S. S. Pawar and V. K. Sunnapwar, Experimental studies on heat transfer to Newtonian and non-Newtonian fluids in helical coils with laminar and turbulent flow, *Experimental Thermal and Fluid Science*, 44 (2013) 792–804.
- [77] N. Shalkevich, W. Escher, T. Buergi, B. Michel, L. Si-Ahmed and D. Poulikakos, On the thermal conductivity of gold nanoparticle colloid, 26 (2010) 663-670.
- [78] D. M. Yu, J. L. Routbort and S. U. S. Choi, Review and comparison of nanofluid thermal conductivity and heat transfer enhancements, *Heat Transfer Engineering*, 29 (2008) 432-460.
- [79] J. A. Eastman, S. R. Phillpot, S. U. S. Choi and P. Keblinski, Thermal transport in nanofluids, *Annual Review of Materials Research*, 34 (2004) 219-246.
- [80] J. Fan and L. Wang, Review of heat conduction in nanofluids, *Journal of Heat Transfer*, 133 (2011) 0408011- 0408014.
- [81] P. Keblinski, R. Prasher and J. Eapen, Thermal conductance of nanofluids: is the controversy over? *Journal of Nanoparticle Research*, 10 (2008) 1089-1097.
- [82] C. Kleinstreuer and Y. Feng, Experimental and theoretical studies of nanofluid thermal conductivity enhancement: A Review, *Nanoscale Research Letter*, 6 (2011) 229.
- [83] D. Singh, E. Timofeeva, W. Yu, J. Routbort, D. France, D. Smith and J. Lopez-Cepero, An investigation of silicon carbide-water nanofluid for heat transfer applications, *Journal of Applied Physics*, 15 (2009) 064306.
- [84] S. Khandekar, Y. M. Joshi and B. Mehta, Thermal performance of closed two-phase thermosyphon using nanofluids. *International Journal of Thermal Sciences*, 47 (2008) 659-667.
- [85] N. Bachok, A. Ishak and I. Pop, The boundary layers of an unsteady stagnation-point flow in a nanofluid, *International Journal of Heat and Mass Transfer*, 55 (2012) 6499-6505.
- [86] S. S. Sebti, M. Mastiani, H. Mirzaei, A. Dadvand and S. A. Kashani, Numerical study of the melting of nano-enhanced phase change material in a square cavity, *Journal of Zhejiang University SCIENCE A*, 14 (2013) 307-316.

- [87] J. Xie, X. Zhao, J. Mi, G. Cao and J. Tu, Solvothermal synthesis of nanosized CoSb₃ skutterudite, *Journal of Zhejiang University Science*, 5 (2004) 1504-1508.
- [88] K. Kwak and C. Kim, Viscosity and thermal conductivity of copper oxide nanofluid dispersed in ethylene glycol, *Korea-Australia Rheology Journal* 17 (2005) 35-40.
- [89] J. Philip, P. D. Shima and R. Baldev, Nanofluid with tunable thermal properties, *Applied Physics Letters*, 92 (2008) 043108.
- [90] W. H. Shih, W. Y. Shih, S. I. Kim, J. Liu and I. A. Aksay, Scaling behavior of the elastic properties of colloidal gels, *Phys. Rev. A* 42 (1990) 4772-4779.
- [91] K. Arafune and A. Hirata, Thermal and solutal Marangoni convection in In-Ga-Sb system, *Journal of Crystal Growth*, 197 (1999) 811-817.
- [92] D. M. Christopher and B. Wang, Prandtl number effects for Marangoni convection over a flat surface, *International Journal Thermal Sciences*, 40 (2001) 564-570.
- [93] L. G. Napolitano, Marangoni boundary layers. In: *Proc. 3rd European symposium on material science in space*, Grenoble, ESA SP-142 (1979).
- [94] N. M. Arifin, R. Nazar and I. Pop, Non-isobaric Marangoni boundary layer flow for Cu, Al₂O₃ and TiO₂ nanoparticles in a water based fluid, *Meccanica*, 46 (2011) 833-843.
- [95] N. A. A. Mat, N. M. Arifin, R. Nazar, and F. Ismail, Radiation effect on Marangoni convection boundary layer flow of a nanofluid, *Mathematical Sciences*, 6 (2012) 1-6.
- [96] R. K. Tiwari and M. K. Das, Heat transfer augmentation in a two-sided lid-driven differentially heated square cavity utilizing nanofluids, *International Journal of Heat and Mass Transfer*, 50 (2007) 2002-2018.
- [97] D. Sastry, A. S. N. Murthi and T. P. Kantha, The effect of heat transfer on MHD marangoni boundary layer flow past a flat plate in nanofluid, *International Journal of Engineering Mathematics*, 2013 (2013) 1-6.
- [98] B. C. Pak and Y. I. Cho, Hydrodynamic and heat transfer study of dispersed fluids with submicron metallic oxide particles, *Experimental Heat Transfer*, 11 (1999) 151-170.
- [99] C. J. Ho, W. K. Liu, Y. S. Chang and C. C. Lin, Natural convection heat transfer of alumina-water nanofluid in vertical square enclosures: an

- experimental study, *International Journal of Thermal Sciences*, 49 (2010) 1345-1353.
- [100] S. Q. Zhou and R. Ni, Measurement of the specific heat capacity of water-based Al_2O_3 nanofluid, *Applied Physics Letters*, 92 (2008) 093123.
- [101] K. Khanafer and K. Vafai, A critical synthesis of thermophysical characteristics of nanofluids, *International Journal of Heat and Mass Transfer* 54 (2011) 4410-4428.
- [102] S. Halelfadl, P. Estelle, B. Aladag, N. Doner and T. Mare, Viscosity of carbon nanotubes water based nanofluids: Influence of concentration and temperature. *International Journal of Thermal Sciences*, Elsevier, 71 (2013) 111-117.
- [103] V. Y. Rudyak, Viscosity of nanofluids-Why it is not described by the classical theories, *Advances in Nanoparticles*, 2 (2013) 266-279.
- [104] N. Jamshidi, M. Farhadi, D. D. Ganji and K. Sedighi, Experimental Investigation on the Viscosity of Nanofluids, *IJE Transactions B: Applications*, 25 (2012) 201-209.
- [105] A. Einstein, *Investigations on the Theory of the Brownian Movement*, Dover Publications, Inc., New York, (1956).
- [106] H. C. Brinkman, The viscosity of concentrated suspensions and solutions, *Journal of Chemical Physics*, 20 (1952) 571-581.
- [107] G. Batchelor, The effect of Brownian motion on the bulk stress in a suspension of spherical particles, *Journal of Fluid Mechanics*, 83 (1977) 97-117.
- [108] H. Brenner, and D. W. Condiff, Transport mechanics in systems of orientable particles, Convective transport, *Journal of Colloid and Interface Science*, 47 (1974) 199-264.
- [109] J. Avsec and M. Oblak, The Calculation of Thermal Conductivity, Viscosity and Thermodynamic Properties for Nanofluids on the Basis of Statistical Nanomechanics, *International Journal of Heat and Mass Transfer*, 50 (2007) 4331-4341.
- [110] W. Evans, R. Prasher, J. Fish, and P. Meakin, Effect of aggregation and interfacial thermal resistance on thermal conductivity of nanocomposites and

- colloidal nanofluids, *International Journal of Heat and Mass Transfer*, 51 (2008) 1431-1438.
- [111] M. Kole, D. Tripathi and T. K. Dey, Percolation based enhancement in effective thermal conductivity of HDPE/LBSMO composites, *Bulletin of Materials Science*, 35 (2012) 601–609.
- [112] J. A. Eastman, S. U. S. Choi and L. J. Thompson and S. Lee, Anomalously increasing effective thermal conductivities of ethylene glycol-based nanofluids containing copper nanoparticles, *Applied Physics Letters*, 78 (2001) 718-720.
- [113] J. Garg, B. Poudel, M. Chiesa, J. B. Gordon, J. J. Ma, J. B. Wang, Z. F. Ren, Y. T. Kang, H. Ohtani, J. Nanda, G. H. McKinley and G. Chen, Enhanced thermal conductivity and viscosity of copper nanoparticles in ethylene glycol nanofluid, *Journal of Applied Phys*, 103 (2008) 074301-074301-6.
- [114] J. C. Maxwell, *A treatise on electricity and magnetism*, Clarendon Press, Oxford, U.K., 1 (1873) 360-366.
- [115] W. Yu and S. U. S. Choi, The role of interfacial layers in the enhanced thermal conductivity of nanofluids: A renovated Hamilton-Crosser model, *Journal of Nanoparticle Research*, 6 (2004) 355-361.
- [116] K. C. Leong, C. Yang and S. M. S. Murshed, A model for the thermal conductivity of nanofluids - the effect of interfacial layer, *Journal of Nanoparticle Research*, 8 (2006) 245-254.
- [117] H. Xie, M. Fujii and X. Zhang, Effect of interfacial nanolayer on the effective thermal conductivity of nanoparticle fluid mixture. *International Journal of Heat and Mass Transfer*, 48 (2005) 2926-2932.
- [118] P. Tillman and J. M. Hill, Determination of nanolayer thickness for a nanofluid. *International Communications in Heat and Mass Transfer*, 34 (2007) 399-407.
- [119] W. Yu and S. U. S. Choi, The role of interfacial layers in the enhanced thermal conductivity of nanofluids, A renovated Maxwell model, *Journal of Nanoparticle Research*, 5 (2003) 167-171.
- [120] C. Pang, J. Y. Jung and Y. T. Kang, Aggregation based model for heat conduction mechanism in nanofluids, *International Journal of Heat and Mass Transfer* 72 (2014) 392–399.

- [121] H. Zhu, C. Zhang, S. Liu, Y. Tang and Y. Yin, Effects of nanoparticle clustering and alignment on thermal conductivities of Fe₃O₄ aqueous nanofluids, *Applied Physics Letters*, 89 (2006), 023123.
- [122] M. S. Liu, M. C. C. Lin, C. Y. Tsai and C. C. Wang, Enhancement of thermal conductivity with Cu for nanofluids using chemical reduction method, *International Journal of Heat and Mass Transfer*, 49 (2006) 3028-3033.
- [123] A. H. Nayfeh, and D. T. Mook, *Nonlinear oscillations*, John Willey and Sons, New York, (1979).
- [124] J. H. He, Some asymptotic methods for strongly nonlinear equations, *International Journal of Modern Physics B*, 20 (2006) 1141-1199.
- [125] A. M. Wazwaz, The Tanh method for generalized forms of nonlinear heat conduction and Burger's-Fisher equations, *Applied Mathematics and Computation*, 152 (2004) 403-413.
- [126] Z. Fu, S. Liu, Q. Zhao, New Jacobi elliptic function expansion and new periodic solutions of nonlinear wave equations, *Physics Letters A*, 290 (2001) 72-76.
- [127] G. Adomian, A review of the decomposition method in applied mathematics, *Journal of Mathematical Analysis and Applications*, 135 (1998) 501-544.
- [128] S. J. Liao, Proposed homotopy analysis techniques for the solution of nonlinear problem, PhD dissertation, Shanghai Jiao Tong University, (1992).
- [129] S. Sen, *Topology and geometry for physicists*, Florida: Academic Press, (1983).
- [130] S. J. Liao, An approximate solution technique which does not depend upon small parameters (Part2): an application in fluid mechanics, *International Journal of Non-Linear Mechanics*, 32 (1997) 815-22.
- [131] Z. Niu and C. Wang, A one-step optimal homotopy analysis method for nonlinear differential equations, *Communications in Nonlinear Science and Numerical Simulation*, 15 (2010) 2026-2036.
- [132] E. V. Timofeeva, J. L. Routbort and Dileep Singh, Particle shape effects on thermo physical properties of alumina nanofluids, *Journal of Applied Physics*, 106 (2009) 014304-014310.
- [133] V. S. Arpaci, Radiative entropy production-lost heat into entropy, *International Journal of Heat and Mass Transfer*, 30 (1987) 2115 -2123.
- [134] L. C. Woods, *Thermodynamics of Fluid Systems*, Oxford Uni. Press, Oxford, (1975).

- [135] G. Makanda, O. D. Makinde and P. Sibanda, Natural convection of viscoelastic fluid from a Cone Embedded in a porous medium with viscous dissipation, *mathematical Problems in Engineering*, 2013 (2013) 1-11.
- [136] M. C. Ece, Free convection flow about a cone under mixed thermal boundary conditions and a magnetic field, *Applied Mathematical Modelling*, 29 (2005) 121-1134.
- [137] J. C. Maxwell, *A Treatise on Electricity and Magnetism*, second Ed. Oxford University Press, Cambridge, (1904) 435-441.
- [138] T. H. Kuehn and R. J. Goldstein, An experimental and theoretical study of natural convection in the annulus between horizontal concentric cylinders, *Journal of Fluid Mechanics*, 74 (1976) 695-719.
- [139] G. Laboni and G. Guj, Natural convection in a horizontal concentric cylindrical annulus: oscillatory flow and transition to chaos, *Journal of Fluid Mechanics*, 375 (1998) 179-202.
- [140] K. Khanafer, K. Vafai and M. Lightstone, Buoyancy-driven heat transfer enhancement in a two-dimensional enclosure utilizing nanofluids, *International Journal of Heat and Mass Transfer*, 46 (2003) 3639-3653.
- [141] G. De Vahl Davis, Natural convection of air in a square cavity, a benchmark numerical solution, *Int. J. Numer. Methods Fluids* 3 (1962) 249-264.
- [142] N. Rudraiah, R. M. Barron, M. Venkatachalappa and C. K. Subbaraya, Effect of a magnetic field on free convection in a rectangular enclosure, *International Journal of Engineering Science*, 33 (1995) 1075-1084.
- [143] Etemad S. Gh., Bagheri R., Heris S. Z., Theoretical and experimental study of the rheological behavior of non-Newtonian fluids using falling cylinder rheometer, 6th World Congress of Chemical Engineering Melbourne, Australia, (2011) 23-27.
- [144] S. Azeem and A. Ramzan, Approximate analytic solution for magneto-hydrodynamic flow of non-Newtonian fluid over a vertical stretching sheet, *Canadian Journal of Applied Sciences*, 2 (2012) 202-215.
- [145] A. J. Chamkha, I. Pop and H. S. Takhar, Marangoni mixed convection boundary layerflow. *Meccanica*, 41 (2006) 219-232.
- [146] Golia and A. Viviani, Non isobaric boundary layers related to Marangoni flows, *Meccanica*, 21 (1986) 200-204.

- [147] N. M. Arifin, R. Nazar and I. Pop, Non-isobaric Marangoni boundary layer flow for Cu, Al₂O₃ and TiO₂ nanoparticles in a water based fluid, *Meccanica*, 46 (2011) 833-843.

Nomenclature

u, v, w	Velocity components	f	dimensionless stream function
x, y, z	Cartesian coordinates	C_p	Specific heat
V	Velocity	K	Consistency index
n	Temperature power law index	$M_i, i = 1, 2.$	Magnetic parameters
n_1	Flow behavior index	p^*	Cluster spanning chain ratio
h_{layer}	Nanolayer thickness	p	Pressure
K_1	Permeability	Nu	Nusselt number
r^*	Nanoparticles ratio	Nu_x	Local Nusselt number
Pr	Prandtl number	C_f	Skin friction coefficient
Ra_x	Local Rayleigh number	T	Fluid temperature
Q	Heat generation parameter	n^*	Shape factor
Q_0	Heat generated / absorbed	h	Convergence parameter.
q	Embedding parameter	N	Radiation parameter
q_{rh}	Radioactive heat flux	q_w	Heat flux at wall
q_1	Heat flux	h_{layer}	Nanolayer thickness
Ec	Eckert number	q_w	Heat flux at wall
Gr	Grashof number	q	Embedding parameter
Gr_x	Local Grashof number	h	Convergence-control parameter.
f_w	Suction or injection parameter	A_1	Intrinsic viscosity
g	Gravitational acceleration vector	A_2	Huggins' coefficient
d_f	Fractal dimensions	A_k	Kapitza radius
d_i	Chemical dimensions	r_{in}	Radius of inner cylinder
Re_x	Local Reynolds number	r_{out}	Radius of the enclosure
N_{int}	Number of cluster's particles	Ha	Hartmann number

N_c Number of backbone's particles

R_p Particle radius

$\mathcal{L}, i = 1, 2$ Linear operators

R_g Gyration radius

$N, i = 1, \dots, 6$ Non-linear operators

$C, i = 1, \dots, 39$ Constants

Greek symbols

ρ Density

ζ Rotation angle

μ Viscosity

ν Kinematic viscosity

β_0 Magnetic field strength

θ Dimensionless temperature

Ω Semi-angle of cone

k^* Mean absorption coefficient

λ Mixed convection parameter

γ Inclined angle

λ_1 Magnetic field angle

ψ Stream function

ϕ Volume fraction

σ_0 Electric conductivity

β Thermal expansion coefficient

k Thermal conductivity

Λ Porosity parameter

σ^* Stefan-Boltzmann

ε^* Viscoelastic parameter

Ψ Sphericity

σ Surface tension

ε Eccentricity

Subscripts

nf Nanofluid

s Solid particle

int Cluster

c Backbone particles

c Cold

h Hot

f Base fluid

$layer$ Nanolayer

a Aggregation

nc Dead ends particles

ave Average

loc Local